UCLA
UCLA Electronic Theses and Dissertations

Title

Optogenetic-fMRI Investigations of Arousal Networks and Analysis Strategies

Permalink

https://escholarship.org/uc/item/4cr5b5bj

Author

Liu, Jia

Publication Date

2016

Peer reviewed|Thesis/dissertation

UNIVERSITY OF CALIFORNIA

Los Angeles

Optogenetic-fMRI Investigations of Arousal Networks and Analysis Strategies

A dissertation submitted in partial satisfaction

of the requirements for the degree

Doctor of Philosophy in Neuroscience

by

Jia Liu

2016

ABSTRACT OF THE DISSERTATION

Optogenetic-fMRI Investigations of Arousal Networks and Analysis Strategies

by

Jia Liu

Doctor of Philosophy in Neuroscience

University of California, Los Angeles, 2016

Professor Thomas Stephen Otis, Chair

Optogenetic functional magnetic resonance imaging (ofMRI) is a novel technique that enables whole-brain visualization of the downstream effects of manipulating a specific neural population. This thesis presents two studies that demonstrate the advantages of ofMRI in brain circuit analysis and offer practical recommendations for ofMRI data analysis. We first describe a study where the technical advantage of ofMRI is utilized in the investigation of arousal networks. The role of central thalamus in forebrain arousal and the frequency-selective modulation of whole-brain networks are uncovered. We then address the challenges of accurate detection and characterization of hemodynamic responses with highly variable temporal dynamics in the ofMRI datasets. In order to find the optimal analysis method, a comprehensive evaluation of the commonly used approaches is presented.

The dissertation of Jia Liu is approved.

Jin Hyung Lee

Mark S Cohen

Michael Levine

Abeer Alwan

Thomas Stephen Otis, Committee Chair

University of California, Los Angeles

2016

TABLE OF CONTENTS

LIST OF FIGURES

LIST OF TABLES

ACKNOWLEDGMENTS

Getting the PhD has been a long yet rewarding journey in my life. I am blessed for meeting all the amazing people who made this fulfilling journey possible and enjoyable.

First, I would like to thank my advisor, Professor Jin Hyung Lee, for agreeing to take me on as a student when I knew nothing about optogenetics and fMRI. Over the past few years, Jin has taught me significantly on how to approach scientific problems and conduct research in a meticulous manner. I would also like to thank my thesis committee members, Professor Tom Otis, Professor Michael Levine, Professor Mark Cohen, and Professor Abeer Alwan, whose feedback and suggestions have offered great help in shaping this dissertation.

I am grateful to the neuroscience interdepartmental program at UCLA for their generous and kind support. In particular, I would like to thank the previous chair, Professor Michael Levine, the current chair, Professor Felix Schweizer, and the staff members, Jenny Lee, Melissa Sherlock, and Suzie Vader. They have been extremely nice, patient, supportive to me.

I thank all the members in the Lee Lab for making my graduate school experience pleasant and enjoyable. Zhongnan Fang has showed me the meaning of persistence and has offered many help on the fMRI data processing. Hyun Joo Lee has showed me the meaning of hardworking and I find myself constantly amazed by the high quality data collected by him. Andrew Weitz has showed me the meaning of dedication and has contributed significantly in the data analysis in Chapter 2. Peter Lin has offered a lot of help within and outside of the lab, and is a good friend to me. Mankin Choy is extremely knowledgable and has also brought a lot of fun into this lab. Ben Duffy and David Bernal-Casas has been extremely helpful in the study shown in Chapter 3 and I am very grateful to their contributions. Other members in the lab, including Wesley Smith, Nguyen Le, Divya Raman, Mazen Asaad, Miggy Chuapoco, Cagan Alkan, and Jason Rudberg have also helped making the lab an enjoyable workplace.

Finally, I thank all my friends for sharing many beautiful moments with me over the past few years. I thank my parents, Ling Chen and Zhaozhi Liu, for their unconditional love and encour-

agement throughout my entire life. I would have never come this far without their continuous support. In the end, I thank Vasiliy - it is difficult to imagine these several years without his support.

2005-2009   B.S. Life Sciences

University of Science and Technology of China

2013-2015   Teaching Associate

University of California, Los Angeles

2014-2015   Technology Transfer Intern

UCLA Office of Intellectual Property

2015-2016   Visiting Graduate Student Researcher

Stanford University

PUBLICATIONS

1. **Liu J**[†], Duffy BA[†], Bernal-Casas D, Fang Z, and Lee JH. *Comparison of fMRI analysis methods for heterogeneous BOLD responses in block design studies.* NeuroImage (2016); Under Review.

2. **Liu J**[†], Lee HJ[†], Weitz AJ[†], Fang Z[†], Lin P, Fisher R, Pinskiy V, Tolpygo A, Mitra P, Schiff N, and Lee JH. *Frequency-selective control of cortical and subcortical networks by central thalamus*, eLife (2015); 4:e09215.

3. Byers B[†], Lee HJ[†], **Liu J**[†], Weitz AJ[†], Lin P, Zhang P, Shcheglovitov A, Dolmetsch R, Reijo Pera R, and Lee JH. *Direct in vivo assessment of human stem cell graft-host neural circuits*, NeuroImage (2015); 114(1), 328-337.

4. Lin P, Fang Z, **Liu J**, and Lee JH. *Optogenetic Functional MRI.* Journal of Visualized Experiments (2015); In Press.

5. Weitz AJ[†], Fang Z[†], Lee HJ[†], Fisher R[†], Smith W[†], Choy M, **Liu J**, Lin P, Rosenberg M, and Lee JH. *Optogenetic fMRI reveals distinct, frequency-dependent networks recruited by dorsal and intermediate hippocampus stimulations.* NeuroImage (2015); 107, 229-241.

6. **Liu J**, Lee HJ, Weitz AJ, Fang Z, Lin P, Fisher R, Pinskiy V, Tolpygo A, Mitra P, Schiff N, and Lee JH. *Dynamic control of forebrain by central thalamus.* Society for Neuroscience Annual Conference (2015).

7. **Liu J**, Fang Z, Bernal-Casas D, and Lee JH. *Comparison of fMRI analysis methods for accurate detection of heterogeneous hemodynamic responses.* Society for Neuroscience Annual Conference (2015).

8. Byers B, Lee HJ, **Liu J**, Weitz AJ, Lin P, Zhang P, Shcheglovitov A, Dolmetsch R, Reijo Pera R, and Lee JH. *Whole-brain, functional interrogation of graft-host interactions in an intact animal.* Society for Neuroscience Annual Conference (2015).

9. **Liu J**, Lee HJ, Weitz AJ, Fang Z, Lin P, Fisher R, Pinskiy V, Mitra P, Schiff N, and Lee JH. *Whole brain dissection of central thalamic circuit function with optogenetic fMRI.* Society for Neuroscience Annual Conference (2014).

10. Weitz AJ, Fang Z, Lee HJ, Fisher R, Smith W, Choy M, **Liu J**, Lin P, Rosenberg M, and Lee JH. *Optogenetic fMRI reveals distinct, frequency-dependent networks recruited by dorsal and intermediate hippocampus stimulations.* Society for Neuroscience Annual Conference (2014).

11. Weitz AJ, Fang Z, Lee HJ, Fisher R, Smith W, **Liu J**, Rosenberg M, Parvizi J, and Lee JH. *On-demand generation of seizures with defined network propagation pathways.* Society for Neuroscience Annual Conference (2013).

[†] equal contribution

CHAPTER 1

Introduction

Brain is the most complex organ in the human body. The 100 billion neurons and 100 trillion nerve connections make deciphering this biological conundrum extremely challenging. To study the function of the brain, conventional means usually include the use of electrical and pharmacological approaches to manipulate neural activity and the recording of subsequent changes in the brain activity. However, as both electrical current and biochemical reagents lack the ability to distinguish the targeted neural populations from the non-targeted ones, it is difficult to disentangle the functional properties of these neural circuits without affecting the surrounding cells. In 2005, optogenetics was introduced as a technique that can alter the activity of specific types of neurons with high spatial and temporal precision [BZB05]. This has since opened new landscapes for the study of brain mechanism.

1.1 Optogenetics

Optogenetics is a technique that enables precise control of neural activities using light. When external light is applied, only genetically modified neurons respond and exhibit changes in their electrochemical activities. Specifically, using molecular biology and genetic engineering approaches, target neurons can be modified to selectively express light-sensitive proteins, typically ion channels. In these cases, light with certain wavelength can induce a conformational change in the light-sensitive ion channels, causing the pore of the channel to open and the ions to flow across cell membrane. This subsequently leads to depolarization or hyperpolarization of the neuron, depending on the property of the specific light-sensitive ion channels employed.
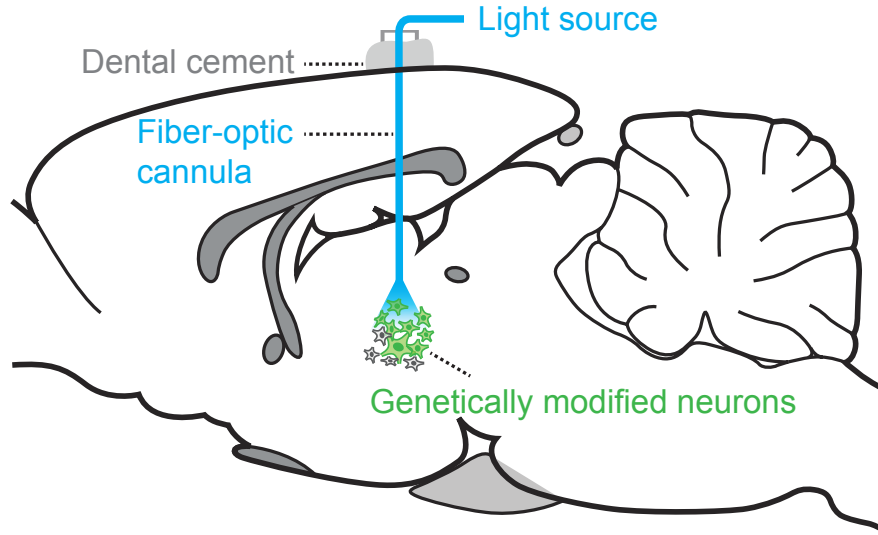
Figure 1.1: ***Schematic of a typical optogenetics experimental design.*** *Genetically modified neurons in green and optic fiber in blue are illustrated on a sagittal brain slice.*

1.1.1 Light-sensitive proteins

In 2005, Boyden et al. demonstrated the usage of exogenous light-sensitive ion channels in controlling the activity of mammalian neurons [BZB05]. Since then, numerous variants of light-sensitive proteins have been developed, offering a wide range of choices among different light absorption spectrums, ion selectivities, photocurrent amplitudes, and biochemical kinetics [YFD11].

If excitatory modulation is desired, light-sensitive cation channels can be selected. The most widely-used type is Channelrhodopsin-2 (ChR2), a nonspecific cation channel controlled by blue light [NBL05, GTZ07]. Compared to the wild type ChR2, a point mutation of H134R increases the amplitude of inward photocurrent by two folds [NBL05]. However, this mutation leads to a relatively slow kinetics, rending ChR2(H134R) unable to evoke stable spike trains beyond 40 Hz. In cases where higher temporal precision is required, ChR2 variants with a faster kinetics may be used, such as ChR2(E123A), ChR2(E123T), and ChR2(E123T/T159C) [GYB10, BSM11]. If blue light is already used to trigger other elements in an experiment, such as GCaMP in the calcium imaging [GHR09], light-sensitive ion channels that respond to other spectrums of light may be more appropriate, such as C1V1, which is activated by red light [YFP11]. In addition,
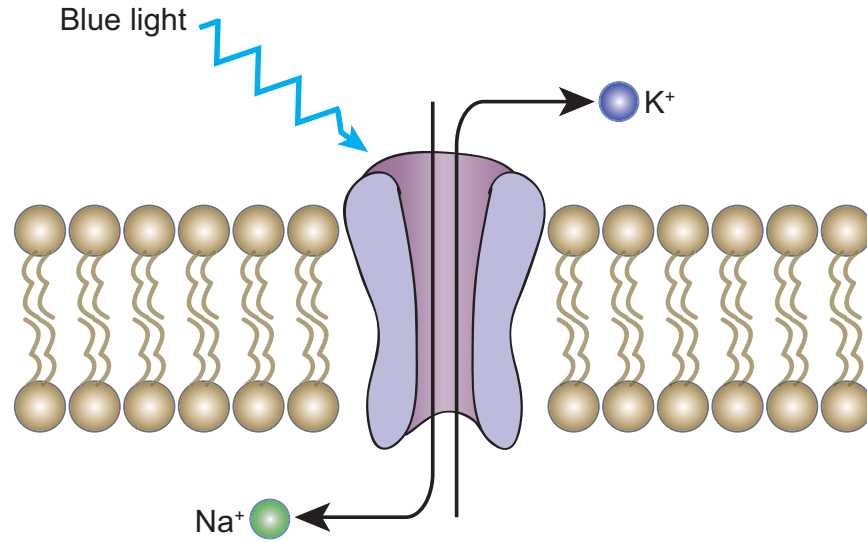
Figure 1.2: ***Channelrhodopsin-2 is a widely-used light-sensitive ion channel in optogenetic studies.*** *It is a nonspecific cation channel that responds to blue light.*

if prolonged excitation is required, using a switchable light-sensitive ion channels may be more advantageous than delivering the light stimulation over the entire duration. In this case, the effects of heat and light on neural functions can be reduced. An example of switchable light-sensitive ion channels is stabilized step function opsins (SSFOs), a ChR2 variant that can be opened by a blue light pulse and closed by a yellow light pulse [BYG09, BGK09, YFP11].

Conversely, if inhibitory modulation is desired, light-sensitive anion pumps may be used instead. Two popular types include light-sensitive proton pumps and chloride pumps. An example of light-sensitive proton pumps is Arch, which is triggered by yellow light. Examples of light-sensitive chloride pumps are NpHR (halorhodopsin, triggered by yellow light) [GZR10], C1C2 (triggered by blue light), and SwiChR (Step-Waveform Inhibitory ChannelRhodopsin, opened by a blue light pulse and deactivated by a red light pulse) [BLR14].

1.1.2 *In vivo* expression of exogenous light-sensitive proteins

Local injection of viral construct via stereotaxic surgery is a standard approach to introduce exogenous light-sensitive proteins into target neurons. The injected viral construct is usually an engineered viral vector (such as adeno-associated virus, or AAV) that carries the gene of interest.

Two approaches are commonly used to ensure selective expression in target neurons. One approach is to include a cell type-specific promoter sequence in the viral construct. In this case, only neurons with matching cell types are able to express exogenous light-sensitive proteins. Examples of commonly used cell type-specific promoters include synapsin (neuron specific) and CaMKIIα (excitatory glutamatergic neurons). The other approach is to include a double-floxed inverse open-reading frame (DIO) in the viral construct. In this case, the gene of the light-sensitive proteins starts in an inverted, inactive orientation, and is not expressed unless with the presence of CRE recombinase. Virus with DIO construct is usually injected into a transgenic animal with tissue-specific CRE recombinase expression. In the cells that co-express CRE recombinase, the gene is inverted to the correct orientation and expressed. As the cell type specificity is enabled via the expression location of the CRE recombinase, the promoter in the viral construct does not need to be tissue-specific. Instead, the promoter can be selected to drive a robust expression of light-sensitive proteins.

1.1.3 *In vivo* light delivery

The standard method to deliver light into the brain region of interest is to implant a fiber-optic cannula via stereotaxic surgery. During the surgery, the cannula is secured in the skull using dental cement. In the subsequent experiments, the implanted fiber-optic cannula can be coupled with a fiber-optic cable through a mating sleeve. The fiber-optic cable is then connected to an external light source. The light source is usually a laser or light-emitting diodes (LED) based system. The parameters of the optical stimulation, such as the frequency and width of the light pulse, can be controlled using a signal generator.

In addition to fiber-optic cannula, several novel light delivery methods have been proposed recently. A good example is LED-based wireless devices [KMJ13, RGM15]. In these devices, the LEDs are usually battery powered and can deliver light into regions of interest without connecting to external light and power source. These devices may be particularly useful in studying the behavior of freely moving animals.
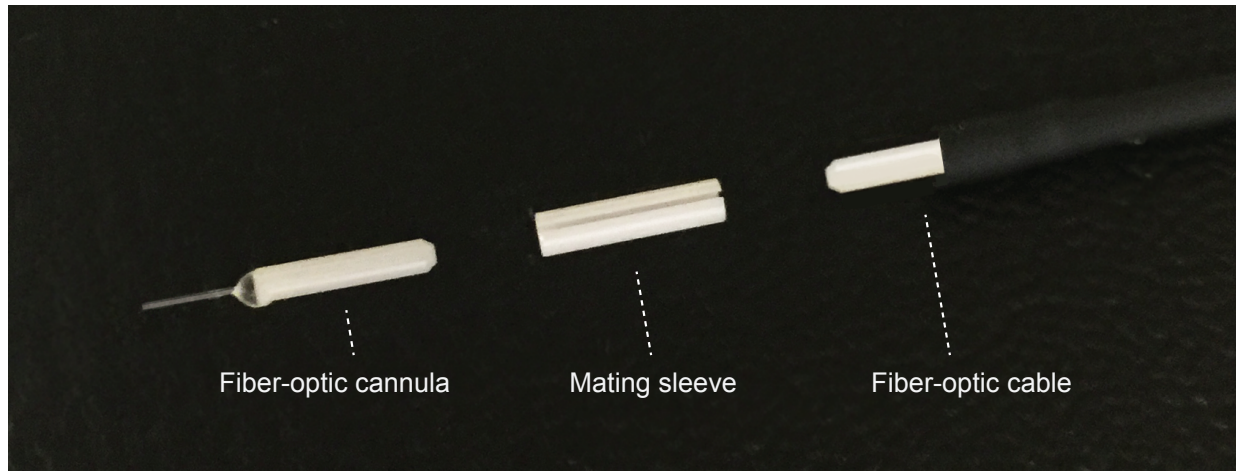
Figure 1.3: **Fiber-optic cannula is commonly used to deliver light *in vivo* in optogenetic studies.**

1.2 Overview of techniques that measure brain activity

As discussed above, the activity of specific neural population can be selectively manipulated with optogenetic approaches. To measure the resulting changes in the neural activity, multiple techniques can be used. Four of them are employed in this thesis, each with a unique combination of spatial and temporal resolutions.

1.2.1 Electrophysiological techniques

Electrophysiological techniques provide high temporal resolutions, usually in the order of milliseconds, but usually without whole-brain coverage. They offer direct measurement of neural activity by recording electrical current and changes in the membrane potential. When neurons are at rest, the net ion flow across membrane is zero. The corresponding difference in membrane potentials is the resting potential. When neurons receive electrical or biochemical inputs, the ion channel on the cell membrane will open or close, resulting in an inward or outward ion flow across membrane, and causing membrane potential to deviate from the resting potential. The change in the membrane potential, such as graded potentials or action potentials, is recorded using electrophysiology techniques.

Electrophysiological techniques, including electroencephalography (EEG), local field poten-

tial (LFP), and single-unit recording, are employed in this thesis. Both EEG and LFP capture the summation of synchronous activities from multiple neurons. EEG recordings usually reflect a large number (up to millions) of neurons, while LFP method records a smaller number of neurons that are close to the recording electrodes. Conversely, single-unit recording is at single-neuron resolution and commonly performed in an extracellular fashion *in vivo*.

1.2.2 Functional magnetic resonance imaging

Functional magnetic resonance imaging (fMRI) offers whole-brain coverage, high spatial resolution, but low temporal resolution, typically on the order of seconds. This technique indirectly measures neural activity through associated changes in the blood flow. The commonly used blood-oxygen-level dependent (BOLD) contrast [OLK90] is based on the following mechanism. When neurons are firing, the increase in the neural activity boosts the oxygen consumption. This accelerates the conversion of oxygen-carrying oxyhemoglobin (Hb) to non-oxygen-carrying deoxyhemoglobin (dHb), and reduces Hb/dHb ratio in the blood. The decrease in the Hb/dHb ratio is then over-compensated by an increase in the blood flow in the vicinity of the firing neurons, which dilutes the concentration of dHb and leads to a net increase in the Hb/dHb ratio. The change in the Hb/dHb ratio is reflected by the change in the T2* signal. The mechanism is that, dHb is paramagnetic, therefore its presence in the blood vessel can cause susceptibility differences between the blood vessel and the surrounding tissue, resulting in dephasing of the magnetic resonance proton signal [TWM82] and a reduction in the T2* value. Conversely, Hb is diamagnetic and does not produce the same dephasing as dHb. Therefore, it does not lead to a reduction in the T2* value. Together, an increase in the neural activity leads to an elevated Hb/dHb ratio and an increase in the T2* value and BOLD signal intensities. A decrease in the neural activity reduces the Hb/dHb ratio and decreases BOLD signal intensities. Upon measuring the BOLD signals over time, the whole-brain neural activity change can be recorded.

Compared to electrophysiological techniques, fMRI datasets usually require more complicated analysis. The most commonly used analysis method is based on the general linear model (GLM) framework [FHW94, SJW04]. GLM assumes the linear time-invariant system, which

6
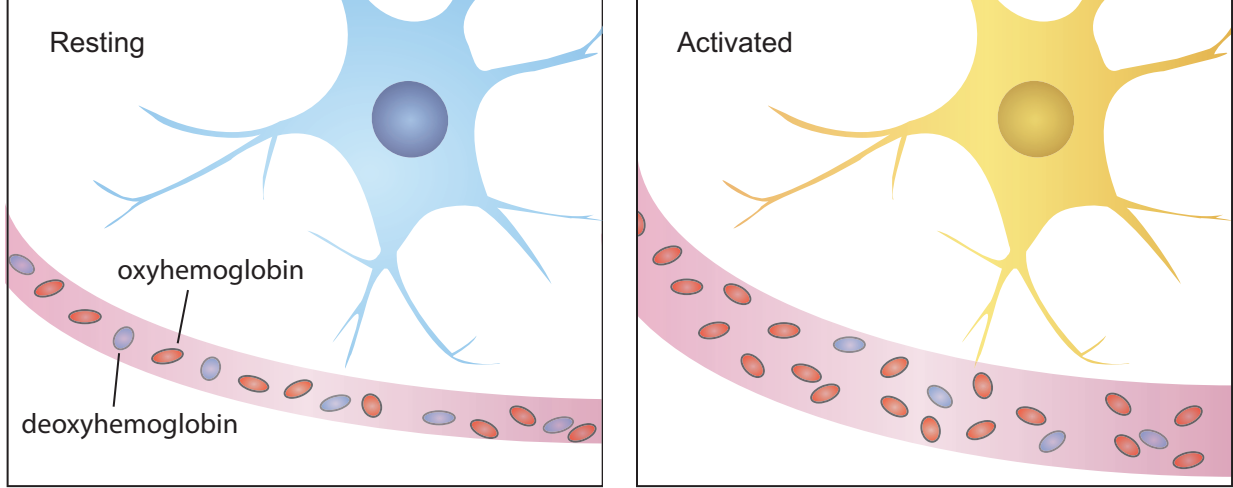
Figure 1.4: ***Mechanism of hemodynamic response.*** *Upon activation, the increase in the oxygen consumption is over-compensated by an increase in the blood flow in the vicinity of the active neurons, resulting in a net increase in the oxyhemoglobin/deoxyhemoglobin ratio.*

enables prediction of BOLD response to a long stimulation using known response to a short stimulus [UUB15]. As shown in Eq. (1.1), observed fMRI time course (Y) is represented by the addition of fitted time series ($X\beta$) and residuals (ε).

$$Y = X\beta + \varepsilon \tag{1.1}$$

In Eq. (1.1), X is a set of regressors, which is also referred to as the design matrix. β is the regression coefficient.

To examine whether there is a significant linear relationship between the fitted time course and the observed data, t and F statistical tests are commonly used.

$$t = \frac{\hat{\beta}_i}{se(\hat{\beta}_i)} \tag{1.2}$$

Eq. (1.2) is the equation for t test. $\hat{\beta}_i$ is the least square estimate of β_i, and $se(\hat{\beta}_i)$ is its standard error.

$$F = \frac{MS_R}{MS_E} = \frac{SS_R/df_R}{SS_E/df_E} \tag{1.3}$$

Eq. (1.3) is the equation for F test. MS_R is the mean square of regression, which equals the ratio of SS_R, the regression sum of squares, and df_R, its degrees of freedom. MS_E is the mean square of error, which equals the ratio of SS_E, the error sum of squares, and df_E, its degrees of freedom.

Based on the resulting t and F statistics, and the corresponding t- and F-distributions, p value can be obtained to determine whether there exists statistical significance at the voxel of interest in the fMRI datasets.

1.3 Optogenetic-fMRI

Optogenetic-fMRI (ofMRI) is a technique that combines optogenetic control with fMRI readout. It enables whole-brain monitoring of neural activity that arises from the manipulation of selected neural circuit elements [LDG10].

Lee et al. presented the first ofMRI study in 2010 [LDG10]. There, optogenetic excitation of the ChR2-expressing pyramidal neurons in the rat motor cortex drives positive BOLD responses locally in the motor cortex and remotely in the thalamus. Direct stimulation of the ChR2-expressing cortico-thalamic projection fibers in the thalamus yields similar activation patterns. The results are supported by immunohistochemistry and electrophysiology experiments. These findings demonstrate a strong potential for ofMRI in the global mapping of the causal connectivity of specific neural populations.

1.4 Thesis outline

This thesis describes two studies. The first study uses the technical advantage of ofMRI to uncover the role of central thalamus in forebrain arousal and its frequency-selective modulation of whole-brain networks. The second study addresses the challenge of analyzing ofMRI data with heterogeneous BOLD response shapes and provides a systematic assessment of available approaches.
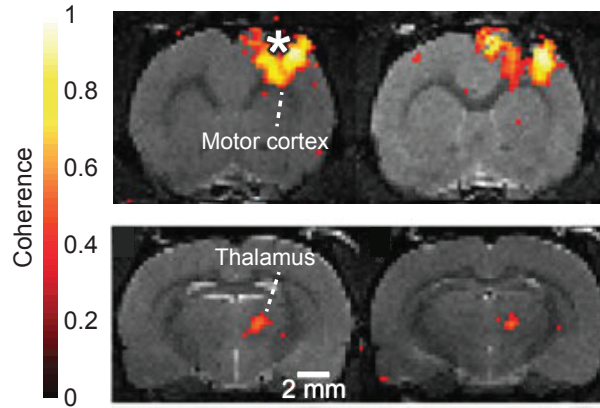
Figure 1.5: ***ofMRI results show that optogenetic excitation of rat motor cortex drives local and remote BOLD responses.*** *Upon optical stimulation of transduced neurons in the motor cortex, positive BOLD responses are observed locally in the motor cortex and remotely in the thalamus. Asterisk denotes the site of optical stimulation. This figure is adapted from [LDG10].*

Chapter 2: Optogenetic-fMRI reveals frequency-selective control of arousal networks by central thalamus

This chapter is adapted from [LLW15]. In this chapter, we investigate the arousal networks modulated by the central thalamus by combining ofMRI with electrophysiology and video-EEG readout. Central thalamus is a key component in the forebrain arousal system and serves as a potential target for therapeutic deep brain stimulation (DBS) in subjects with traumatic brain injury. However, the mechanisms that link the neural activity in the central thalamus to the changes in brain state remains enigmatic, which significantly limits the clinical efficacy of central thalamus DBS. In this study, we find that, high frequency stimulations of central thalamus, such as 40 and 100 Hz, cause widespread activation of forebrain, including frontal cortex, sensorimotor cortex, and striatum, and transition the brain to a state of arousal in asleep rats. In contrast, low frequency stimulation, such as 10 Hz, evokes significantly less activation of forebrain, inhibition of sensory cortex, and behavioral arrest. To investigate possible mechanisms underlying the frequency-dependent cortical inhibition, we perform recordings in zona incerta, where 10, but not 40, Hz stimulation evokes spindle-like oscillations. Importantly, suppressing incertal activity during 10 Hz central thalamus stimulation reduces the evoked cortical inhibition. Together, our findings identify key brain-wide dynamics underlying central thalamus arousal regulation.

Chapter 3: Comparison of fMRI analysis methods for heterogeneous BOLD responses in ofMRI studies

This chapter is adapted from [LDB16]. In this chapter, we address the challenge in the analysis of ofMRI data caused by heterogeneous BOLD response shapes. Specifically, a large number of fMRI studies have shown that the temporal dynamics of evoked BOLD responses can be highly heterogeneous. Failing to model heterogeneous responses in statistical analysis can lead to significant errors in signal detection and characterization and alter the neurobiological interpretation. However, to date it is not clear that, out of a large number of options, which methods are robust against variability in the temporal dynamics of BOLD responses in ofMRI studies. Here, we use rodent ofMRI data in Chapter 2 with heterogeneous BOLD responses and simulations guided by experimental data as a means to investigate different analysis methods' performance against heterogeneous BOLD responses. Evaluations are carried out within the GLM framework and consist of standard basis sets as well as independent component analysis (ICA). Analyses show that, in the presence of heterogeneous BOLD responses, conventionally used GLM with a canonical basis set leads to considerable errors in the detection and characterization of BOLD responses. Our results suggest that the 3rd and 4th order gamma basis sets, the 7th to 9th order finite impulse response (FIR) basis sets, the 5th to 9th order B-spline basis sets, and the 2nd to 5th order Fourier basis sets are optimal for good balance between detection and characterization, while the 1st order Fourier basis set (coherence analysis) used in Chapter 2 show good detection capability. ICA has mostly good detection and characterization capabilities, but detects a large volume of spurious activation with the control ofMRI data.

CHAPTER 2

Optogenetic-fMRI reveals frequency-selective control of arousal networks by central thalamus

This section is adapted from:

Liu J[†], Lee HJ[†], Weitz AJ[†], Fang Z[†], Lin P, Fisher R, Pinskiy V, Tolpygo A, Mitra P, Schiff N, Lee JH. *Frequency-selective control of cortical and subcortical networks by central thalamus*, eLife (2015); 4:e09215.

2.1 Introduction

The thalamus plays an important role in coordinating global brain signals responsible for cognition and normal waking behavior [SG96, LRC98, MSS14]. The central thalamus and intralaminar nuclei, in particular, have been postulated to play a critical and unique function in regulating arousal, attention, and goal-directed behavior [Sch08, MOH11]. This idea dates back to the first demonstrations that direct and indirect electrical stimulations of central thalamus control cortical EEG dynamics and elicit behavioral transitions between drowsiness/relaxation and wakefulness/attention [MM49, HJ49, Fur58]. Since the initial identification of central thalamus's causal effect on brain state and behavior, significant support for its role in arousal regulation has come from anatomical and histological studies. Steriade and Glenn [SG82] identified a monosynaptic pathway from the mesencephalic reticular formation to the central lateral (CL) and paracentral (PC) nuclei of central thalamus that projects to cerebral cortex and striatum. In addition to this input, the central thalamus receives projections from other arousal systems, including norepinephrinergic innervation from locus coeruleus [VHF08] and cholinergic innervation from the upper brainstem and basal forebrain [HGM92]. In combination with these inputs, the diffuse projections of central thalamus allow it to influence the overall excitability of cortex during states of attention. For example, virtually all relay cells of the CL nucleus project to both striatum and cerebral cortex [DBP96].

Studies on the physiological properties of central thalamus also show that it is tightly coupled to arousal regulation. First, variations in the level of activity within the intralaminar nuclei are linked to changes in behavioral alertness [KLG96, SSS06, MH08, SSH13, GDP15], including transitions during the normal sleep-wake cycle and acute cognitive enhancements such as improved working-memory and sustained attention. Similarly, lesions of the central thalamus can produce enduring cognitive impairments, including reduced attentional processing and memory [GS83, MBP98, VWJ99, NB05], hypersomnolence [BMG96], or even coma [CLB81, Plu91]. Indeed, neuronal loss across central thalamus has been associated with severely disabled and vegetative patients following severe traumatic brain injury [MMS06]. In addition, electrical stimulation of the central thalamus at low frequencies is associated with absence seizures and behavioral

arrest in animal models [HJ49] and human subjects [VVV97]. Human imaging studies have also found that anesthesia-induced loss of consciousness is associated with disrupted thalamocortical functional connectivity in regions consistent with the intralaminar nuclei [ALC15].

According to the mesocircuit hypothesis of forebrain dysfunction, the central thalamus, which has a strong activating role in driving cortical and striatal neurons [Sch10], is under tonic inhibition by GABAergic pallidal neurons [GHM05]. This GABAergic population is itself inhibited by the striatal neurons driven by central thalamus, creating a positive feedback loop. Thus, when the thalamostriatal and thalamocortical projections from central thalamus are partially lost due to brain injury, it causes disinhibition of the pallidum and increased inhibition of the remaining central thalamus neurons, which further reduces cortical activation. While this down-regulation is predicted to have broad modulatory impact on global dynamics, central thalamus DBS has been explored as a potential means of reversing its effects and facilitating arousal regulation in the minimally conscious state [SSS06, SGK07, MH08, SSH09, MOH11, Sch12, FBB14, GMS15]. Despite success in a single-subject clinical study [SGK07], identification of circuit-level mechanisms that link therapeutic efficacy of central thalamus DBS to specific stimulation parameters remains challenging and at present limits the clinical efficacy of DBS in subjects with traumatic brain injury. Thus, while significant progress has been made in understanding the connections of central thalamus and its behavioral correlates [WWG02, Sch08], relatively little is known about the dynamic function of these circuits, and no clear mechanism exists to explain how - or indeed, if - a single population in central thalamus can act as a switch on the global brain state.

To overcome such obstacles and dissect the dynamic influence of central thalamus on global brain networks, we combined ofMRI, EEG, and single-unit recordings, to uncover the downstream effects of distinct firing patterns by central thalamus relay cells at the whole-brain level. Prior work beginning with Morison and Dempsey [MD41], who envisioned "dissecting... the electrical activity of the cortex on the basis of its relations with the thalamus," has shown that high- and low-frequency electrical stimulation of thalamic nuclei can produce distinct cortical activation patterns. For example, early studies of the intralaminar nuclei per se showed that low-frequency stimulation evokes slow-wave activity and spindle bursts in cortical EEG, which

13

are associated with primary generalized absence seizures, loss of consciousness, and drowsiness [HJ49, Jas49, SP01]. Conversely, high-frequency electrical stimulation has been shown to desynchronize the cortical EEG signal [MM49], which is associated with behavioral arousal. While these studies set early hypotheses on the mechanisms of arousal regulation, the non-selective nature of electrical stimulation has prevented the observed responses from being attributed specifically to relay cells, and not synaptic afferents or fibers of passage mixing together in a bulk activation effect. More importantly, although a picture of whole brain activity can be vaguely inferred from electrophysiology recordings, these techniques cannot provide a direct visualization of activity across individual brain regions over the entire brain. Because ofMRI can provide spatial and temporal information on the whole-brain scale during perturbations of specific neural circuitry, we applied this technique to study the causal role of central thalamus relay neurons in activating forebrain networks.

In addition, following on novel results described below, we were led to examine the interplay between central thalamus and zona incerta (ZI), a subcortical region implicated in the modulation of absence seizures in rats [SLC13]. The zona incerta, a mostly GABAergic region, has been shown to limit the transmission of ascending sensory information via feedforward inhibition of higher-order thalamic nuclei [BFA02, TK04, LUD05, TBM06]. Such activity can induce a state of reduced sensory processing, similar to the behavioral quiescence induced by low-frequency central thalamus stimulation. These studies suggest a powerful control exerted by zona incerta over brain state and higher-level processing, much like central thalamus. However, the possible involvement of zona incerta in central thalamus arousal circuits remains unexplored. Here, we investigated the electrophysiology responses of this region during targeted stimulation of central thalamus at frequencies that either facilitate or suppress attention and arousal. To determine whether zona incerta plays an active role in these circuits, we also used optogenetics to specifically inhibit neurons in this region during central thalamus stimulation. This experimental paradigm was used to infer zona incerta's functional contribution to the central thalamus-driven brain circuit dynamics measured with fMRI and electrophysiology.

2.2 Materials and methods

2.2.1 Animals

Female Sprague-Dawley rats (>11 weeks old, 250-350g) were used as subjects for all thalamic injections. Animals were individually housed under a 12 hour light-dark cycle and provided with food and water ad libitum. Animal husbandry and experimental manipulation were in strict accordance with National Institute of Health, UCLA Institutional Animal Care and Use Committee (IACUC), and Stanford University IACUC guidelines.

2.2.2 Viral injections and fiber placement

pAAV5-CaMKIIα-hChR2(H134R)-EYFP-WPRE plasmid was obtained from the Deisseroth lab at Stanford University. Concentrated virus was produced at the vector core of the University of North Carolina at Chapel Hill. Rats were anesthetized with isoflurane (induction 5%, maintenance 2-3%; Sigma-Aldrich, St. Louis, Missouri, USA) and secured in a stereotactic frame. Standard procedures for sterile surgery were followed. Buprenorphine was administered to minimize pain. Artificial tears were applied to the eyes. The head was shaved, and 70% ethanol and betadine were applied to the bare scalp following a midline incision. A small craniotomy was performed with a dental drill above the targeted coordinate. Two microliters of virus were injected through a 34 gauge needle (World Precision Instruments Inc., Sarasota, FL) at 150 nl/min with a micro-syringe pump controller at the desired coordinates in central thalamus or other subcortical targets for control experiments: I) CL and PC nuclei of central thalamus (-3.2 mm AP, +1.5 mm ML, -5.6 mm DV; n = 47 animals for imaging); II) ventral posteromedial nucleus (-2.5 mm AP, +2.6 mm ML, -6.0 mm DV); III) anterior thalamic nuclei (-3.1 mm AP, +1.8 mm ML, -5.3 mm DV); IV) posterior thalamic nuclei (-4.6 mm AP, +1.8 mm ML, -5.0 mm DV); V) intermediate hippocampus (-5.8 mm AP, +5.2 mm ML, -3.4 mm DV, n = 8 animals). All injections were made in the right hemisphere. The syringe needle was left in place for an additional 10 minutes before being slowly withdrawn. Custom-designed guide cannulas (Plastics One) or fiber-optic cannulas (Doric Lenses Inc.) were mounted on the skull and secured using metabond

15

(Parkell). Incisions were sutured, and animals were kept on a heating pad until recovery from anesthesia. Buprenorphine was injected subcutaneously twice daily for 48 hours post-operatively to minimize discomfort. The original cohort of 47 central thalamus animals was further refined to a group of 18 after screening for implant locations less than 0.85 mm away from the target coordinate (estimated with T2 MRI scans; Figure 2.2B). Two additional animals were excluded due to lack of thalamic activation, leaving 16 animals for analysis.

In a second cohort of rats, concentrated AAV5-hSyn-eNpHR3.0-mCherry virus produced at the University of North Carolina at Chapel Hill vector core was injected into the right zona incerta (-3.96 mm AP, +2.8 mm ML, +7.4 mm DV, n = 4 animals) after completion of the ChR2 injection into the central thalamus as described above. Both injections were performed during the same surgery. 0.5 microliters of eNpHR virus were injected through a 34 gauge needle at 100 nl/min. Following the injection, the syringe needle was left in place for approximately 10 minutes before being slowly withdrawn. Recovery details were the same as described above.

2.2.3   ofMRI data acquisition

fMRI scanning was performed using a 7T Bruker Biospec small animal MRI system at UCLA. Animals were initially anesthetized with 5% isoflurane and intubated before placement onto custom-made MRI-compatible cradles with ear and tooth securement. A 39 mm outer diameter, 25 mm inner diameter custom-designed transmit/receive single-loop surface coil was centered over the region of interest on the skull to maximize signal-to-noise ratio. An optical fiber of 62.5 μm core diameter was connected to a 473 nm laser source (Laserglow Technologies, Toronto, Canada) and coupled with the implanted fiber-optic cannula. A single ofMRI scan consisted of a block design with six 20 s pulse trains of light (10, 40, or 100 Hz in randomized order) delivered once per minute over 6 minutes. Five to six consecutive scans were collected during each session. For all experiments, the optical fiber output power was calibrated to 2.5 mW. A duty cycle of 30% was used across frequencies to maintain the total amount of light delivery, resulting in unique pulse widths of 30, 7.5, and 3 ms for 10, 40, and 100 Hz, respectively. In a series of control experiments using a second cohort of animals with validated probe locations (n = 3), the

duty cycle was varied while the pulse width was held constant at 3 ms (Figure 2.6).

During fMRI scanning, animals were placed into the iso-center of the magnet while artificially ventilated (45-60 strokes/min) under light anesthesia using a ventilator and calibrated vaporizer with a mixture of O_2 (35 %), N_2O (63.5 %), and isoflurane (1.3-1.5 %). To ensure stable BOLD signals, expiratory CO_2 was kept at 3-4 % and body temperature was maintained at 36.5-37.5 °C using heated airflow. T2-weighted high-resolution anatomical images were acquired with a fast spin echo sequence prior to fMRI scanning to check for brain damage and validate the optical fiber's location (137 μm resolution in-plane resolution with 35×35 mm^2 FOV, 0.5 mm slice thickness, 32 coronal slices). Gradient recalled echo (GRE) BOLD methods were used to acquire fMRI images during photostimulation. The fMRI image acquisition was designed to have 35×35 mm^2 in-plane field of view (FOV) and $0.5 \times 0.5 \times 0.5$ mm^3 spatial resolution with a sliding window reconstruction to update the image every repetition time (TR) [FL13]. The two-dimensional, multi-slice gradient-echo sequence used a four-interleave spiral readout [GL95, KAS03], 30 degree flip angle, 750 ms TR, and 12 ms echo time, resulting in 23 coronal slices (128×128 matrix size). The spiral k-space samples were reconstructed through a 2-dimensional gridding reconstruction method [JMN91]. Finally, real-time motion correction was performed using a previously described GPU-based system [FL13]. Scans with significant motion, identified by careful visual inspection for spiral artifacts and activations at the boundary of the brain, which indicates large motion, were excluded from analysis. This condition for exclusion was established prior to data collection.

2.2.4   fMRI data analysis

All fMRI data processing was performed using the Matlab software environment (MathWorks, Inc., Natick, MA) and mrVista (Stanford Vision and Imaging Science and Technology Laboratory, Stanford, CA). Motion-corrected images belonging to consecutive scans of the same stimulation paradigm and scanning session were first averaged together. The average 4D images were then aligned to a common coordinate frame, using a six degree-of-freedom rigid body transformation. If multiple scanning sessions were performed on the same animal at the same frequency

(typically 1, at most 4), the resulting images from each session were first averaged together before any inter-subject analysis to achieve maximum SNR while weighting the images from all animal subjects equally.

Time series were calculated for each voxel in these individual-animal images as the percent modulation of the BOLD signal relative to a 30 s baseline period collected prior to stimulation. Boxcar detrending with a window size of 1 minute was also performed to correct for possible scanner drift. Next, a coherence value was calculated for each voxel's time series as the magnitude of its Fourier transform at the frequency of repeated stimulation blocks (i.e. 1/60 Hz) divided by the sum-of-squares of all frequency components [EGW97]. Voxels with a coherence value greater than 0.35 were considered to be significantly synchronized to stimulation. Assuming Gaussian noise and 470 degrees of freedom (computed using the SPM software environment), the Bonferroni-corrected P value for this threshold can be estimated to be less than 10^{-9} [BJW93]. Activation volume was defined as the number of significant voxels that exhibited a positive response within a predefined region of interest, multiplied by the volume per voxel. Positive responses were identified as having a phase in the interval $[0, \pi/2] \cup [3\pi/2, 2\pi]$. Phase represents the temporal shift of the response when it is modeled as a sinusoid, and was calculated as the argument of each voxel's Fourier transform at the frequency of repeated stimulation blocks (i.e. 1/60 Hz).

HRFs were calculated as the average 60 s response of a voxel's six-cycle, 6-minute time series. Time series and HRFs displayed for figures were generated by averaging the mean time series or mean HRF of voxels with a coherence value greater than 0.35 in the corresponding ROI across animals.

To generate average activation maps (Figure 2.4), the 4D fMRI images from experiments at the same stimulation location and frequency were normalized and averaged together across animals. The averaged images were then processed according to the above Fourier domain analyses. Coherence values were overlaid onto all voxels having a coherence above the 0.35 threshold. Warm and cool colormaps generated using Matlab's 'hot' and 'winter' functions were used for positive and negative responses, respectively, to illustrate the localization of negative BOLD to

the somatosensory cortex. These activation maps were overlaid onto corresponding T2-weighted anatomical images with a digital standard rat brain atlas [PW06]. The same atlas was used to segment ROIs. An identical analysis pipeline was used for activation maps in Figure 2.8 with a representative animal.

2.2.5 EEG electrode implantation

EEG electrodes were implanted upon completion of ofMRI experiments in a subset of animals. Surgical preparation and recovery details were the same as those used for virus injection. Stainless steel screws (0-80, 1.5 mm diameter, Plastics One) attached to 2 cm of insulated wire (30 gauge, R30Y0100, Wire Wrapping Wire, O.K. Industries) were used as EEG electrodes and secured on the skull using dental cement. The recording electrode was placed approximately 2 mm anterior of bregma and 2 mm to the right of midline. The reference electrode was located approximately 5 mm anterior of bregma and 3 mm to the left of midline [HSO03].

2.2.6 Video-EEG acquisition and analysis

Prior to video-EEG recording, animals were anesthetized under 5% isoflurane for approximately 5 min for optical fiber coupling and EEG wire connection. Animals were then transferred to a light- and sound-controlled experimental chamber where they were allowed to move freely. Behavioral experiments began after animals recovered from anesthesia and subsequently fell asleep for 15 min (as indicated by lack of motion and real-time EEG output readings). For each experiment, the animal was video-recorded during 5 min of sleep, followed by 20 s of optical stimulation (10, 40, or 100 Hz, 473 nm laser, 2.5 mW laser power, 30% duty cycle), and then an additional 5 min post-stimulation period. EEG data was acquired throughout the experiment at 1 kHz with an MP150 data acquisition unit and EEG100C amplifier (Biopac Systems Inc., Santa Barbara, CA), using EL254S Ag-AgCl electrodes and Gel102 conductive EEG paste. A digital camera was used to video-record the experiment. All behavioral experiments were performed during the animals' light cycle.

EEG recordings were classified using the Biopac Acqknowledge software by an experienced

electroencephalographer blind to treatment into a single best category: normal, low-voltage fast, spikes, spike-waves, or evolving electrographic seizure. Video clips paired to each EEG recording were classified into one of the following categories to further assess the animal's brain state: sleep (i.e. no change), awakening (animal is alert and exploring), absence seizure (animal is immobile and appears frozen for the duration of stimulation, but returns to a sleeping state once stimulation ends), or convulsive seizure. All observed behavioral responses could be classified into one of these categories. Band power in Figure 2.4 was quantified using Matlab's 'bandpower' function and normalized by the signal's total power from 0 Hz to one half the sampling rate (500 Hz).

2.2.7 *In vivo* electrophysiology

Upon completion of ofMRI and EEG behavioral experiments, *in vivo* electrophysiology experiments were performed in a subset of animals. Animals were anesthetized with 5% isoflurane for induction and maintained at 2-3% until any craniotomies were complete. Isoflurane was kept at 0.8-1.2% during the recording session, and artificial tears were applied to the eyes. Recordings in Figure 2.9 and Figure 2.11 were performed under ventilation conditions identical to fMRI experiments. After securing the animal within a stereotactic frame, small craniotomies were performed using a dental drill above the region of interest. For stimulation, the cannula implanted at central thalamus was connected to a 473 nm laser source (Laserglow Technologies) with an output power level of 2.5 mW via an optical fiber. The cannula implanted at zona incerta was connected to a 593 nm laser source (Laserglow Technologies) calibrated to 2.5-3.0 mW. An acute 16-channel microelectrode array was targeted to the recording site using stereotactic instruments (NeuroNexus Technologies; A1x16 standard model linear electrode array for local and cortical recordings; V1-16-Poly2 polytrode array for ZI recordings; 0.35±0.5 MOhm impedance). A stainless steel reference screw was placed above the cerebellum. Continuous field potential and single unit spiking events were recorded using the Plexon omniplex system with plexcontrol software (Plexon Inc., TX, USA). When only ChR2 was activated, recordings were performed for 20 seconds without stimulation, followed by repeated stimulation cycles (20 s on, 40 s off) at 10, 40, or 100 Hz with 30% duty cycle. When ChR2 and eNpHR were activated together, the

20

same stimulation paradigm was followed, except that a 30 s period of continuous 593 nm light delivery began 5 s before the onset of ChR2 excitation. When only eNpHR was activated (Figure 2.11D), a 20 or 30 s period of continuous 593 nm light delivery was used, with 40 or 30 s periods of no light delivery between repeated cycles, respectively. For single unit responses, the Plexon multichannel acquisition processor was used to amplify and band-pass filter the neuronal signals (150 Hz - 8 kHz). Signals were digitized at 40 kHz and processed to extract action potentials in real-time. To separate the field potential, we used a low-pass filter (200 Hz cutoff frequency, 4-pole Bessel filter) and downsampled signals to 1 kHz. Simultaneous EEG data was collected at 1 kHz during zona incerta recordings in Figure 2.9 using the MP150 data acquisition unit and EEG100C amplifier (Biopac).

2.2.8 Zona incerta electrophysiology analysis

For the analysis in Figure 2.9, field potential recordings were high pass filtered with a cutoff frequency of 2 Hz to eliminate respiratory artifacts. Spindle-like oscillations (SLOs) occurring during the stimulus were then quantified on a per trial basis using a post-hoc custom algorithm. Briefly, an SLO was identified when the recording's magnitude reached at least 6 standard deviations above its mean absolute value. If the recording did not exceed this value for the preceding 500 ms, and was above this value for at least 2% of samples over the next 500 ms, an SLO was counted. This method of quantification accurately captured the large-amplitude oscillations that could be visually discerned (see Figure 2.9D).

2.2.9 Fluorescence imaging and immunohistochemistry

Upon completion of *in vivo* ofMRI, behavioral, and electrophysiology experiments, rats were deeply anesthetized with isoflurane in a knockdown box and transcardially perfused with 0.1M PBS and ice-cold 4% paraformaldehyde (PFA) in PBS. Brains were extracted and fixed in 4% PFA overnight at 4°C. The brains were equilibrated in 10%, 20%, and then 30% sucrose in PBS at 4°C. Coronal sections (50 μm) were prepared on a freezing microtome (HM 430 Sliding Microtome, Thermo Scientific Inc.). Consecutive sections (500 μm apart) were mounted and examined

with a fluorescence microscope (Leica EL6000). For quantitative immunohistochemistry (Figure 2.1), free-floating sections were processed with 5% normal donkey serum, and 0.4% Triton X-100 for 60 min. Sections were then exposed at 4°C for 48 hr to primary antibodies against mouse monoclonal CaMKIIα (CaMKIIα, 1:500, 05-532, Millipore, Billerica, MA). After washing with PBS, sections incubated for 2 hr at room temperature with Alexa Fluor 647-conjugated AffiniPure donkey anti-mouse IgG (1:250, Jackson Laboratories, West Grove, PA). Slices were then washed and mounted (DAPI-Fluoromount G, SouthernBiotech, Birmingham, AL). Immuno-fluorescence was assessed with a laser confocal microscope (Leica CTR 6500).

For high-resolution, whole-brain fluorescence imaging (Figure 2.2A, Figure 2.9H, and Figure 2.5), frozen brains were embedded using stainless steel Tissue-Tek base molds and Neg-50 embedding medium (Richard-Allan Scientific (Thermo); n = 2 animals) [PTJ13]. Post-freezing, the Neg-50 embedded brain was sectioned on a Microm HM550 cryostat using the tape-transfer method with all sections mounted directly onto slides. Alternating sections, cut at 20 μm, were separated to form two distinct series per brain. One slide series of the sectioned material was processed for Nissl cell body staining, using a thionin-based protocol and coverslipped with DPX mounting medium. The alternate series was dehydrated and directly coverslipped with DPX for fluorescence imaging. Whole-slide digital imaging was performed using a Hamamatsu NanoZoomer 2.0-HT system at 0.46 μm/pixel, with fluorescence scans at 12-bit depth using a tri-pass filter cube. Following data conversion to lossless jp2 (JPEG2000), individual brain sections were aligned and registered using rigid 2-D image transformation.

2.2.10 Statistics

All statistical tests were performed in Matlab. Non-parametric tests were used throughout the analysis. For *in vivo* electrophysiology measurements at thalamus and zona incerta, one-tailed Wilcoxon signed-rank tests were used to evaluate changes in firing rate between the pre-stimulation and stimulation periods. For measurements at sensory cortex in Figure 2.7G, a two-tailed version of the test was used to evaluate either increases or decreases in firing rate. One-sided Wilcoxon rank sum tests were used to evaluate differences in SLO occurrence (Figure 2.9E), as well as

changes in cortical or incertal firing when eNpHR activation was coupled with central thalamus stimulation (Figure 2.11F,H). For electrophysiology results, independence was assumed between repeated trials. All other assumptions for these tests were satisfied. For volumetric comparisons in Figure 2.4E-G, one-sided Wilcoxon signed-rank tests were used to identify increases in the volume of BOLD activation between 10 and 40 Hz and 10 and 100 Hz (corrected for multiple comparisons). Note that variance was generally similar across groups being compared. Significance was determined at the $\alpha = 0.05$ cutoff level. No statistical methods were used to estimate sample size. All statistical tests used to compare changes with frequency (Figure 2.4E-G, and Figure 2.5B) were performed pairwise, with an equal number of animals used for each frequency.

2.3 Results

2.3.1 High-frequency stimulation of central thalamus relay neurons drives widespread forebrain activation *in vivo*

To investigate the specific role of central thalamus, we applied optogenetic techniques to control relay cells in a spatially and temporally precise manner. We performed a stereotactic injection in the right CL and PC intralaminar nuclei of central thalamus with adeno-associated virus carrying channelrhodopsin-2 (ChR2) and the fluorescent reporter protein EYFP under control of the CaMKIIα promoter. This promoter is expressed primarily in excitatory neurons, the vast majority of which in thalamus are relay cells [Smi08, EHK13]. 35% of cells identified within the bulk injection area were EYFP-positive, and 97% of EYFP-positive cells co-expressed CaMKIIα, indicating high sensitivity for stimulation of excitatory neurons (n = 2 rats, 831 cells; Figure 2.1). While ChR2-EYFP expression extended beyond these two nuclei (Figure 2.2A), targeted stimulation of the intralaminar nuclei was achieved by (a) stereotactic placement of the implanted optical fiber, as confirmed with high-resolution T2-weighted structural MR images (Figure 2.2B,C), and (b) spatially restricted illumination (Figure 2.2A,B). We initially injected and cannulated 47 rats using the central thalamus as the stereotactic target (-3.2 mm AP, +1.5 mm ML, -5.5 mm DV). However, the intralaminar nuclei are relatively small and difficult to accurately target. We there-

fore used only a subset of these animals based on the empirically observed distribution of optical fiber tip locations using T2-weighted MRI scans (Figure 2.2B; < 0.85 mm distance from target coordinate). Of the 18 rats that had an accurately localized implant location, two exhibited a general absence of fMRI activity - most notably at the site of stimulation - and were excluded, leaving 16 animals for further analysis.
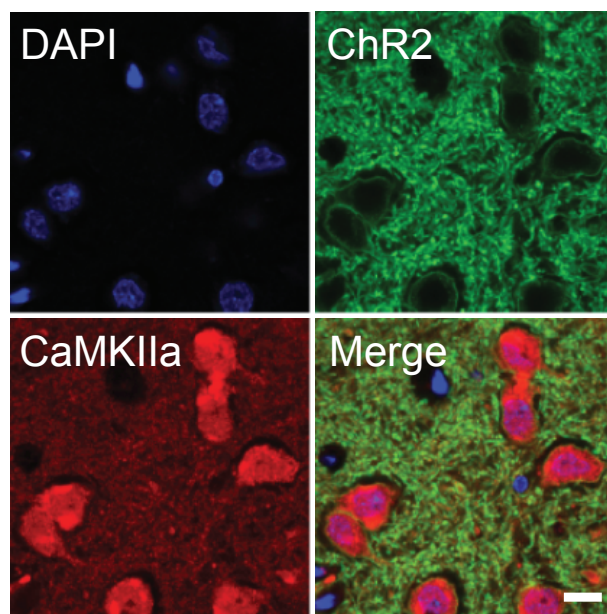
Figure 2.1: **Specificity of ChR2 targeting for CaMKIIα-positive cells.** *Immunohistochemistry confirms the specific targeting of ChR2-EYFP to CaMKIIα-positive neurons in central thalamus. 35% of cells identified within the bulk injection area were EYFP-positive, and 97% of EYFP-positive cells co-expressed CaMKIIα (n = 2 rats, 831 cells). Scale bar, 10 μm.*

In order to achieve a small volume of directly excited tissue limited to the intralaminar nuclei, we used a 62.5 μm diameter optical fiber. Assuming that an intensity of 1 mW/mm^2 is required for ChR2 activation [AWZ07], the specific power exiting from the fiber optic's tip in these experiments (2.5 mW) corresponds to a penetration depth of 1.08 mm and a volume of 0.08 mm^3 over which ChR2+ neurons can be excited. Figure 2.2A illustrates this penetration depth and activation cone (11.7 degree half-angle of divergence) to scale with the targeted nuclei, showing that stimulation is well restricted to the central thalamus. These two factors (MR-validated stereotactic fiber placement and a small volume of excited tissue) suggest that the effects reported here primarily derive from stimulation of excitatory relay neurons within the central thalamus.
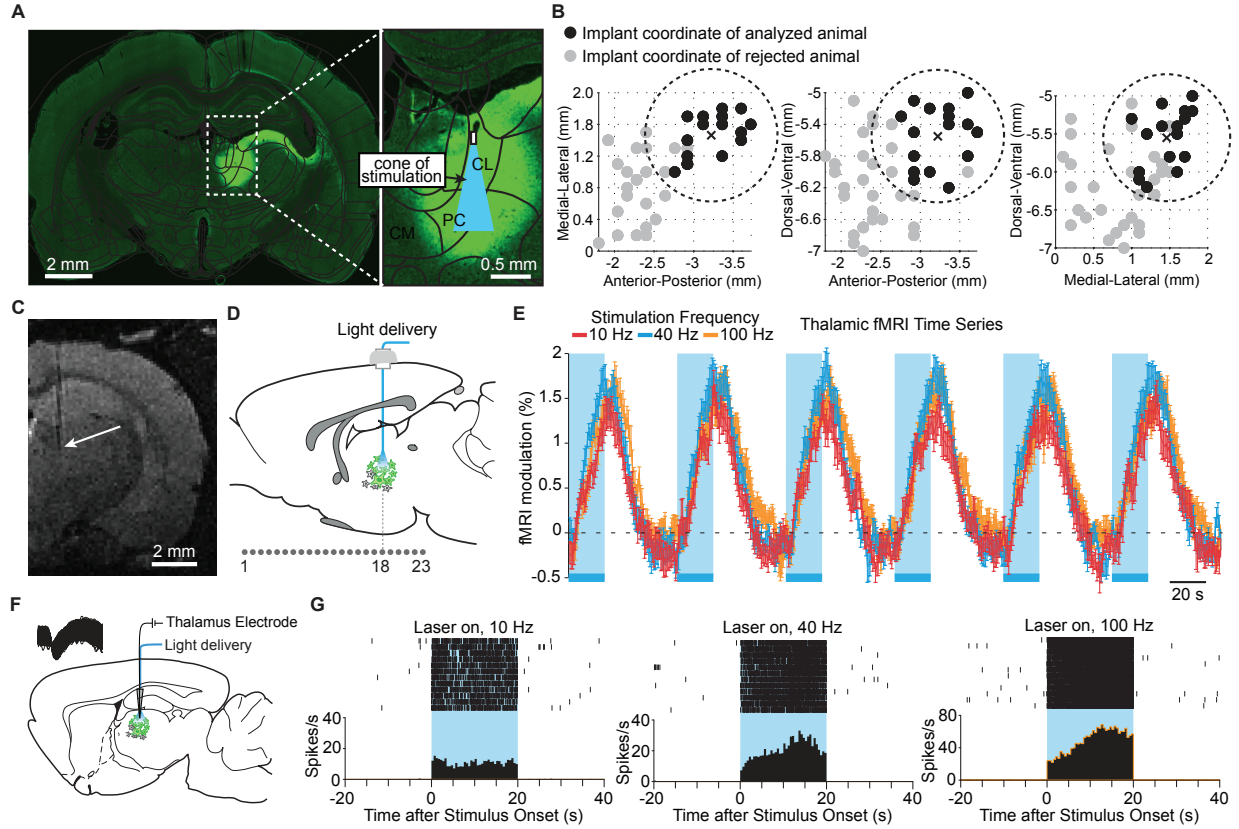
Figure 2.2: **Targeted stimulation of central thalamus evokes positive BOLD changes and increases in neuronal firing at the site of stimulation.** *(A) Representative wide-field fluorescence image shows robust ChR2-EYFP expression throughout central thalamus, overlaid with the estimated cone of excited tissue shown to scale. (B) Empirically observed locations of fiber optic implants in initial cohort of 47 rats, estimated using high-resolution structural MRI scans. 18 of these animals had implant locations that were accurately localized to the central thalamus (< 0.85 mm from target site, shown as dashed circle and cross). Two were excluded based on lack of thalamic activation, leaving n = 16 rats for further analysis. Black dots indicate implant coordinates of 16 animals used for analysis. Gray dots indicate implant coordinates of 31 rejected animals. (C) Representative T2-weighted anatomical MRI scan used to estimate implant location, marked with arrow. (D) Schematic of 23 coronal slices acquired during ofMRI experiments. Slice numbers correspond to activation maps in Figure 2.4. (E) Average time series of significantly modulated voxels within the ipsilateral thalamus ROI (see Figure 2.4D) exhibit robust positive BOLD responses during repeated 20 s periods of stimulation at 10, 40, and 100 Hz, indicated by blue bars. Values are mean s.e.m. across animals (n = 16, 10, and 16 for each frequency, respectively). (F) Diagram of local in vivo optrode recordings during optical stimulation of central thalamus. Inset shows spike waveforms of recorded neurons. (G) Representative peri-event time histogram of a recorded neuron showing the increase in firing rate within central thalamus during optical stimulation at each of the three frequencies tested.*

25

To explore the anatomical connectivity of transfected neurons in central thalamus, we collected *ex vivo* fluorescence microscopy images of ChR2-EYFP expression. Due to the spread of viral transfection (Figure 2.2A), it is possible that the reported fluorescence reflects projections from adjacent thalamic nuclei as well. Nevertheless, in agreement with known projection systems of central thalamus, EYFP-expressing axons were observed throughout forebrain, including frontal cortex and striatum (Figure 2.3). In particular, the medial prefrontal, lateral prefrontal, cingulate, motor, and sensory cortices all received strong projections. This input was highly convergent at the superficial layers, with moderate but weaker projections present in middle layers as well. Furthermore, projections were significantly restricted to the hemisphere ipsilateral to virus injection for both cortex and striatum. While these anatomical connections provide a strong foundation for understanding how central thalamus can influence brain state, they do little to explain the dynamic nature of these circuits - for example, how stimulation of central thalamus at different frequencies can lead to distinct behavioral responses [HJ49, VVV97]. Therefore, to dissect the functional significance of these massive forebrain projections and visualize the large-scale spatial and temporal dynamics evoked by central thalamus stimulation, we combined optical stimulation with simultaneous *in vivo* whole-brain functional imaging [LDG10].

During optogenetic fMRI experiments, twenty-three coronal slices with 0.5×0.5 mm^2 inplane resolution and 0.5 mm thickness were acquired at a frame rate of 750 ms using spiral k-space trajectories and a sliding window reconstruction algorithm to achieve high spatiotemporal resolutions with whole-brain coverage (bregma +5.2 to -5.3 mm; Figure 2.2D) [FL13]. Novel inverse Gauss-Newton methods were also used to correct for possible motion artifacts and optimize the robustness of detecting optogenetically-evoked responses [FL13]. For each experiment, we delivered 20 s periods of stimulation every minute for 6 minutes at 10, 40, or 100 Hz. This form of continuous steady-state stimulation mimics the approach used in clinical DBS and has been showed to evoke robust fMRI responses with optogenetic stimuli [LDG10, DCC15, WFL15]. Indeed, stimulation at all three frequencies resulted in a robust positive blood-oxygen-level-dependent (BOLD) signal at the site of stimulation that was highly synchronized to light delivery, increased upon optical activation, and gradually returned to baseline following the end of stimulation (Figure 2.2E). To confirm that this BOLD signal reflected underlying neuronal firing
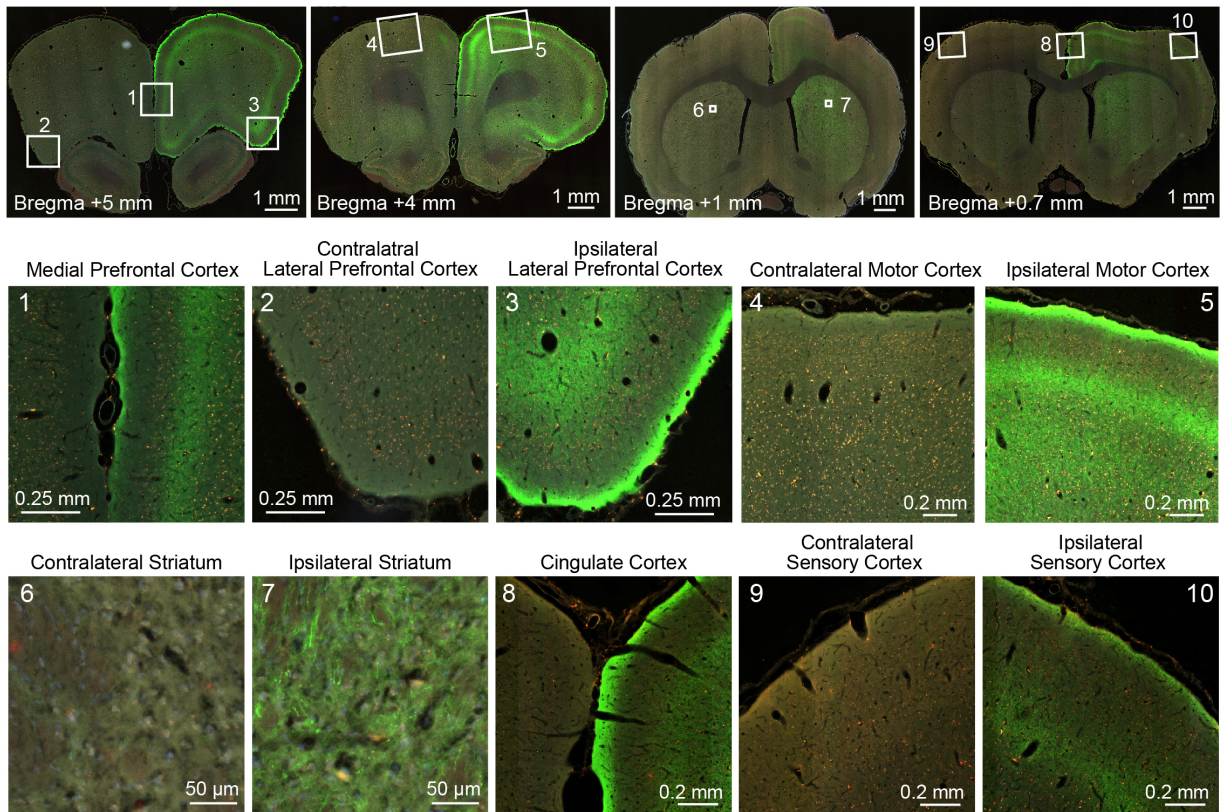
Figure 2.3: ***Representative fluorescence images of ChR2-EYFP at remote targets illustrate the massive projections to forebrain from transfected relay neurons in the right central thalamus.*** *The bottom two rows provide magnified images of cortical and striatal regions used for quantitative ofMRI analysis. The top row provides the whole-brain slices from which these magnified images come. EYFP-expressing axonal projections are primarily localized to the ipsilateral hemisphere and to superficial layers in cortex.*

patterns, we next performed simultaneous single-unit recordings with stimulation using an optrode at the central thalamus (Figure 2.2F). In agreement with the fMRI signal, stimulations at 10, 40, and 100 Hz all resulted in robust increases in the local neuronal firing rate (Figure 2.2G; n = 5 neurons, P < 0.05, Wilcoxon signed-rank test between the 20 s pre-stimulation and stimulation periods, 12 trials for each neuron).

Both locally in the thalamus and at downstream, synaptically connected brain regions, the frequency of stimulation was a critical parameter in determining the extent of ipsilateral and contralateral BOLD activation - defined here as positive BOLD signals significantly synchronized to the block stimulation paradigm. In general, a much larger volume of brain tissue was activated

by stimulation at 40 and 100 Hz compared to 10 Hz, with frontocortical areas and striatum being strongly activated at high frequencies (Figure 2.4A-C). To quantify these spatial differences in recruitment patterns, we calculated the total volume of positive and statistically significant BOLD signals evoked by stimulation in select ROIs (Figure 2.4D). This difference in activation volume between low (10 Hz) and high (40 or 100 Hz) stimulation frequencies was significant at the thalamus, striatum, and medial prefrontal, lateral prefrontal, cingulate, motor, and sensory cortices (Figure 2.4E-G). Striatal activity was primarily localized to the dorsal sector, with negligible activity occurring in the ventral region (Figure 2.4B,C). Furthermore, BOLD activation was generally restricted to the ipsilateral hemisphere, although activation volumes in the contralateral striatum, lateral prefrontal cortex, motor cortex, and sensory cortex were all significantly greater during 100 Hz stimulation compared to 10 Hz stimulation (Figure 2.4F-H).

These results provide a direct, region-specific visualization of the widespread driving effect that central thalamus has been shown to exert over forebrain, and link prior anatomical and physiological studies on arousal regulation to spatially precise and quantitative measures of cortical and striatal activation. For example, the evoked responses are consistent with the unilateral nature of thalamocortical projections (Figure 2.3), but reveal that the contralateral cortex can still be modulated by unilateral stimulation of central thalamus, particularly at high frequencies. Importantly, stimulation of other thalamic nuclei failed to evoke similarly widespread activity in the striatum and cortex (Figure 2.5A). Furthermore, large differences in forebrain activation between 10 and 40 Hz stimulations were not observed for other forms of subcortical stimulation (Figure 2.6B), suggesting this is a distinct property of central thalamus.

Throughout these experiments, a constant duty cycle of 30% was used to maintain the total amount of light delivery across frequencies and control for possible heating artifacts [CWS13]. Because we wished to keep a 20 s pulse train for all stimulation frequencies and avoid possible differences introduced by neuronal adaptation, maintaining a constant duty cycle required unique pulse widths for each frequency (i.e. 30, 7.5, and 3 ms for 10, 40, and 100 Hz, respectively). To rule out the possibility that these changes in pulse width were the primary cause of the above differences in forebrain recruitment, we repeated stimulations while maintaining a 3 ms pulse

28
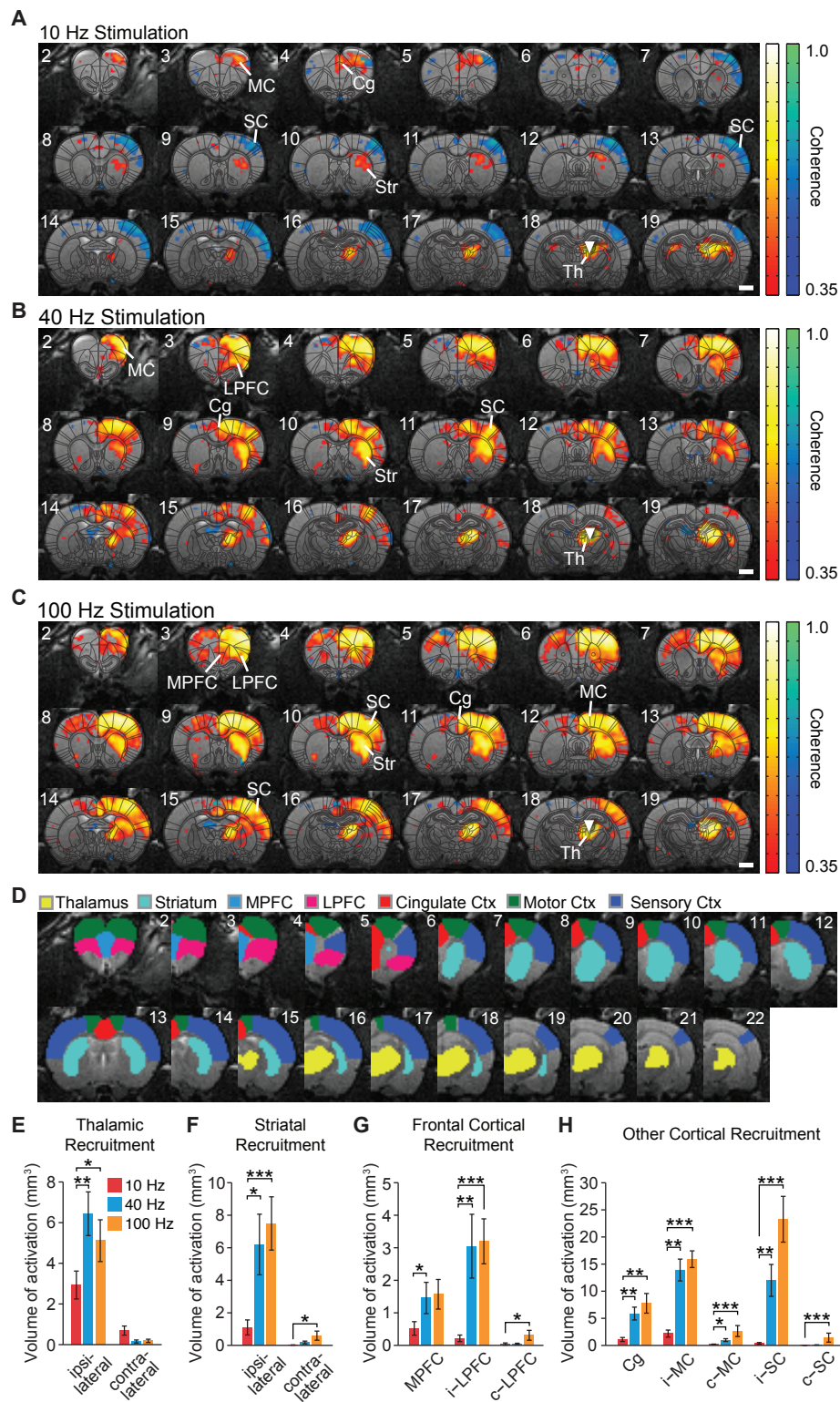
Figure 2.4:

Figure 2.4: ***Spatial characterization of evoked fMRI signals.*** *(A-C) Average coherence maps of brain-wide activity during stimulation of excitatory central thalamus relay neurons at 10, 40, and 100 Hz. Warm colors indicate positive BOLD responses, while cool colors indicate negative BOLD responses. (D) Regions of interest (ROIs) used for quantitative analysis of spatial ofMRI activation patterns. (E) The amount of active volume (positive signal with coherence>0.35) in the ipsilateral thalamus is significantly greater during 40 and 100 Hz stimulations than 10 Hz stimulation. Thalamic recruitment is relatively limited on the contralateral side. (F) Activation of the ipsilateral striatum is significantly greater during 40 and 100 Hz stimulations than 10 Hz stimulation. Activation of the contralateral striatum is limited across frequencies, although there is an increase from 10 to 100 Hz. (G) Medial and lateral prefrontal cortex exhibit a significantly greater volume of activation during 40 and/or 100 Hz stimulation than 10 Hz stimulation. Activity in the contralateral hemisphere is limited across all tested frequencies, although there is an increase from 10 to 100 Hz. (H) Activation of cingulate, motor, and somatosensory cortex is each greater during 40 and 100 Hz stimulations than 10 Hz stimulation. The contralateral motor and sensory cortices are also activated to a greater extent during 40 and/or 100 Hz stimulation. Scale bars in panels A through C represent 2 mm. Asterisks in panels E through H indicate significant differences for 10 versus 40 Hz and 10 versus 100 Hz stimulations. * P < 0.05, ** P < 0.005, *** P < 0.001, one-sided Wilcoxon signed-rank tests, corrected for multiple comparisons. Error bars represent mean s.e.m. across animals. n = 16, 10, and 16 animals for 10, 40, and 100 Hz, respectively. Abbreviations are as follows: i- (ipsilateral), c- (contralateral), Cg (cingulate cortex), MC (motor cortex), MPFC (medial prefrontal cortex), LPFC (lateral prefrontal cortex), SC (sensory cortex), Str (striatum), Th (thalamus).*

width. Visualization and quantification of evoked fMRI responses show that the increase in cortical and striatal activation with frequency was preserved (Figure 2.6A,B). These data suggest that stimulation frequency was the primary factor in modulating forebrain fMRI activation.

2.3.2 Central thalamus stimulation frequency controls cortical excitation/inhibition balance

We next examined the temporal dynamics of cortical responses evoked during low- and high-frequency central thalamus stimulation. Despite targeted activation of excitatory neurons, the somatosensory cortex exhibited a strong negative BOLD signal during 10 Hz stimulation, suggesting a suppression of baseline activity (Figure 2.4A and Figure 2.7A,B). In stark contrast, central thalamus stimulations at 40 and 100 Hz led to positive changes in the BOLD signal at the somatosensory cortex (Figure 2.4B,C and Figure 2.7A,B). Thus, stimulation of the same excitatory population at different frequencies resulted in completely opposite responses at a down-
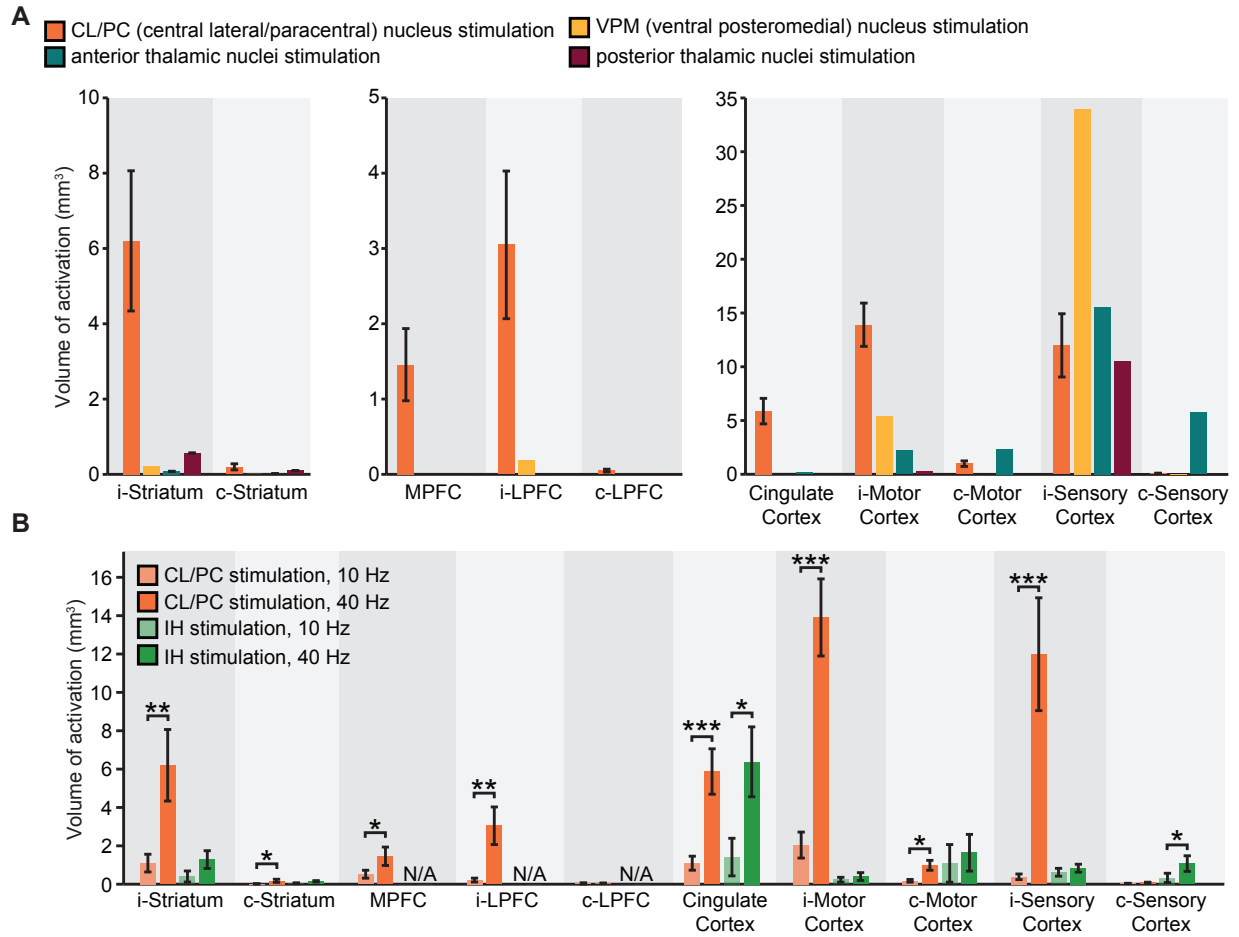
Figure 2.5: ***Widespread and frequency-dependent recruitment of forebrain with optogenetics is distinct to stimulation of intralaminar nuclei of central thalamus.*** *(A) Volumes of striatal and cortical activation (i.e. positive BOLD signals with coherence greater than 0.35) during 40 Hz stimulation of central thalamus, presented with activation volumes during stimulation of other thalamic nuclei. Central thalamus is the only target to result in significant recruitment of striatum and prefrontal and frontal cortical regions. (B) Comparison of frequency dependent effects of central thalamus stimulation with those of intermediate hippocampus (IH) stimulation. Unlike central thalamus stimulation, which recruits significantly more volume in striatum, motor cortex, and sensory cortex at 40 Hz than at 10 Hz (* P < 0.05, ** P < 0.005, *** P < 0.001; one-sided Wilcoxon signed-rank test), recruitment of these regions during hippocampal stimulation does not exhibit a significant dependence on frequency. Note that activation data was not available (N/A) at MPFC or LPFC for hippocampus stimulation due to differences in field of view. Abbreviations are as follows: i- (ipsilateral), c- (contralateral), Cing. ctx (cingulate cortex), MPFC (medial prefrontal cortex), LPFC (lateral prefrontal cortex), Sens. ctx (sensory cortex).*
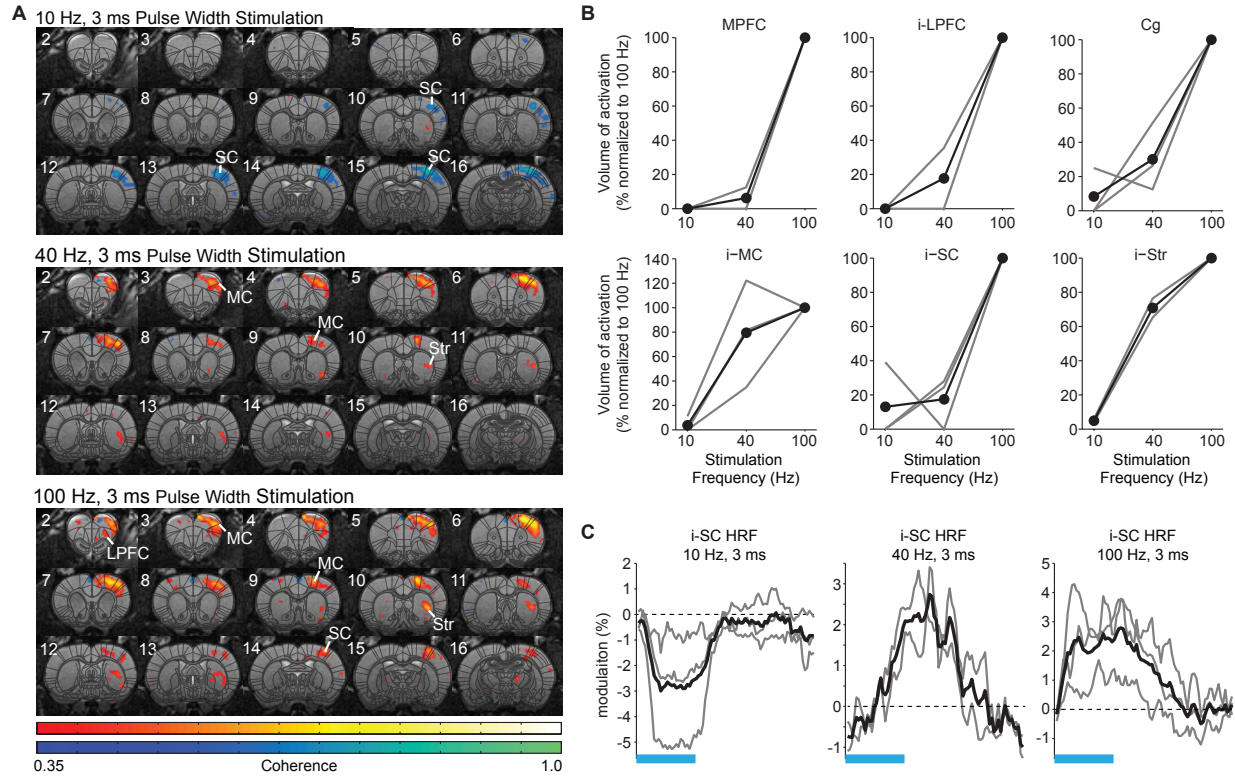
Figure 2.6: **The frequency-dependent recruitment of forebrain by central thalamus and its control over cortical BOLD signal polarity are preserved when pulse width is held constant.** *(A) Representative coherence map of brain-wide activity during stimulation of excitatory central thalamus relay neurons at 10, 40, and 100 Hz using a constant pulse width of 3 ms. Warm colors indicate positive BOLD responses, while cool colors indicate negative BOLD responses. (B) Quantification of positive BOLD responses in cortex and striatum (n = 3 animals). Gray lines indicate animal-specific results, normalized to 100 Hz stimulation. Black lines indicate the average across animals. All six regions exhibit an increase in recruitment with frequency, consistent with the study's main results when pulse width was varied to keep the duty cycle and total amount of light delivery constant. ROIs are the same as those used in Figure 2.4. (C) Hemodynamic response functions evoked in somatosensory cortex during 10, 40, and 100 Hz stimulation of central thalamus using a constant pulse width of 3 ms. Consistent with the study's main results, a negative BOLD signal is evoked at 10 Hz, while slow and fast positive BOLD responses are evoked at 40 and 100 Hz, respectively.*

stream target. Importantly, these responses were preserved when pulse width was held constant in control experiments, indicating that stimulation frequency was the primary factor controlling this effect (Figure 2.6A,C).

While previous studies have hinted at similar findings of frequency-dependent polarity changes [LAM10, WFL15], downstream positive and negative BOLD signals that result from selective stimulation of excitatory neurons at distinct frequencies have not yet been visualized and validated with electrophysiology. To define the neuronal underpinnings of these signals, we therefore performed single-unit extracellular recordings in the somatosensory cortex during central thalamus stimulation (Figure 2.7C). In agreement with the BOLD activity observed during ofMRI experiments, 10 Hz stimulation resulted in a decrease in neuronal firing rate between pre-stimulation and stimulation periods (Figure 2.7D,E; n = 9 of 11 recorded neurons). Conversely, stimulations at 40 and 100 Hz both led to increases in neuronal firing (Figure 2.7D,E; n = 11 of 11 recorded neurons). Because the evoked firing rates appeared to change over the course of stimulation, we specifically compared the pre-stimulation firing rate to the average firing rates during consecutive 5 s periods of the 20 s stimulus (i.e. 0-5 s, 5-10 s, 10-15 s, and 15-20 s; uncorrected P < 0.05, Wilcoxon signed rank test; 17 trials for each neuron). Interestingly, the decrease in firing rate during 10 Hz stimulation occurred primarily over the interval from 5 to 15 s after stimulation began, while the increase in firing rate during 40 Hz stimulation occurred primarily over the first 10 s. On the other hand, the increase in neuronal firing rate during 100 Hz stimulation was generally maintained throughout the 20 s stimulation period. Such differences may reflect short-term plasticity of the thalamocortical pathway, which has previously been shown to exhibit frequency-dependent properties [CC96a, CC96c]. Peri-stimulus time histograms also revealed that spike events occurring during inhibition had a non-uniform distribution over time, which peaked between 6 and 34 ms after light onset (Figure 2.8). These data suggest that the glutamatergic thalamocortical input at 10 Hz sometimes generated action potentials. Notably, however, not every light pulse resulted in an immediate action potential.

Together, these ofMRI and electrophysiological data indicate that neuronal activity throughout somatosensory cortex is suppressed at low frequencies of central thalamus stimulation and
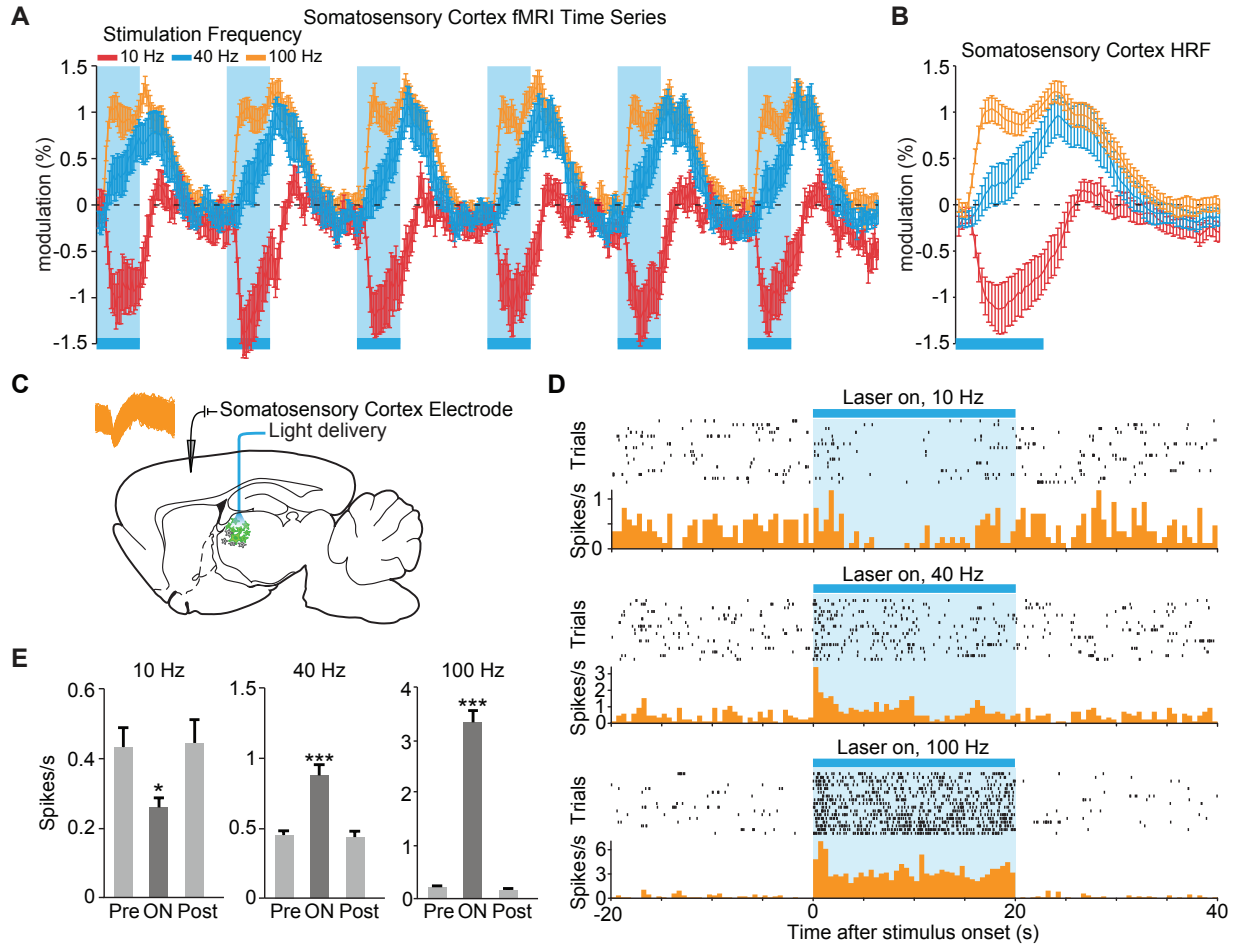
Figure 2.7: **The sign of evoked cortical activity depends on the frequency of central thalamic stimulation.** *(A,B) 10 Hz stimulation of central thalamus evokes a strong negative BOLD signal throughout ipsilateral somatosensory cortex, while 40 and 100 Hz stimulations evoke positive responses. Time series come from the sensory cortex ROI defined in Figure 2.4D. Hemodynamic response function (HRF) shows the average response to a single 20 s period of stimulation, indicated by blue bar. Error bars represent mean s.e.m. across animals. n = 16, 10, and 16 for 10, 40, and 100 Hz, respectively. (C) Diagram of in vivo recordings at somatosensory cortex during stimulation of excitatory central thalamus relay neurons. Inset shows spike waveforms of recorded neurons. (D,E) Representative peri-event time histogram of a recorded neuron, and corresponding quantification of firing rate during the 20 s periods before, during, and after stimulation. Neural firing rate decreased within the somatosensory cortex during 10 Hz central thalamus stimulation, but increased during 40 and 100 Hz stimulations (n = 17 trials each, * P < 0.05, *** P < 0.001 pre vs. ON, two-tailed Wilcoxon signed-rank test). Values are mean s.e.m.*
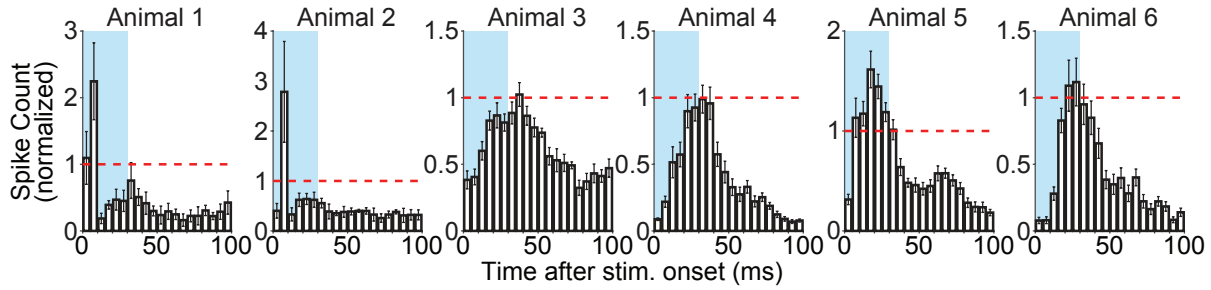
	Pre-stimulation firing rate (Hz)	Suppressed firing rate (Hz)	Peak latency (ms)	Spike fidelity (%)	Number of cells
Animal 1	2.2 ± 0.6	1.2 ± 0.4	5.8 ± 1.1	5.0 ± 1.4	6
Animal 2	5.6 ± 1.5	3.3 ± 1.3	7.5 ± 0.0	14.6 ± 6.3	4
Animal 3	10.6 ± 1.9	6.6 ± 1.2	33.5 ± 3.2	14.1 ± 2.1	10
Animal 4	14.0 ± 2.3	6.3 ± 1.3	32.5 ± 2.6	17.3 ± 3.3	23
Animal 5	12.4 ± 2.1	8.4 ± 1.6	21.9 ± 3.3	31.3 ± 4.7	18
Animal 6	8.4 ± 2.1	4.2 ± 1.2	26.9 ± 2.3	11.2 ± 2.5	17

Figure 2.8: ***Cortical spikes that occur during periods of inhibition driven by 10 Hz central thalamus stimulation exhibit a non-uniform distribution over time.*** *(Top figure) Average peristimulus time histograms (PSTHs) of spike events in somatosensory cortex during 10 Hz central thalamus stimulation for six animals. Analysis was restricted to the 5 s time bin with the greatest number of neurons inhibited for each animal. PSTHs were calculated by aligning spike counts to the onset of individual 30 ms light pulses, summing over the 50 pulses delivered during the 5 s stimulation period, averaging across trials, and binning at 5 ms intervals for each inhibited neuron. Histograms were normalized by the corresponding spike count value during the 20 s pre-stimulation baseline period (represented by the dashed red line), and averaged across neurons for each animal. Blue rectangles represent the 30 ms light pulse. Note that spike events are reduced relative to baseline for the majority of the 100 ms inter-stimulus period, but spike events that do occur have a non-uniform distribution that peaks 6-34 ms after stimulus onset. These patterns suggest that some thalamic stimuli induce spike events in cortex, despite the net suppression of activity relative to pre-stimulation levels. Animals presented include four used for combined ChR2-eNpHR electrophysiology experiments in Figure 2.11. (Bottom table) Summary of PSTH peak latencies and spike fidelity for inhibited neurons in somatosensory cortex. Peak latency was defined as the 5 ms bin with highest spike count for each neuron's PSTH. Spike fidelity represents the percentage of light pulses in the given 5 s bin of inhibition that evoke at least one spike during the 30 ms pulse. Values represent mean $\pm$ s.t.e. across cells in the figure and table.*

increased at high frequencies of stimulation. Because our stimulations were restricted to excitatory neurons with cell bodies located in central thalamus, the causal relationship between stimulation frequency and cortical excitation/inhibition can be attributed to the neurons' initial firing pattern. These results add to a growing body of literature in systems neuroscience suggesting that a neuronal population's firing pattern can have vastly different - even opposite - effects on downstream regions depending on its specific temporal code [DM43, LAM10, MBE14, WFL15].

2.3.3 Low-frequency central thalamus stimulation drives incertal oscillations

Given that stimulation was restricted to excitatory neurons, we hypothesized that the suppression of cortex during 10 Hz stimulation might be related to the frequency-dependent modulation of a GABAergic population. We chose to investigate the response properties of the zona incerta (ZI), which has been implicated in providing a powerful GABAergic modulation of 10 Hz spike-wave activity in spontaneous absence seizures in the rat [SLC13]. Anatomically, ZI sends direct GABAergic projections to somatosensory thalamic nuclei and sensory cortex [NCL95, KM99, BFA02]. Functionally, ZI has also been shown to selectively gate sensory information processing in higher-order thalamic nuclei through GABAergic inhibition [TK04, LUD05, TBM06]. To investigate the involvement of zona incerta, we performed single-unit and field potential electrophysiology recordings in this region during simultaneous optogenetic stimulation of central thalamus at 10 or 40 Hz (Figure 2.9A). EEG recordings were simultaneously collected in frontal cortex to directly evaluate the relationship between ZI activity and whole-brain arousal state, which is typically measured with forebrain EEG. The zona incerta was targeted using stereotactic localization and the well-defined somatotopic representation of this region [NCL92]. The electrode was targeted to -3.96 mm AP, +2.2-2.6 mm ML, +6.7-7.2 mm DV from dura. The zona incerta was identified according to a compatible depth reading, spike latencies consistent with a polysynaptic response (on the order of 10 ms; Figure 2.9B), and a receptive field that responds to contralateral whisker stimulation, which zona incerta is known to possess [NCL92]. The electrode was initially lowered through the dorsal part of the VP thalamus (approximately 1.5 mm above zona incerta), which also responds to whisker stimulation, until the recorded neurons did
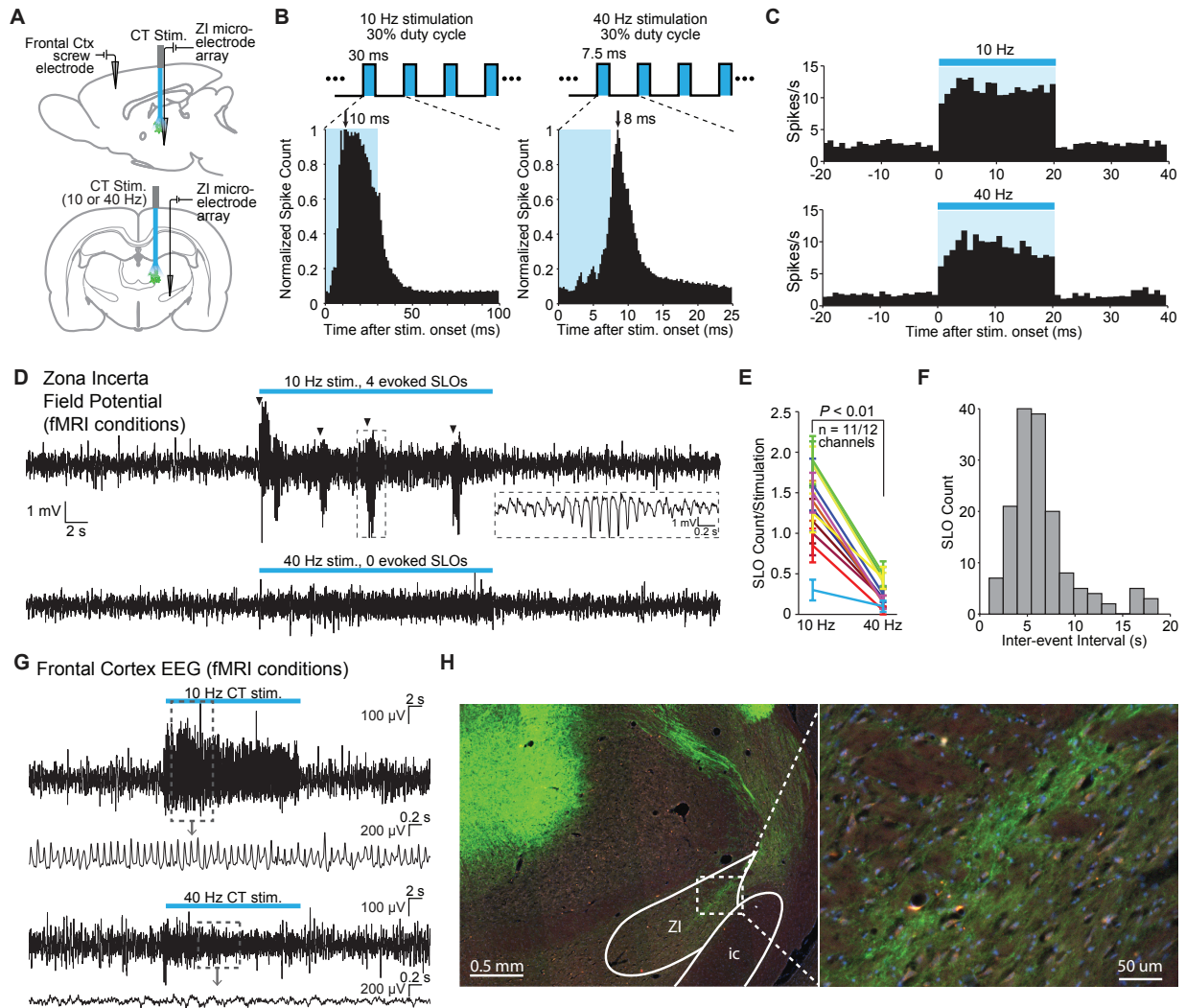
Figure 2.9: ***Frequency-dependent spindle-like oscillations are evoked in zona incerta (ZI).***
(A) Diagram of in vivo recordings at zona incerta and simultaneous EEG recordings in frontal cortex during optical stimulation of central thalamus in anesthetized animals. (B) Representative peri-event time histograms of spiking activity from recorded ZI neurons aligned to the onset of individual light pulses, summed over all pulses and trials. Peak spike latencies are approximately 10 and 8 ms for 10 Hz (left) and 40 Hz (right) stimulations, suggesting that recordings are performed at least one synapse away from the stimulated population in central thalamus. Schematics at top illustrate the 30% duty cycle pulse trains which lasted 20 s for each frequency. (C) Representative peri-event time histograms over the 20 s period of stimulation show increases in ZI firing during 10 and 40 Hz stimulations. Among the 28 isolated single-units in zona incerta (n = 2 animals), most exhibited a significant increase in firing rate during stimulation (n = 26 and 22 out of 28 neurons, respectively; P < 0.05, one-tailed Wilcoxon signed-rank test with 20 trials for each cell). (D) Representative field potential recordings from the same channel and trial number during 10 Hz (top) and 40 Hz (bottom) stimulation of central thalamus. Four amplitude-modulated, spindle-like oscillations (SLOs) are evoked during 10 Hz stimulation (marked by black triangles), while none are evoked during 40 Hz stimulation. Inset shows a zoomed-in SLO.

37

Figure 2.9: *(E) The number of SLOs was greater during 10 Hz stimulation than 40 Hz stimulation across 11 of 12 available channels (n = 2 animals, 20 trials each, P < 0.01, one-tailed Wilcoxon rank sum test). (F) When more than one SLO was evoked within the same 20 s period of 10 Hz stimulation, the distribution of inter-event intervals was centered at 6.6 ± 0.2 s (s.e.m.). (G) Representative EEG recordings collected in frontal cortex during central thalamus stimulation and simultaneous ZI recordings. 10 Hz stimulation evokes a spike-wave response, which is associated with loss of consciousness and perceptual awareness, while 40 Hz stimulation evokes a low-voltage fast response indicative of arousal. (H) ChR2-positive processes were observed in zona incerta, providing a basis for its recruitment during stimulation of central thalamus. i.c.: internal capsule.*

not respond to such a stimulus. The electrode was then lowered for another 1.5 mm until the recorded neurons fired in response to whisker stimulation, indicating the zona incerta had been reached.

Out of 28 isolated ZI neurons, the majority exhibited increases in their firing rate during central thalamus stimulation at both 10 and 40 Hz (Figure 2.9C; n = 26 and 22, respectively; $P < 0.05$, Wilcoxon signed rank test between the 20 s pre-stimulation and stimulation periods, 20 trials for each neuron). However, a key difference was that large, amplitude-modulated spindle-like oscillations (SLOs) in the field potential occurred significantly more often during 10 Hz stimulation than 40 Hz stimulation (Figure 2.9D,E). These oscillations exhibited an inter-event interval centered around 6.6 ± 0.2 s (s.e.m.), similar to those observed in thalamus during sleep onset [CDS97] (Figure 2.9F). Consistent with this, simultaneous EEG recordings in frontal cortex revealed strong spike-wave modulation during 10 Hz stimulation and lower amplitude, fast oscillations during 40 Hz stimulation, which are associated with loss of consciousness and aroused brain states, respectively (Figure 2.9G). EYFP-expressing axons were also observed in zona incerta (Figure 2.9H), indicating that central thalamus relay neurons may have direct connections to zona incerta and providing a possible anatomical substrate for these responses.

2.3.4 Cortical inhibition driven by central thalamus stimulation depends on evoked incertal activity

The observation of spindle-like oscillations in zona incerta during 10, but not 40, Hz central thalamus stimulation indicates that this region can be uniquely engaged by central thalamus-driven networks. However, it remains unknown whether the evoked activity in zona incerta plays a causal role in driving the frequency-dependent inhibition of somatosensory cortex. To address this question, we injected the inhibitory opsin halorhodopsin (eNpHR) fused to the mCherry fluorescent marker and controlled by the pan-neuronal hSyn promoter into zona incerta of four animals expressing ChR2-EYFP in central thalamus (Figure 2.10,Figure 2.11A,B,). Two new stimulation paradigms were explored: (1) 20 or 30 s continuous eNpHR activation, and (2) 20 s, 10 Hz central thalamus stimulation performed within a 30 s period of continuous eNpHR activation. Single-unit recordings were performed simultaneously at the zona incerta and sensory cortex during concurrent activation of these two opsins (Figure 2.11C).
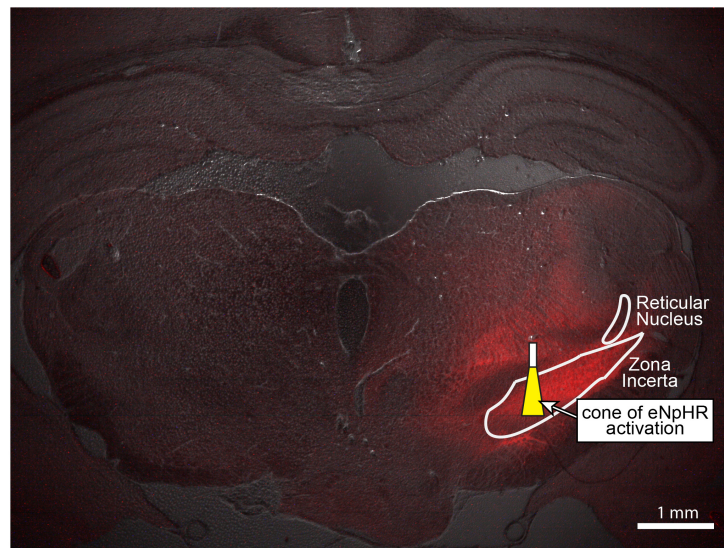
Figure 2.10: ***Wide-field fluorescence image of eNpHR expression in zona incerta, overlaid with the estimated cone of activated eNpHR (i.e. inhibited neurons) shown to scale.*** *Penetration depth and volume were calculated to be 0.64 mm and 0.024 mm^3, respectively, using the methods described in (54) and a threshold light intensity of 5 mW/mm^2 (104). The optical fiber had a diameter of 105 μm, NA of 0.22, and half-angle of divergence of 9.3°. Penetration depth and activation volume correspond to an optical power of 3 mW exiting the fiber optic's tip. Stimulation coordinate corresponds to -3.96 mm AP, +2.4 mm ML, and -6.7 mm DV. The thalamic reticular nucleus, another region of dense GABAergic neurons, is shown for reference.*

Among the 70 neurons recorded in zona incerta, delivery of 593 nm light resulted in a decrease in firing for 62 cells ($P < 0.05$, Wilcoxon signed rank test between 20 s pre-stimulation period and 20 or 30 s stimulation period, 15-20 trials for each neuron), indicating that illumination of halorhodopsin was successful in suppressing incertal activity. The evoked decrease in neuronal firing rate typically lasted throughout the duration of 593 nm light delivery (Figure 2.11D). When halorhodopsin activation in ZI was paired with 10 Hz stimulation of central thalamus, the previously described increase in incertal firing (Figure 2.9C) was disrupted. In 60 out of 70 neurons, the difference in incertal firing rate between the 20 s 10 Hz central thalamus stimulation period and the pre-stimulation period was significantly reduced with concurrent eNpHR activation (Figure 2.11F; $P < 0.05$, one-sided Wilcoxon rank sum test, n = 10-20 trials). Figure 2.11E illustrates the suppression of zona incerta activity throughout the 20 s period of 10 Hz central thalamus stimulation in a representative neuron. These data indicate that activation of halorhodopsin significantly suppressed the incertal firing evoked by 10 Hz central thalamus stimulation, and successfully disrupted incertal processing.

To determine whether this suppression of zona incerta affected the cortical activity driven by central thalamus stimulation, we quantified the changes in somatosensory cortex firing rate evoked by ChR2 activation with and without illumination of eNpHR. 76 somatosensory cortex neurons were recorded, and the 20 s period of central thalamus stimulation was divided into four 5 s bins as before. Consistent with the data presented in Figure 2.7, 68 cells (89%) exhibited a decrease in firing during 10 Hz stimulation of central thalamus (uncorrected $P < 0.05$, Wilcoxon signed rank test; 10-15 trials for each neuron). Strikingly, however, suppression of zona incerta activity with eNpHR reversed this effect. Across animals, 50 out of 76 neurons (66%) exhibited reduced inhibition when central thalamus stimulation was paired with eNpHR activation (Figure 2.11H; $P < 0.05$, Wilcoxon rank sum test over 1 s bins; 10-20 trials for each neuron). Indeed, a fraction of cells switched from inhibitory responses to excitatory ones. Figure 2.11G illustrates the firing patterns of one cell that exhibited an inhibitory response during 10 Hz central thalamus stimulation that was eliminated when zona incerta was simultaneously suppressed with eNpHR. Collectively, these data suggest that incertal activity during 10 Hz central thalamus stimulation has a net inhibitory effect on somatosensory cortex. In support of this influence being through di-
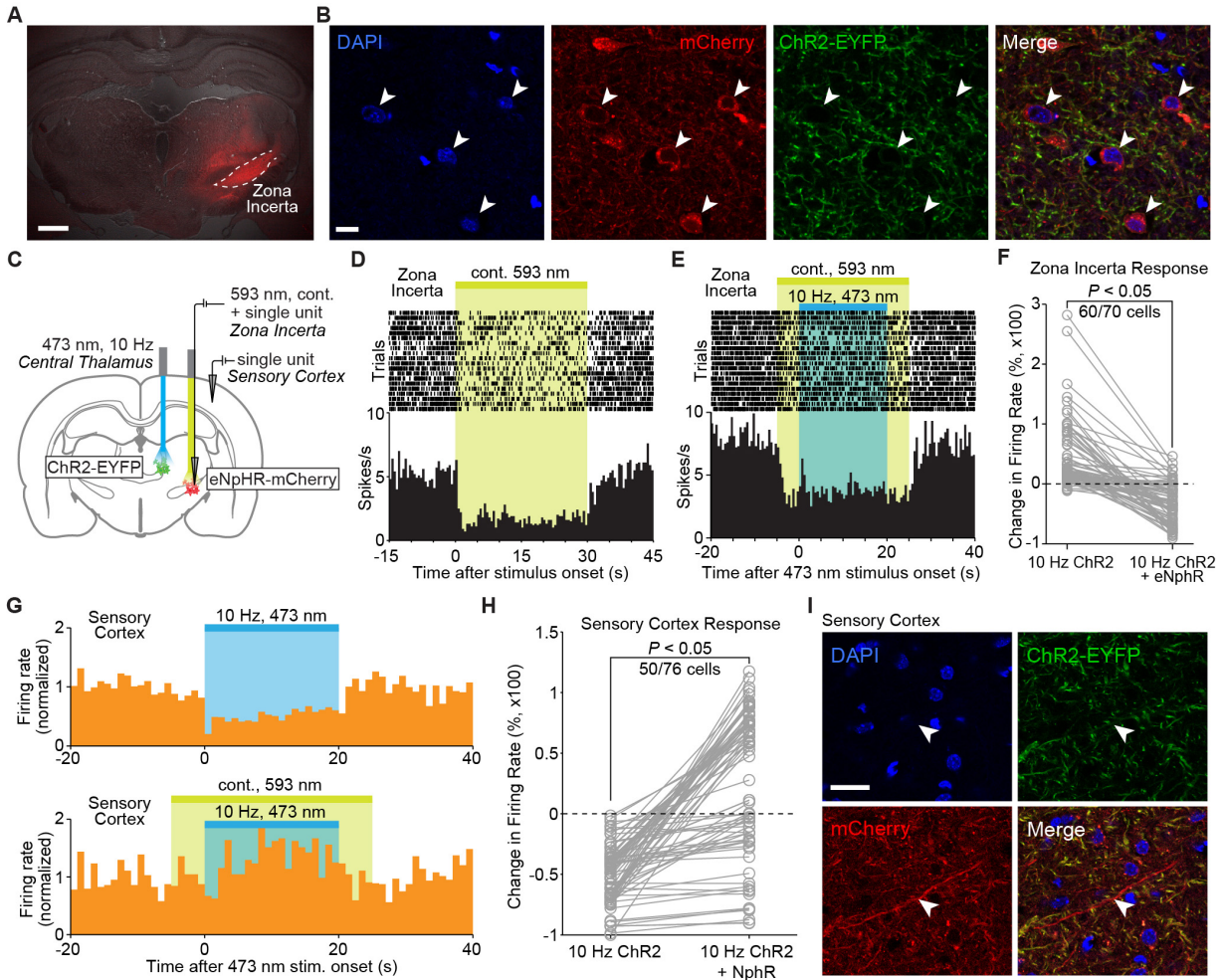
Figure 2.11: ***Cortical inhibition driven by 10 Hz central thalamus stimulation depends on normal incertal processing.*** *(A) Wide-field fluorescence image shows robust eNpHR-mCherry expression spatially localized to the right zona incerta. Scale bar, 1 mm. (B) Confocal images show eNpHR-mCherry localized to somatic membrane of neurons in zona incerta. Scale bar, 10 μm. 209 out of 882 DAPI-stained cells co-expressed mCherry in ZI (24%, n = 2 animals). (C) Schematic of cortical electrophysiology recordings during 10 Hz stimulation of central thalamus and continuous (cont.) inhibition of zona incerta using ChR2 and eNpHR, respectively. (D) Peri-event time histogram of a representative neuron in zona incerta whose firing rate is suppressed during activation of eNpHR with 593 nm light. (E) Peri-event time histogram of a representative neuron in zona incerta whose firing rate remains suppressed throughout the period of 10 Hz central thalamus stimulation during eNpHR activation (compare to Figure 2.9C). (F) Activation of eNpHR in zona incerta significantly reduces the change in incertal firing rate evoked by 10 Hz central thalamus stimulation in 60 of 70 neurons (P < 0.05, one-sided Wilcoxon rank sum test). Changes in firing rate are normalized to pre-stimulation levels. (G) Peri-event time histograms from a representative cortical neuron show that the inhibitory response evoked by 10 Hz central thalamus stimulation is reversed by simultaneously suppressing activity in zona incerta. Firing rates are normalized to the average pre-stimulation values.*

Figure 2.11: *(H) Quantification of evoked changes in cortical firing rate during 10 Hz central thalamus stimulation with and without concurrent eNpHR activation. 50 out of 76 cells exhibit reduced inhibition when central thalamus stimulation is paired with eNpHR activation (P < 0.05, Wilcoxon rank sum test over 1 s bins). Changes in firing rate are normalized to pre-stimulation levels. (I) Confocal images show mCherry-positive axonal projections from zona incerta in somatosensory cortex. Scale bar, 20 μm.*

rect anatomical connections, mCherry-positive axons were observed in the sensory cortex (Figure 2.11I), consistent with previous reports of incerto-cortical projections [LNS90]. These findings present a conceptually novel role of zona incerta in central thalamus arousal circuits.

2.3.5 Central thalamus stimulation modulates brain state in a frequency-dependent manner

Finally, to relate these findings more directly to behavior associated with central thalamus arousal circuits and previous electrical stimulation studies, we performed 10, 40, and 100 Hz stimulations in asleep, unanaesthetized animals with simultaneous video and EEG recordings. Control (pre-stimulus) activity was consistent across frequencies of stimulation, as quantified with EEG band power in delta, theta, alpha, and beta bands (Figure 2.12). During 10 Hz stimulation, the majority of animals exhibited behavior indicative of an absence seizure, including freezing and behavioral arrest throughout stimulation followed by a return to sleep (Figure 2.13A; n = 4/7). In addition, the most common EEG response was a transition to slow spike-wave discharges (Figure 2.13B,C; n = 5/7), which are typically associated with loss of consciousness [MV65]. In stark contrast, stimulations at 40 and 100 Hz resulted in behavioral transitions to an awake state, reflected by exploration and goal-directed movement (Figure 2.13A; n = 4/7 and 4/6, respectively). Similarly, the most common EEG pattern evoked by these high-frequency stimulations was a low-voltage-fast response (Figure 2.13B; n = 3/7 and 6/6, respectively), indicative of cortical activation and desynchronization. Collectively, these phenomena are consistent with the patterns of cortical and striatal recruitment observed with ofMRI. Moreover, the slow spike-wave and low-voltage-fast EEG responses evoked during behavioral experiments (Figure 2.13C,D) match those recorded under anesthetized conditions (Figure 2.9G), further linking the network activation pat-

terns revealed by ofMRI to the arousal responses reported here, as well as those reported in early stimulation studies (e.g. [HJ49]).
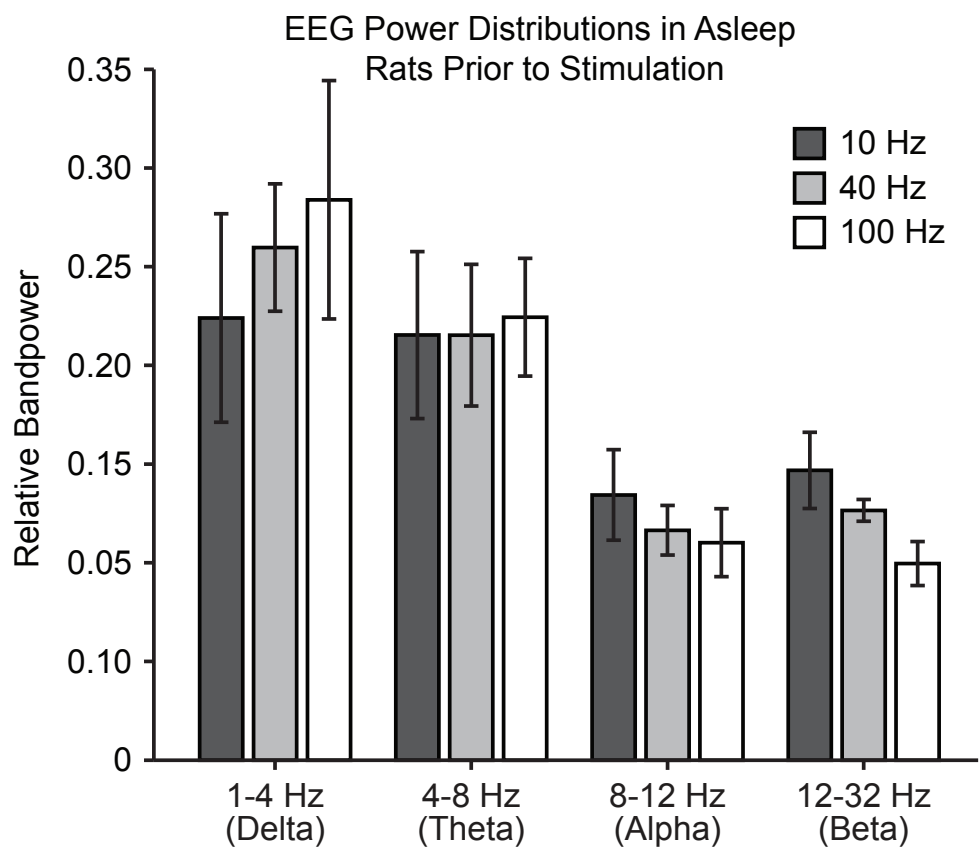
Figure 2.12: **Pre-stimulus activity is consistent across frequencies of stimulation in asleep rats, as quantified with EEG bandpower in delta, theta, alpha, and beta bands.**
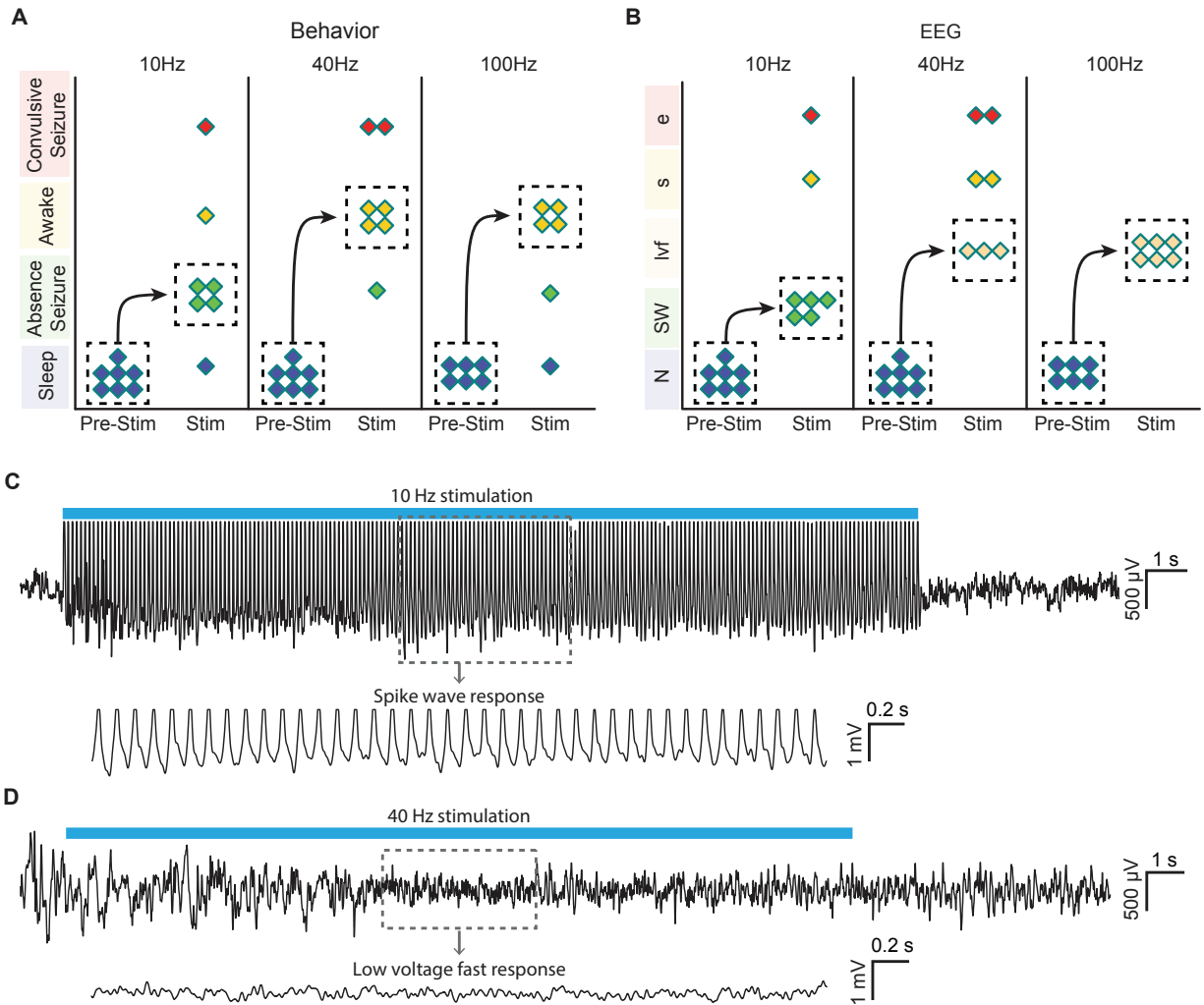
Figure 2.13: **Optogenetic stimulation of central thalamus in asleep animals modulates brain state in a frequency-dependent manner.** *(A) Low-frequency stimulation (10 Hz) in a majority of animals (n = 4/7) evokes behavioral absence seizures, while high-frequency stimulations (40 and 100 Hz) cause a majority of animals to awaken (n = 4/7 and 4/6, respectively). Dashed boxes indicate the most common response for each frequency, with arrows indicating the corresponding transition from sleep. (B) Low-frequency stimulation typically evokes spike-wave responses in EEG (n = 5/7), consistent with the behavioral reading of absence seizures. The most frequent EEG response during high-frequency stimulations is low voltage fast (n = 3/7 and 6/6), indicative of arousal. N, normal. SW, spike-wave. lvf, low voltage fast. s, spiking. e, evolving seizure. (C,D) Representative traces of EEG responses classified as spike-wave and low voltage fast. Insets show 4 s magnification. Importantly, these EEG patterns match those recorded under anesthetized conditions (Figure 2.9G), further linking the responses visualized with ofMRI to the reported behavioral responses.*

2.4 Discussion

Previously proposed mechanisms of arousal regulation have focused on the physiological and anatomical specialization of neurons within central thalamus [Sch08]. Here, using a combination of ofMRI and electrophysiological recordings, we directly visualize whole-brain network activations produced by selective stimulation of central thalamus relay neurons and reveal novel insight into frequency-dependent gating of forebrain arousal.

Since the earliest observations that electrical stimulation of central thalamus exerts frequency-dependent effects on behavior and EEG rhythms [MM49, HJ49], behavioral arousal and cognition have been tightly linked with cortical activation (i.e. low-amplitude, high-frequency oscillations), while behavioral arrest has been linked with cortical deactivation (i.e. high-amplitude, low-frequency oscillations). More recently, it has also been shown that pharmacologically-induced changes in thalamic firing levels can switch cortical dynamics between activation and deactivation [HC10]. However, no studies have characterized the specific changes in activity that simultaneously occur across the whole intact brain during these events to explain how the same neuronal population can selectively switch arousal state. Here, we show that distinct firing patterns of excitatory neurons in the central thalamus drive these opposing EEG rhythms, lead to dramatic differences in the spatial extent of forebrain recruitment, and switch the region's downstream influence on cortex from excitation to inhibition. Notably, high-frequency EEG patterns evoked during 40 and 100 Hz stimulation associate with robust activation of frontal cortex, motor cortex, somatosensory cortex, and striatum - regions that receive widespread glutamatergic projections from intralaminar nuclei [JL74, BG90, GB94, SRP04, HV07, HLK14]. On the other hand, slow-wave oscillations evoked during 10 Hz stimulation are associated with limited forebrain activation and strong inhibition of somatosensory cortex. The frequency-dependent generation of spindle-like oscillations, which are known to underlie brain synchronization at the onset of sleep [SMS93], suggest that these differences may in part be due to the engagement of thalamocortical networks responsible for sleep and loss of perceptual awareness during 10 Hz stimulation. In the context of our findings, it is also noteworthy that for some rat strains with absence seizures, a specific 10 Hz generator in somatosensory cortex has been independently

45

proposed [LS06].

The broadly contrasting cortical responses between low and high frequencies of central thalamus stimulation imply the frequency-dependent activation of a GABAergic population. In this study, we investigated the behavior of zona incerta - a region rich in GABAergic neurons that also sends direct inhibitory projections to sensory thalamus and sensory cortex [LNS90, BIG92, NCL95, KM99, BFA02]. We found that spindle-like oscillations were uniquely evoked when central thalamus was stimulated at 10 Hz and somatosensory cortex was inhibited. Stimulation at this frequency in asleep rats also evoked absence seizure-like freezing and spike-waves in a majority of animals, a cortical pattern known to be modulated by zona incerta projections [SLC13]. Importantly, suppressing the incertal activity evoked by 10 Hz central thalamus stimulation with halorhodopsin reduced the cortical inhibition (Figure 2.11H), suggesting a key role for zona incerta in modulating this response. Indeed, it has previously been suggested that rhythmic incertal activity contributes to membrane hyperpolarizations and sustained high-voltage cortical rhythms through GABAergic incertofugal pathways [SLC13]. Our data support this hypothesis, and link such a pathway to whole-brain, directly visualized fMRI activity patterns.

Given the presence of GABAergic projections from zona incerta to central thalamus [BFA02], activity in zona incerta may also act to limit forebrain activation, as observed with ofMRI during 10 Hz stimulation, through incertal-thalamic feedback. This incerto-thalamic pathway would parallel the previously reported gating of ascending sensory information at the level of thalamus by zona incerta [TK04, LUD05]. The hypothesized feedforward and feedback inhibition via zona incerta both suggest a direct projection from central thalamus to ZI, which our fluorescence imaging data support (Figure 2.9H). However, we note that previous tracing studies failed to identify thalamic input specifically from intralaminar nuclei to zona incerta [SNR85]. In summary, our findings provide the first demonstration that arousal regulation driven by central thalamus has a causal and frequency-dependent influence on zona incerta, and that suppressing the recruitment of zona incerta modulates the brain-wide dynamics driven by central thalamus stimulation. Specifically, our results suggest that the frequency-dependent depression of cortical activity is in part mediated by extrinsic inhibitory signals originating from zona incerta.

An additional mechanism that could contribute to the evoked suppression of cortex is feedforward thalamocortical inhibition - the process by which relay neurons drive inhibitory postsynaptic potentials (IPSPs) in pyramidal cells via fast spiking cortical interneurons [AC91, PJA01, CLC07]. Low-frequency (10 Hz) stimulations of certain thalamic nuclei *in vivo* yield strong hyperpolarization of cortical neurons putatively via this process [CC96a, CC96b]. It is also interesting to note that the "recruiting response," characterized by an enhanced cortical response during low frequency electrical stimulation of intralaminar nuclei [MD41], is hypothesized to originate from this inhibition [CC97]. Our observation that individual stimuli sometimes trigger spikes in cortex (Figure 2.8) is consistent with the possibility that these phenomena occur during the delivered 10 Hz optogenetic stimuli. However, intracellular and laminar recordings are needed to more conclusively resolve this issue. More recently, a study utilizing optogenetic targeting showed that non-specific "matrix" thalamocortical neurons preferentially drive inhibitory interneurons in cortical layer I [CAS12]. Moreover, they found that IPSPs generated by stimulation of matrix neurons (which constitute the nuclei targeted here [Jon01]) remain sustained during repeated stimuli compared to those evoked by stimulation of non-matrix neurons. Given the above findings, it is possible that interneuron-mediated thalamocortical inhibition, in addition to the demonstrated role of zona incerta, may contribute to the observed cortical responses. However, to the best of our knowledge, there have been no *in vivo* studies demonstrating that cortical interneuron-to-pyramidal cell inhibition is stronger at low frequencies of intralaminar thalamic stimulation compared to high frequencies.

In addition to providing novel insight into the mechanisms of arousal regulation by central thalamus, our study offers important insight into the cellular origins of the fMRI BOLD signal. While there is a growing body of evidence suggesting that negative BOLD signals reflect local decreases in neuronal activity [SAO06, PIF07, APD07, DTN07, ST07], the nature of this signal remains a subject of debate and holds significant potential for the interpretation of functional imaging studies [SKM08, Eks10]. It has been shown that different sensory stimuli can evoke positive and negative BOLD signals in the same cortical area, which are linked to increases and decreases in neural activity, respectively [SAO06]. Building upon these studies, we found that direct stimulation of central thalamus excitatory neurons at different frequencies leads to activa-

tion or suppression of neuronal activity in a downstream cortical location, which is coupled with positive and negative BOLD signals, respectively (Figure 2.7). These findings strongly support the hypothesis that a major component of the negative BOLD signal derives from decreases in neuronal activity and are consistent with previous reports of tight neural-hemodynamic coupling in the somatosensory cortex [HGP08].

Our results are also consistent with a previous study by Logothetis et al., which showed that low frequencies (<50 Hz) of electrical microstimulation in the thalamic lateral geniculate nucleus evoke negative BOLD responses in the monosynaptically connected V1 cortex, while higher frequencies (100-200 Hz) evoke positive BOLD responses in the same region [LAM10]. We observed similar results in the somatosensory cortex, which is monosynaptically connected to the stimulated intralaminar nuclei [WWG02] (Figure 2.3). The study by Logothetis et al. also found that cortical regions which are polysynaptically connected to the lateral geniculate nucleus, such as V2, even exhibit negative BOLD responses at high frequencies of stimulation (>60 Hz). It was proposed that these polysynaptic deactivations result from frequency-dependent disynaptic inhibition, the process by which pyramidal cells in cortex inhibit local and remote pyramidal cells via GABAergic interneurons. Unlike the study by Logothetis et al., we did not observe significant negative BOLD signals in either mono- or polysynaptically connected regions of cortex during high frequencies of stimulation. Furthermore, given the bias of corticocortical disynaptic inhibition toward higher frequencies [SM07], this microcircuit is unlikely to be driving the observed suppression of cortex during 10 Hz central thalamus stimulation.

In the context of electrical stimulation, our study helps dissociate the confounding effects of (a) delivering stimulation at a certain frequency (which can preferentially recruit certain neuronal elements [MG02]) and (b) the excited neuronal population firing at a specific frequency. With electrical stimulation, it has been impossible to dissociate these two effects *in vivo*, since the frequency of stimulation and preferential recruitment of specific neuronal populations could not be decoupled [MG02]. This made it difficult to explain, for example, the relationship between stimulation parameters and the therapeutic efficacy of deep brain stimulation. Using targeted, temporally precise, optogenetic stimulation in the current study allowed us to selectively excite

a single group of neuronal elements and identify their specific role in creating distinct modes of network function. The use of electrical stimulation instead would have prevented us from gaining this unique insight into the specific role of excitatory central thalamus neurons and their spiking frequency.

Finally, in the context of central thalamus DBS, our study offers important insight into the identification of proper stimulation targets and parameters that are needed before the therapeutic application of central thalamus stimulation can reach its full clinical potential. In particular, the images from ofMRI experiments (Figure 2.4 and Figure 2.6) reveal dramatic differences in global brain dynamics that can result from controlling one parameter of stimulation (i.e. frequency). Furthermore, the widespread activation of cortex and striatum observed at high frequencies of stimulation adds to a growing body of evidence that the central thalamus is a highly appropriate target for the remediation of acquired cognitive disabilities via forebrain recruitment. In a more general context that extends beyond stimulation of central thalamus, the ofMRI techniques we employ here are generalizable and can be universally applied to study the mechanisms under-lying DBS for other target regions and disorders. With this knowledge, stimulation paradigms can be optimized to accelerate clinical translation for a wide range of neurological disorders that currently lack such treatment, paving the way for the development of next-generation DBS therapies.

CHAPTER 3

Comparison of analysis methods for heterogeneous BOLD responses in ofMRI studies

This section is adapted from:

3.1 Introduction

Reliable detection of evoked BOLD responses is critical to estimate the brain activation maps in fMRI studies. In addition, there has been an increasing interest in characterizing temporal features such as onset and duration to investigate activation timing of BOLD responses across brain regions and experimental conditions [BLL15, HGD12, LLA09, LLW15, WFL15]. However, accurate detection and characterization remain challenging in scenarios where BOLD responses exhibit a large variability in the temporal dynamics [AZD98, GSH12, HOD04], such as in studies of disease states [AKS12, MHB06], and in small animal studies with anesthesia [SSR15, SSS14, WMM10], as in the case of Chapter 2. In these cases, commonly used GLM [FHW94] with a canonical hemodynamic response function (HRF) is often not the best choice. For example, in an fMRI study of motor control in human ischemic patients, GLM with a canonical HRF failed to detect motor cortex activation [AKS12]. It also failed to estimate temporal features of the BOLD responses [CSP04, LLA09]. In these studies, onset and duration differences between experimental conditions were misinterpreted as differences in the amplitudes of evoked BOLD responses. These substantial detection and characterization errors stress the importance of proper choice of analysis methods.

Nevertheless, it is currently not clear which methods are optimal in scenarios of heterogeneous BOLD responses. This is partially due to the large set of analysis approaches available, yet few comprehensive evaluations have been conducted, especially in block-design studies. Over the past decades, dozens of methods have been proposed. Among the most accessible ones are those implemented in widely available software packages, such as GLM with the canonical basis set [CSP04, FFJ98, HPR02, STR10], the gamma basis set, the Fourier basis set, the finite impulse response (FIR) basis set, and the B-spline basis set [Gen00]. Likewise, optimized methods for specific datasets have been considered. For example, colleagues have developed specific basis sets to estimate onset delays [LWP02], implemented transient plus sustained models to detect transient responses in block-design experiments [GLA00, HM02, SEH02], and designed basis sets that incorporate prior information of BOLD responses [WBS04]. Additionally, data-driven methods are employed as they place few assumptions on the hemody-

namic responses. Commonly used methods include independent component analysis (ICA) [BS04, EFS02, MJM98, MMB98], principal component analysis (PCA) [BBS96, SBB94], and fuzzy clustering analysis [BSS00, CCL99, WLD02].

In block-design studies, only data-driven methods, such as ICA, PCA, and unsupervised clustering, have been compared on their detection and characterization performance [BSS00, ERB11, MWL04], but not the more widely-used model-based approaches. In contrast, another study assessed several HRF models' ability to estimate HRF parameters from a block-design experiment, but did not examine detection performance [SWT14]. More often, comparisons were not conducted as the main purpose of the study, but to support the introduction of new approaches to analyze fMRI data [CAP01a, HM03, MMB98, MRM03], or to highlight the heterogeneity of the observed BOLD responses [AKS12, GSH12, PLO09, SSR15]. As a result, it is difficult to derive a comprehensive evaluation from the literature, due to the limited range of statistical methods employed and/or assessment conducted in each study.

Here, we investigate the robustness of six widely available methods against heterogeneous BOLD responses in block-design studies. Given the fact that the vast majority of methods already incorporate information about the shape of evoked hemodynamic responses during the detection stage, we focused not only on each method's detection performance, but also on their characterization power [DL14, MIV08]. A detailed comparison of state-of-the-art methods for analyses of heterogeneous BOLD responses is presented. Evaluations are carried out in the GLM framework and include standard basis sets as well as ICA. In order to evaluate each methods' performance against fMRI data with heterogeneous BOLD responses, we use data from the ofMRI study in Chapter 2 [LLW15]. To further validate each method's performance, we also use simulated data with varying temporal dynamics. Advantages and shortcomings of each approach are quantified using receiver operating characteristic (ROC) analysis and root-mean-square error (RMSE) of fit. Together, our results aim to provide practical recommendations on proper methods selection for analyzing block-design fMRI data with heterogeneous BOLD responses.

3.2 Materials and methods

3.2.1 fMRI analysis methods

In this study, a set of six different approaches including model-based and data-driven methods was evaluated (Figure 3.1). The same block-design paradigm was used across methods. It consisted of 30 s baseline, followed by six 60 s cycles, each consisting of 20 s stimulation and 40 s rest, unless otherwise noted. To enable comparison across methods, a single statistical analysis platform is needed. Therefore, the linear regression platform in Statistical Parametric Mapping (SPM, Wellcome Trust Center for Neuroimaging) was employed for statistical analysis. All methods were evaluated by using different sets of regressors within the same GLM framework. The detailed description of each method is included as follows:

(i) The canonical basis set was selected from the SPM toolbox as one of the most commonly used methods. Model orders up to 3 were included in the evaluation. In the present study, GLM with a single canonical HRF as basis function is referred to as the 1st order canonical basis set. GLM with a canonical HRF and its temporal derivative as basis functions is referred to as the 2nd order canonical basis set. GLM with a canonical HRF and its temporal and dispersion derivatives as basis functions is referred to as the 3rd order canonical basis set. The canonical basis functions were first convolved with the stimulation paradigm before being used as regressors for the canonical basis set.

(ii) The gamma basis set was selected from the SPM toolbox as another widely available method. Model orders up to 4 were investigated. Each order includes a set of K gamma functions of increasing dispersions as basis functions, where K denotes the model order. Similar with the canonical basis set, the gamma basis functions were first convolved with the stimulation paradigm before being used as regressors for the gamma basis set.

(iii) The FIR basis set was included as one of the most flexible basis sets. The model order of 3 to 10 was investigated. Each order includes a set of K contiguous boxcar functions, in which the bin width of each boxcar function equals T/K, where K denotes the model order, and T represents the length of each stimulation cycle (60 seconds). For simplicity, only results
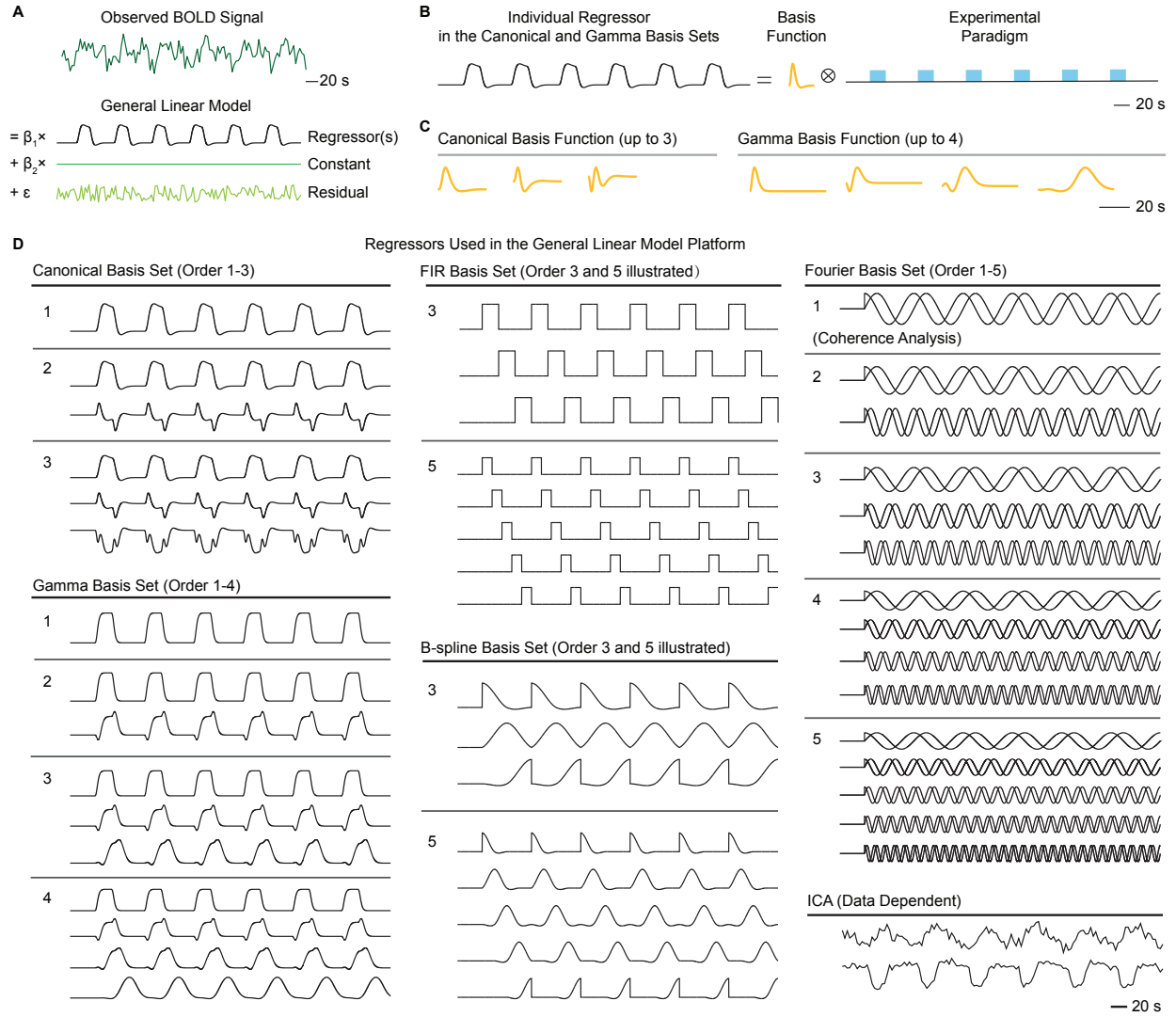
Figure 3.1: **A GLM platform was used to compare analysis methods.** *(A) Illustration of the general linear model framework. β_1 and β_2 are the coefficients in the model, and ϵ represents residual. (B) Each regressor used in the canonical and gamma basis sets is obtained by convolving a basis function with the experimental paradigm. Blue boxcars in the experimental paradigm represent the 20 s period of optical stimulation. (C) Illustration of the basis functions in the canonical and gamma basis sets. (D) Illustration of different sets of regressors used in the general linear model framework. Due to the space constraint, only order 3 and 5 are shown for the FIR and B-spline basis sets.*

from the odd numbers (e.g., model order of 3, 5, 7, and 9) are shown in figures. Additionally, we investigated the model order of 20, in which the bin width of each boxcar function equals our image acquisition interval (3 seconds), a common practice when employing the FIR basis set. Unlike the canonical and gamma basis sets, the FIR basis set was not convolved with the stimulation paradigm before being used as regressors.

(iv) The B-spline basis set was selected as another popular analysis method [Gen00, SSR15]. The model order of 3 to 10 was included in the evaluation. Each order includes a set of K cubic spline functions created using the program 3dDeconvolve in the AFNI software package [Cox96, War02], where K denotes the model order. Similar with the FIR basis set, only results from the odd numbers are shown for simplicity (e.g., model order of 3, 5, 7, and 9), and the B-spline basis set was not convolved with the stimulation paradigm before being used as regressors.

(v) The Fourier basis set was selected due to its capability to exploit the periodic nature of the experimental paradigm and evoked responses [BBW96, PJS16]. Model orders up to 5 were investigated. Each order includes a set of K sine and K cosine functions at harmonic frequencies: f_1, 2 f_1, ..., K f_1 Hz, where K denotes the model order, and f_1 represents the frequency of repeated stimulation cycles (1/60 Hz). Similar with the FIR and B-spline basis sets, the Fourier basis set was not convolved with the stimulation paradigm before being used as regressors.

It is worth noting that, GLM with the 1st order Fourier basis set is mathematically equivalent with coherence analysis, a frequency-domain analysis method that is widely used in periodic block-design studies [AKS12, BJW93, EGW97, LDG10], including the ofMRI datasets in Chapter 2 that we utilized in this chapter [LLW15]. A coherence value was defined as a ratio of the magnitude of each time series' Fourier transform (F) at the frequency of repeated stimulation cycles (f_1, 1/60 Hz) and the total energy of all frequency components:

$$coherence = \frac{|F(f_1)|}{\sqrt{\sum_f |F(f)|^2}} \tag{3.1}$$

According to [EGW97], the coherence value is equivalent to the Pearson's correlation coefficient of the target time series with the best fitted sinusoid waveform at f_1 in the least-squares sense. Therefore, coherence analysis is equivalent to GLM with the 1st order Fourier basis set, according

to:

$$\beta_0 \cdot sin(2\pi f_1 t + \theta) = \beta_1 \cdot sin(2\pi f_1 t) + \beta_2 \cdot cos(2\pi f_1 t) \tag{3.2}$$

when $\beta_1 = \beta_0 \cdot cos(\theta)$ and $\beta_2 = \beta_0 \cdot sin(\theta)$. In Eq. (3.2), β_1 and β_2 are the coefficients of the model, t denotes time, and θ represents the phase shift of the best fitted sinusoidal waveform.

(vi) Spatial ICA was chosen as one of the most commonly used data-driven approaches. GIFT ICA algorithm [CAP01a] with the Infomax approach [BS95] was used to extract the spatially independent components. Since there has been no consensus on the optimal method for estimating the number of independent components, the default setting in the GIFT software package (20 components) was used. After ICA decomposition, the independent components representing the signal of interest, which we refer to as signal components, were selected. In the present study, we assumed that their time courses share similar periodicity as the stimulation paradigm. Selection was achieved using the following two steps.

First, we ranked all components' associated time courses based on their power spectrum. In the study by [MRM03], the frequency power spectrum of each independent component time courses were ranked by their magnitude contributions at the frequency of repeated stimulation cycles. Here, we quantified this ranking by calculating the coherence value for the time series of each component. In addition, we incorporated the time series' Fourier transform magnitude at the second harmonic (f_2, 1/30 Hz) to maximize the separation between signal and noise components [NHT09]. Here we refer to the modified coherence value as coherence$_m$:

$$coherence_m = \frac{\sqrt{|F(f_1)|^2 + |F(f_2)|^2}}{\sqrt{\sum_f |F(f)|^2}} \tag{3.3}$$

Then, we used hierarchical agglomerative clustering [Joh67] to separate the extracted components into two groups: one group with signal components and the other group with noise components. Here, we assumed that the signal components exhibited distinctly higher coherence$_m$ values than the noise components. Therefore, if we separated the extracted signal components into two groups based on their coherence$_m$ values, the cluster with higher coherence$_m$ values should predominately contain signal components, while the other cluster with lower coherence$_m$ values

should primarily contain noise components. Based on these assumptions, we used hierarchical agglomerative clustering to group the obtained coherence$_m$ values into a hierarchical cluster tree, as shown in the dendrogram in Figure 3.2. We then cut the hierarchical tree to yield two clusters that have the largest inter-cluster distance. The cluster with higher coherence$_m$ values was used as the group with signal components (Figure 3.2). The time series of all the signal components were employed as a set of regressors, resembling a unified GLM-ICA approach [HYL05, PLO09].

The above separation was conducted without a predefined number of signal components and was solely based on each component's coherence$_m$ value. In other words, the number of signal components was determined by the inherent structure of the data, thus avoiding biasing the results by using fixed numbers of signal components. We also did not use a predefined coherence$_m$ threshold during the separation, as such threshold may only be selected in an arbitrary fashion.

3.2.2 Performance metrics

We evaluated the aforementioned methods based on their detection and characterization performance. For the ofMRI data, since the ground truth is unknown, detection volume and modified ROC curves [NC03] were used as detection metrics. The modified ROC curve was created by plotting the fraction of detected voxels in each subject with ChR2-containing virus injection (experimental group) against the fraction of detected voxels averaged across subjects with saline injection (control group) at varying thresholds. The fraction was calculated as a ratio of the number of detected voxels and the number of brain-masked voxels in each dataset. To quantify the modified ROC curve, area under the ROC curve (AUC) was calculated using a small fraction of the modified ROC curve (fraction of control positive < 0.05) instead of the entire curve, since this region is more relevant for fMRI analysis [NC03]. For the simulated data, where the ground truth is known, we used true positive rate (TPR), false positive rate (FPR), and AUC as detection metrics. TPR was defined as the percentage of ground truth positive voxels that were correctly detected as activated. FPR was defined as the percentage of simulated noise voxels that were incorrectly detected as activated. ROC was used to characterize TPR and FPR at varying thresholds [SCG99]. As before, AUC was calculated using a small fraction of the ROC curve (FPR < 0.05)
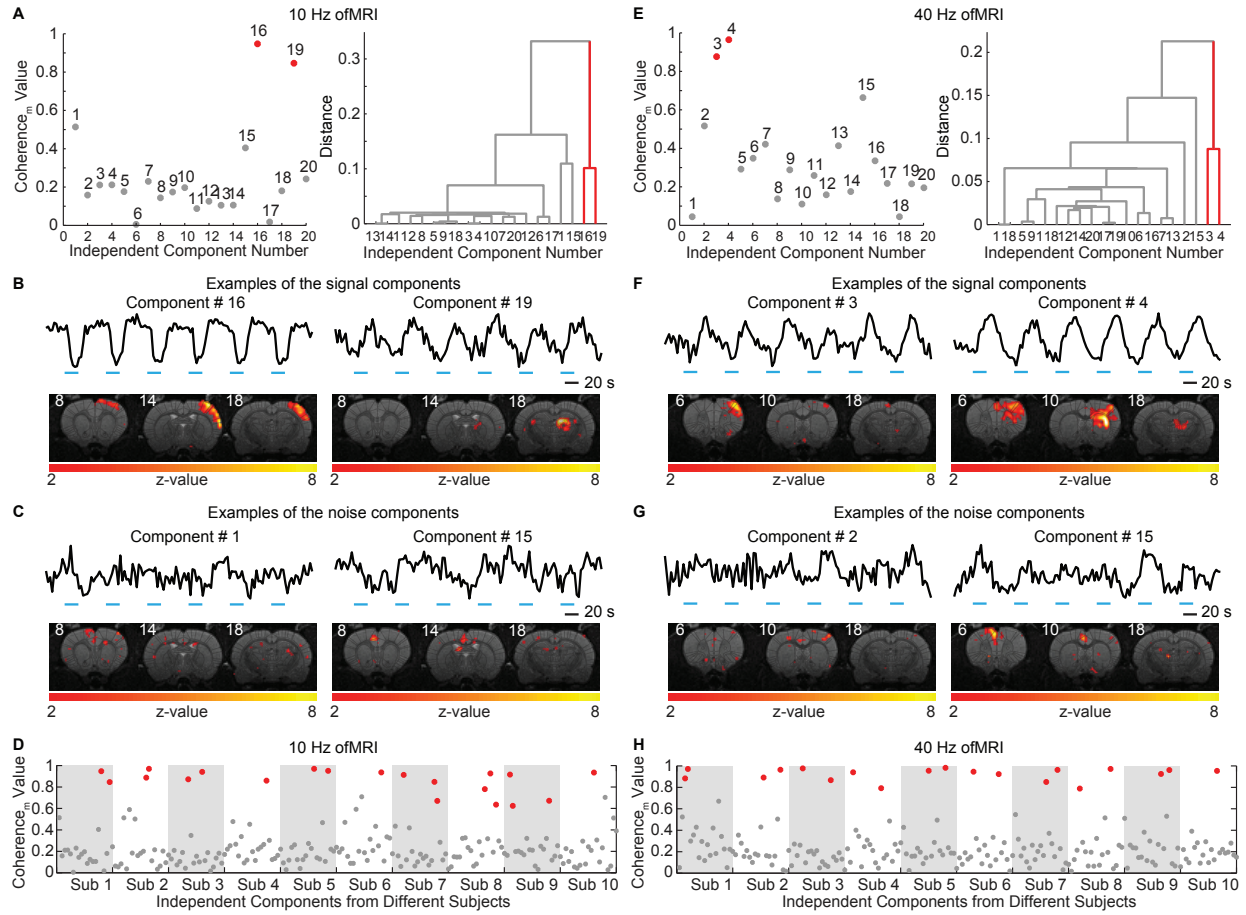
Figure 3.2: **Coherence_m value was used to select the signal components with the experimental ofMRI datasets.** *Examples with the experimental ofMRI data from Chapter 2 are shown here. (A, E) Scatter plots show coherence_m value (left panel) and dendrogram (right panel) of each extracted independent component from a representative subject in the experimental group. The signal components (red) have substantially higher coherence_m values than the noise components (gray) with the 10 Hz and 40 Hz stimulation ofMRI datasets. Dendrogram was generated using the hierarchical agglomerative clustering method. The number of independent components in each subject was set to 20, which is the default setting for the ICA software used in the present study. (B, F) The time courses and the spatial maps associated with the signal components are shown. Threshold was set at $|Z| > 2$ for the spatial map and horizontal blue bars represent the 20 s period of optical stimulation in panel B, C, F, and G. (C, G) The time courses and the spatial maps associated with the noise components are shown. Here we show two noise components that exhibit the highest coherence_m values in the noise group. Unlike the signal components, the time courses of the noise components do not share similar periodicity as the stimulation paradigm. (D, H) Coherence_m value was used to select signal components for each subject separately. With both the 10 Hz and 40 Hz stimulation ofMRI datasets, the selected signal components (red) have distinctively higher coherence_m values than the noise components (gray) within each subject. Subject 1 is the representative subject result shown in panel A, B, C, E, F, and G. Non-smoothed ofMRI data are used in each panel.*

58

instead of the entire curve.

The characterization performance metrics included temporal parameter estimation accuracy and RMSE of fit. Two standard parameters, onset and duration, were used for temporal parameter estimation. Onset was defined as the time to half-peak [HFP03, WSB01], and duration was defined as full-width at half-peak [LLA09]. These parameters were used to characterize time series without assuming any specific shape. The estimated value was calculated from a single period. For the model-based methods, the temporal structure of the fitted time series is the same over each stimulation cycle. However, it is not the case for ICA, therefore we averaged fitted time series across cycles and estimated values from the averaged period. With the ofMRI data, since the ground truth is not available, we calculated the temporal parameter estimation error as the difference between the estimated value and the value measured from the observed time course. As before, since the temporal structure of the observed time series is not the same over each stimulation cycle, we averaged the observed time series across cycles and measured onset and duration from the averaged period. With the simulated data, since the ground truth is available, we calculated the temporal parameter estimation error as the difference between the estimated value and the ground truth. In addition to the temporal parameter estimation, RMSE of fit was used to evaluate each method's capability to estimate the time course of the BOLD responses for the ofMRI and simulated data:

$$RMSE = \sqrt{\frac{\sum_{i=1}^{n}(y_i - \hat{y}_i)^2}{n}} \qquad (3.4)$$

where $\hat{y}_i$ is the fitted data and n is the number of time points. With the ofMRI data, since the ground truth is not available, we used observed data for y_i. For the simulated data, we used the ground truth signal for y_i instead.

As described above, AUC and RMSE were calculated differently for the ofMRI datasets and the simulated datasets. Specifically, for the ofMRI datasets, AUC was calculated using the modified ROC curve that plots the fractions of detected voxels with the experimental group against those with the control group, while for the simulated datasets, AUC was calculated using the ROC curve that plots TPR against FPR. Similarly, RMSE was calculated relative to the observed

data for the ofMRI datasets, but was calculated relative to the ground truth for the simulated datasets. With such differences, the values of the corresponding performance metrics can be very different in the ofMRI datasets and the simulated datasets, especially for AUC, where up to one order of magnitude difference was observed (Table 3.1). Therefore, to enable a direct comparison between the performance of each method across ofMRI and simulated datasets, we standardized the AUC and RMSE values according to the following formulas:

$$Standardized\ AUC_{i} = \frac{AUC_{i} - AUC_{second\ lowest}}{AUC_{second\ highest} - AUC_{second\ lowest}} \tag{3.5}$$

$$Standardized\ RMSE_{i} = \frac{RMSE_{i} - RMSE_{second\ lowest}}{RMSE_{second\ highest} - RMSE_{second\ lowest}} \tag{3.6}$$

To eliminate the influence of extreme values, the second highest value and the second lowest value were used in the above formulas. In this case, the method with the second highest AUC or RMSE was assigned a value of 1, while the method with the second lowest AUC or RMSE was assigned a value of 0. The method with the highest AUC or RMSE was assigned a value of larger than 1, while the method with the lowest AUC or RMSE was assigned a negative value.

3.2.3 Image analysis

For the ofMRI datasets, custom written software in MATLAB (MathWorks, Inc.) was used for image reconstruction, motion correction [FL13], and registration. The acquired 4D fMRI images were manually registered to a common space using a six degree-of-freedom rigid body transformation. Low-frequency drift was removed by temporal high pass filtering with a cut-off frequency of 1/128 Hz as implemented in SPM. 5 or 6 ofMRI acquisitions were collected for each subject. After preprocessing, the 4D fMRI images for each subject were normalized to the same scale to account for differences in mean and variance. All the ofMRI acquisitions were then averaged for each subject before statistical analysis. Both single-subject and group-level analyses were conducted during statistical analysis.

For the single-subject analysis, we show results that either do not involve smoothing in the

preprocessing step to preserve the distinct hemodynamic responses and enable comparisons at the single-voxel level [DDA97, GK09], or involve spatial smoothing with a 0.5 mm FWHM Gaussian kernel to increase the signal-to-noise ratio. Throughout the present study, results with the single-subject analysis refer to those that do not involve smoothing in the preprocessing step, unless otherwise noted. Prior to statistical analysis, the correlations within each set of regressors were removed using the SPM implementation of Gram-Schmidt orthogonalization. After generating statistical parametric maps using the linear regression platform in SPM, a threshold was applied to define activated voxels. Commonly used voxel-wise threshold settings were employed. For the non-smoothed data, we applied $p < 0.05$ with Bonferroni correction to control the family-wise error rate (FWER), uncorrected $p < 0.001$, and false discovery rate (FDR) < 0.05 [BH95, GLN02] on all brain-masked voxels. For the spatially-smoothed data, we used $p < 0.05$ with random field theory correction to control the FWER on all brain-masked voxels. Note that here we used voxel-wise inference instead of cluster-wise inference during statistical analysis. This is because with our imaging acquisition parameters, SPM's cluster-wise inferences may yield inflated false positive rate at the first-level analysis [EAJ12].

For the group-level analysis, fixed-effects analysis and random-effects analysis were conducted using SPM to show the detected activation maps at the group level. Experimental ofMRI data from 10 subjects were included. We applied a 0.5 mm FWHM Gaussian kernel to spatially smooth the raw data in order to increase the signal-to-noise ratio and ameliorate differences in the inter-subject localization. With the fixed-effects analysis, the time series from each subject were temporally concatenated across different subjects before entering into a first-level analysis using SPM. With the random-effects analysis, regression coefficient estimates from the single-subject analysis for each subject were entered into a second-level analysis, and a full factorial design was used for each method and model order at the second level analysis. The potentially unequal variance of the regression residuals across subjects was accounted for by using the correction algorithm implemented in SPM. With both the fixed-effects and random-effects analyses, because the data was spatially smoothed,the statistical threshold was set to $p < 0.05$ with random field theory correction to control the FWER [WEM92]. Similar to the single-subject analysis, here we used voxel-wise inference, as SPM's cluster-wise inference may yield inflated false-positive rates

at the group level [ENK16].

Since the group-level analysis requires each method to share the same regressors across different subjects, group ICA was conducted to select a common set of signal components among different subjects. Group ICA was performed based on the self-organizing clustering method [ESH05]. In short, 20 independent components were extracted for each subject using GIFT software package. For a total of 10 subjects in each group, 200 independent components were extracted. Then, a similarity matrix (SM) value was calculated for each pair of the 200 total independent components, resulting in a 200×200 matrix. Each value in the similarity matrix was calculated using a weighted sum of the correlation coefficients of each component pair's spatial component maps (CC_s) and their associated time courses (CC_t):

$$SM(i,j) = \lambda \cdot CC_s(i,j) + (1 - \lambda) \cdot CC_t(i,j) \tag{3.7}$$

In Eq. (3.7), i and j each represent an independent component. λ was set to 0.5, so that the spatial and temporal correlations were equally weighted. The similarity matrix was then converted into a dissimilarity matrix (DM) according to:

$$DM(i,j) = \sqrt{1 - SM(i,j)} \tag{3.8}$$

Based on the resulting DM matrix, we invoked a supervised hierarchical clustering algorithm, which links components to each other only if they were from different subjects. In this way, similar components in different subjects were clustered into the same group, yielding a total of 20 groups, where each group contains 10 components, and each component originated from a different subject. The mean time courses from each group were ranked based on their coherence$_\text{m}$ values, and signal groups were selected using hierarchical agglomerative clustering as described earlier. The mean time series from each of the signal groups were employed as a set of regressors for the fixed-effects and random-effects analyses.

For the simulated datasets, the analysis was conducted similarly to the single-subject analysis for the ofMRI datasets as described earlier. Due to the space limit and scope of the present

work, spatial smoothing was not involved in the preprocessing step and group-level analyses were not conducted with the simulated data. As before, prior to statistical analysis, the correlations within each set of regressors were removed using the SPM implementation of Gram-Schmidt orthogonalization. The statistical parametric maps were generated using the linear regression platform implemented in SPM. Commonly used voxel-wise threshold settings were employed to define activated voxels, which include $p < 0.05$ with Bonferroni correction to control the FWER, uncorrected $p < 0.001$, and FDR < 0.05 [BH95, GLN02] on all brain-masked voxels.

3.2.4 ofMRI data

As mentioned above, we used data from the *in vivo* ofMRI study in Chapter 2 to evaluate the analysis methods. The high level of variability in the evoked BOLD responses offers an excellent opportunity to assess the robustness of different methods to cope with heterogeneous BOLD responses.

In the present study, three groups of subjects were included in the ofMRI datasets. (i-ii) The first two groups of subjects are the experimental groups. In these subjects, adeno associated viruses that were engineered to express channelrhodopsin-2 (ChR2) were stereotaxically injected into the central thalamus of each subject. A fiber optic cannula was subsequently implanted for light delivery. (i) In the first experimental group, data from 10 subjects with 10 Hz or 40 Hz optical stimulation in the central thalamus was used. The stimulation paradigm consisted of 30 s baseline, followed by six 60 s cycles, each consisting of 20 s stimulation and 40 s rest. Throughout the present study, the experimental ofMRI data refer to data from the first experimental group, unless otherwise noted. (ii) In the second experimental group, data from one subject with 100 Hz optical stimulation in the central thalamus was used. Here we employed a slightly different stimulation paradigm compared to the first experimental group, in which 10 s of stimulation was applied in each of the six cycles instead of 20 s (Figure 3.13A). (iii) The third group of subjects is the control group. In this case, saline was injected into the central thalamus of each subject and a fiber optic cannula was implanted for light delivery. Data from two subjects with 40 Hz optical stimulation in the central thalamus was used. The stimulation paradigm was the same as in the

first experimental group.

3.2.5 Simulated data

Simulated datasets were generated to utilize data with known ground truth (Figure 3.3). We assumed that a diverse range of signal shapes was evoked using the same six-cycle block design as in the experimental ofMRI data. Each simulated slice was based on a single imaging slice from the experimental ofMRI data during the baseline period. Random, non-physiological system disturbances were modeled by additive Gaussian noise and were added into all the brain-masked voxels. In each slice, signals with the same shape were added into two "active" regions in the cortex and striatum. The activation signal was created by convolving the canonical HRF used in SPM with a boxcar function with a varying onset and duration. The onset shift of the boxcar function was set to vary between 0 and 20 s, time locked to the 20 s stimulation block. The duration range was set to vary between 5 and 50 s, to reflect the transient and prolonged BOLD responses observed in previous studies [DCC15, GSH12, WFL15]. After convolving each boxcar function with the canonical HRF used in SPM, the resulting time series that did not return to below 50 % maximum amplitude at the end of each cycle were excluded, resulting in 85 shapes, each with a distinct onset and duration. To ensure the generalizability of the results, three different contrast-to-noise ratios (CNR), 1, 1.5, and 2, were used. CNR was calculated as a ratio of the signal amplitude and the standard deviation of the underlying noise in the time domain.

For each method, we summarized the analysis results that were obtained from the simulated datasets with different signal shapes. This was conducted by averaging the analysis results across all signal shapes assuming a uniform distribution, or by calculating weighted average based on the bivariate probability distribution of onset and duration for the 10 Hz and 40 Hz stimulation ofMRI data. The probability distribution was estimated using the onset and duration measured from the observed raw time series in the ofMRI datasets. The superset of voxels detected by each method across all subjects were included. The threshold was set to $p < 0.05$ with Bonferroni correction. To minimize the effect of outliers, the onset and duration range between the 5th and 95th percentile was included. Based on these onset and duration values, a histogram approach was
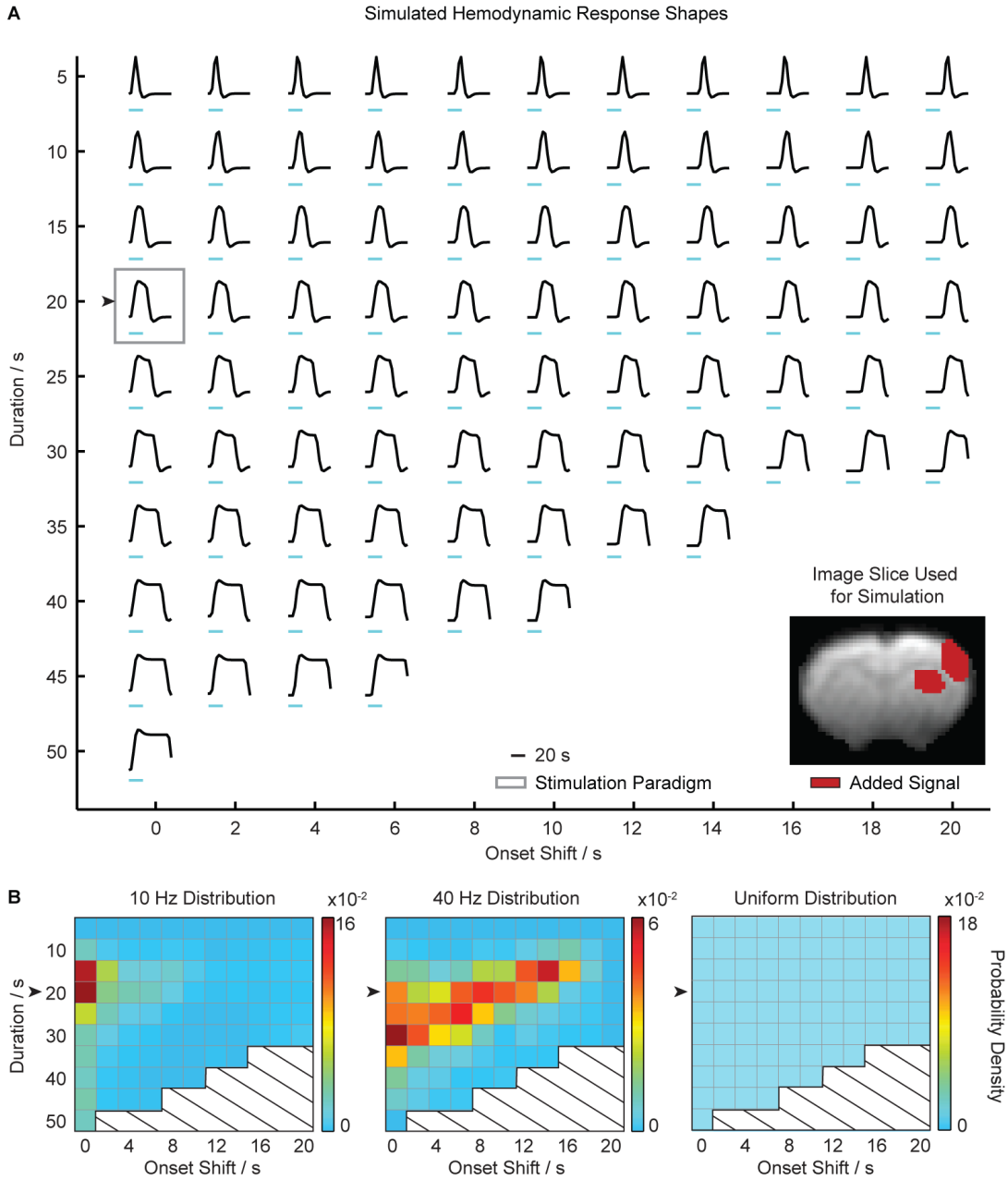
Figure 3.3: **Simulated datasets were designed to have a wide range of onset and duration.** *(A) Signals were simulated with varying onset and duration. The simulated shape that matches the canonical response is denoted by a black arrowhead in each panel. The horizontal axis refers to the onset shift of each signal shape relative to the canonical response. The vertical axis refers to the duration of each signal shape. Bottom right shows the spatial activation pattern of the simulated data with the ground truth positive voxels overlaid in red. (B) Three probability distributions of onset and duration are shown. Each square in the grid corresponds to the probability of the onset and duration from a different simulated signal shape.*

used to estimate the probability distributions. Specifically, we generated a 2D histogram using the following steps. First, we divided the onset and duration values from the ofMRI data into a series of consecutive and non-overlapping bins. The bins were specified based on the onset and duration of each simulated signal shape. Then, we counted how many values fell into each bin. The ratio of the number of values in each bin and the total number of values across all bins was obtained as the probability for the corresponding simulated signal shape.

Concerning ICA, before computing the summary statistics, we defined a set of specific regressors for each distribution of onset and duration. This was different from model-based methods, where the set of regressors was pre-determined. In ICA, to obtain the distribution-specific regressors, additional datasets were generated to depict different distributions. For example, we used spatial concatenation of simulated datasets with different signal shapes to generate the uniform distribution. In this case, each signal shape was present in the same number of active voxels. Conversely, to simulate the 10 Hz and 40 Hz stimulation ofMRI data, we generated datasets with the same data size and "active" regions as those for the uniform distribution; however, unlike the uniform distribution, here each signal shape was present in a different number of active voxels. In particular, the number of active voxels that contained each signal shape was calculated as the product of the total number of active voxels in the datasets and the probability of the signal shape in the 10 Hz or 40 Hz stimulation ofMRI data distribution. As a result, three datasets were generated, each of them depicting a different distribution of onset and duration. In each dataset, we extracted independent components using the GIFT software package. We then selected signal components using coherence$_m$ value plus hierarchical agglomerative clustering, as described earlier in the manuscript. Finally, the signal components were used as a set of distribution-specific regressors. From here, the next steps of the statistical analysis were set to be the same for ICA as for model-based methods with the goal of fairly compare the performance across different methods.

3.3 Results

3.3.1 Conventionally used analysis method leads to detection and characterization errors with ofMRI datasets

Figure 3.4 shows the detection and characterization results by GLM with the 1st order canonical basis set using the experimental ofMRI data in Chapter 2. Based on previous anatomical and electrophysiological studies, where widespread projections from the stimulation site (i.e., the central thalamus) to the forebrain have been demonstrated [DBP96, SG82, WWG02], we would expect a large volume of forebrain activities to be detected with the ofMRI data. However, the 1st order canonical basis set detects cortical and thalamic responses with the 10 Hz stimulation ofMRI data, but detects a small volume of responses with the 40 Hz stimulation ofMRI data, in contrast to what was detected using coherence analysis in Chapter 2. We then take a close look at the observed BOLD responses detected by the 1st order canonical basis set. There, we see variations in their temporal dynamics across different stimulation frequencies (Figure 3.4E-H) and brain regions (Figure 3.6A, B). Specifically, at 10 Hz stimulation, the observed BOLD responses (Figure 3.4E, G), especially those in the cortex (Figure 3.6A), show similar onset and duration as theconvolution of the canonical HRF with the experimental paradigm, which henceforth we refer to as canonical response. While at 40 Hz stimulation, the observed BOLD responses show delayed onset and extended duration compared to the canonical response (Figure 3.4F, H), especially in the thalamus and striatum (Figure 3.6B). However, the 1st order canonical basis set is not able to characterize these diverse temporal features in the ofMRI data (Figure 3.4I-L), as its shape is fixed and only its amplitude is allowed to vary [WF95].

The above results obtained by the 1st order canonical basis set demonstrate its inability to cope with highly variable responses. Here, we sought to understand the proper choice of methods in these scenarios. Specifically, we conducted a systematic evaluation to assess a set of six standard methods' capabilities to detect and characterize heterogeneous BOLD responses. These include GLM with the canonical, gamma, FIR, B-spline, and Fourier basis sets, as well as ICA (Figure 3.1).
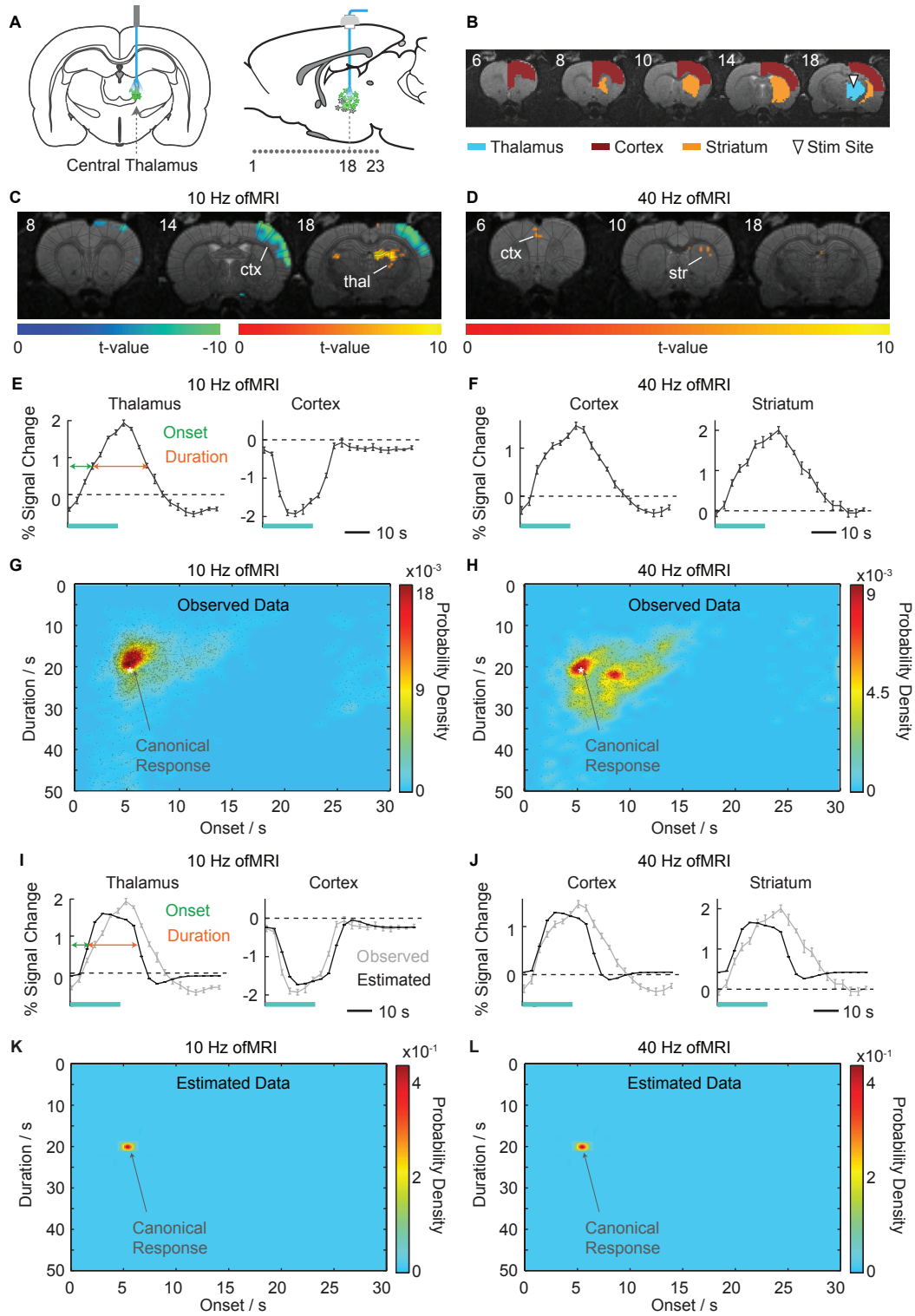
Figure 3.4: **GLM with 1st order canonical basis set leads to detection and characterization errors with experimental ofMRI datasets.**

Figure 3.4: *(A) Schematic of the ofMRI experimental design indicating the site of transduced cells in the central thalamus (green), optical fiber location (blue line), and location of acquired coronal fMRI slices (1...23). Slice numbers correspond to those denoted in the activation maps in subsequent figures. (B) Regions of interest used to extract the time series in subsequent figures are shown. (C, D) Activation maps detected by GLM with the 1st order canonical basis set from a representative subject are shown. For group-level activation maps, please see Figure 3.9 and Figure 3.10. In panel C-L, non-smoothed ofMRI data were used and the threshold was set to p < 0.05 with Bonferroni correction. T2-weighted anatomical images are used as underlays. (E, F) Plots showing the observed BOLD responses that are detected by GLM with the 1st order canonical basis set. They were generated by first averaging the time series of detected voxels that fell within each region of interest, followed by averaging over six stimulation cycles of the resulting time series. Error bars represent standard error of the mean (SEM) across different stimulation cycles. The superset of voxels detected by GLM with the 1st order canonical basis set in each subject were used in panel E-L (N = 10 subjects). Percent signal change was calculated relative to the baseline period. Horizontal blue bars represent the 20 s period of optical stimulation. (G, H) Plots showing the onset and duration measured from the observed data. Each grey dot refers to a detected voxel from a subject (N = 10 subjects). Probability density color map was calculated with a histogram of 50 bins along each axis. Canonical response was generated by convolving the canonical HRF with the experimental paradigm. (I, J) Plots showing the fitted BOLD responses that are estimated by GLM with the 1st order canonical basis set. The observed responses shown in panel E and F are overlaid here for comparison using gray line. (K, L) Plots showing the onset and duration estimated by GLM with the 1st order canonical basis set. Abbreviations are as follows: ctx (cortex), str (striatum), and thal (thalamus).*

3.3.2 Detection capability assessment with ofMRI datasets

GLM with the 2nd and 3rd order canonical basis sets, the 2nd to 4th order gamma basis sets, the 5th to 20th order FIR basis sets, the 5th to 9th order B-spline basis sets, and the 2nd to 5th order Fourier basis sets show good detection performance with the ofMRI datasets

We first examined the detection performance across different methods with the experimental ofMRI data. With the 10 Hz stimulation data, the 2nd and 3rd order canonical basis sets, the 1st to 4th order gamma basis sets, the 5th to 7th order B-spline basis sets, the 2nd order Fourier basis set, and ICA detect significantly greater volumes compared to the 1st order canonical basis set (Figure 3.5A). Among the different methods, ICA detects the largest volume. Nonetheless, each method detects similar activations at the stimulation site (i.e., the thalamus) and the downstream brain regions (Figure 3.5B). The observed BOLD responses detected by different methods also share similar onset and duration as the canonical response (Figure 3.5C, D), especially in the
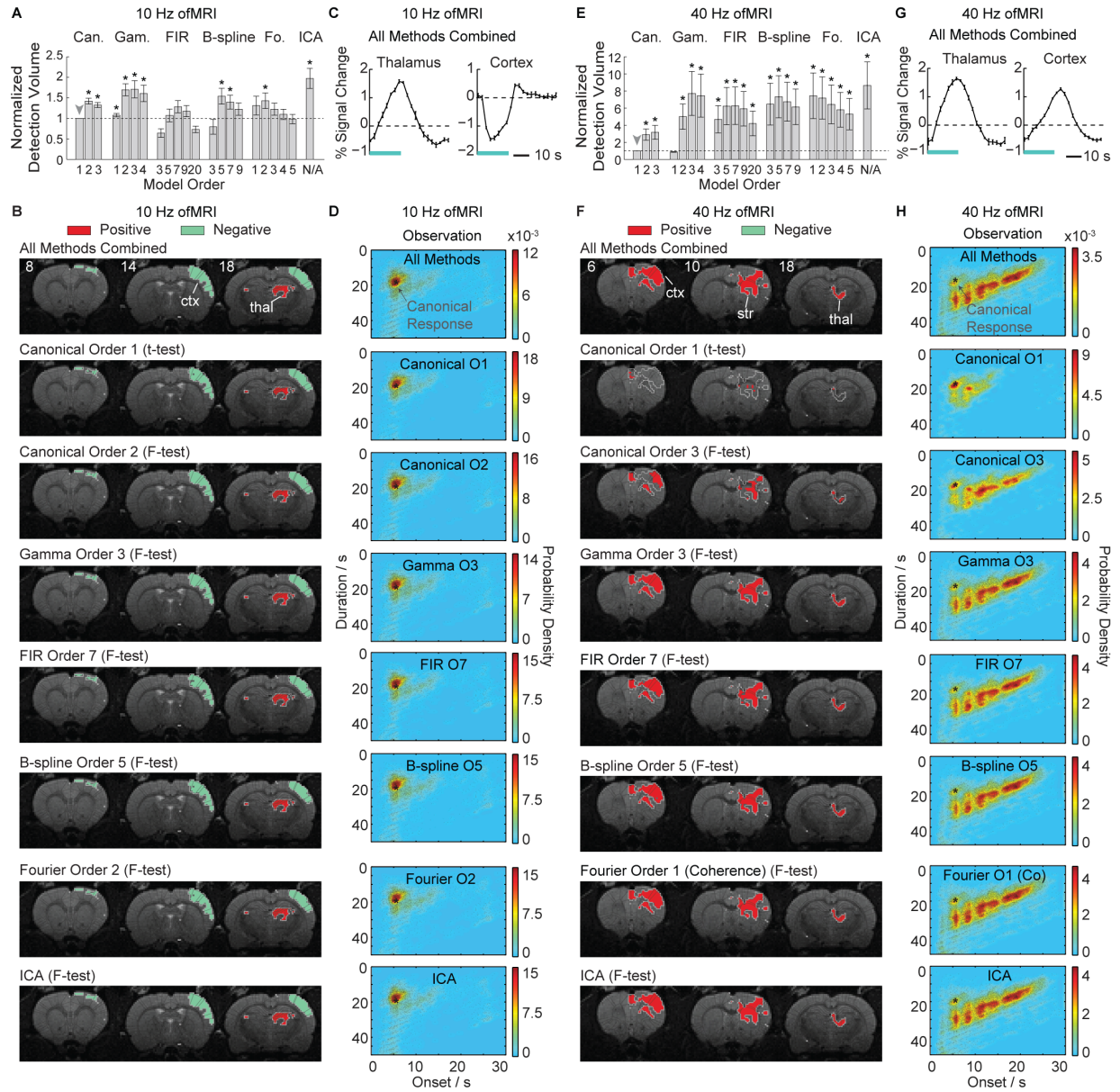
Figure 3.5: **GLM with the 2nd and 3rd order canonical basis sets, the 2nd to 4th order gamma basis sets, the 5th to 7th order B-spline basis sets, the 2nd order Fourier basis set, and ICA yield large detection volumes with the experimental ofMRI datasets.** *(A-D) Detection capability assessment with the 10 Hz stimulation ofMRI data. (E-H) Detection capability assessment with the 40 Hz stimulation ofMRI data. (A, E) Bar graphs show the active volume detected by each method. The detection volume was first normalized to the active volume detected by GLM with the 1st order canonical basis set (gray arrowhead and dashed horizontal line) for each subject, and then averaged across different subjects. Non-smoothed ofMRI data were used and the threshold was set to $p < 0.05$ with Bonferroni correction in each panel. Error bars represent SEM across different subjects. Asterisk indicates $p < 0.05$ compared with GLM with the 1st order canonical basis set using one-sided Wilcoxon signed-rank test (N = 10 subjects).*

70

Figure 3.5: *(B, F) Activation maps from a representative subject are shown. For group-level activation maps, please see Figure 3.9 and Figure 3.10. Here, for simplicity, we show results from conventionally used GLM with the 1st order canonical basis set, as well as from the model order within each method that yields the largest detection volume in panel A and E. The gray border represents the superset of voxels that are detected by all tested methods.Colored voxels are detected by the method denoted in the figure legend. The evoked response is considered positive if the average percent signal change over entire stimulation cycle is above zero, otherwise is considered negative. T2-weighted anatomical images are used as underlays. (C, G) Plots show the observed BOLD responses that are detected by all methods combined. Error bars represent SEM across different stimulation cycles. Horizontal blue bars represent the 20 s period of optical stimulation. (D, H) Plots show the onset and duration measured from the BOLD responses that are detected by each method. The onset and duration are measured from the observed time course, not estimated from the fitted time course. Each grey dot refers to a detected voxel from a subject (N = 10 subjects). The probability density color map is overlaid. Note that, the plots for the 1st order canonical basis set are identical to those in Figure 3.4G and H. Abbreviations are as follows: Can. (canonical), Gam. (gamma), Fo. (Fourier), ctx (cortex), str (striatum), thal (thalamus), and co (coherence analysis).*

cortex (Figure 3.6C). In contrast, with the 40 Hz stimulation data, the majority of the methods yield significantly larger volumes compared to the 1st order canonical basis set, including the 2nd and 3rd order canonical basis sets, the 2nd to 4th order gamma basis sets, the 3rd to 20th order FIR basis sets, the 3rd to 9th order B-spline basis sets, the 1st to 5th order Fourier basis sets, and ICA (Figure 3.5E). Among the different methods, ICA detects the largest volume. Unlike the detection results with the 10 Hz stimulation ofMRI data, not all methods are able to detect responses at the stimulation site and the downstream brain regions during 40 Hz stimulation (Figure 3.5F). Specifically, the 1st order canonical basis set detects a very small volume in the thalamus, cortex, and striatum, while most of the other methods detect a large volume in these regions. In addition, with 40 Hz stimulation, the observed BOLD responses, especially those in the cortex, show much higher variations in their temporal dynamics compared to the 10 Hz stimulation ofMRI datasets (Figure 3.5G, H, Figure 3.6D). Most of the methods are able to detect BOLD responses with substantial onset and duration deviations from the canonical response, except for the 1st order canonical basis set (Figure 3.5H).

Next, we examined the consistency of these detection results across different conditions. There, detection results with similar trends within and across methods are obtained when: (i)
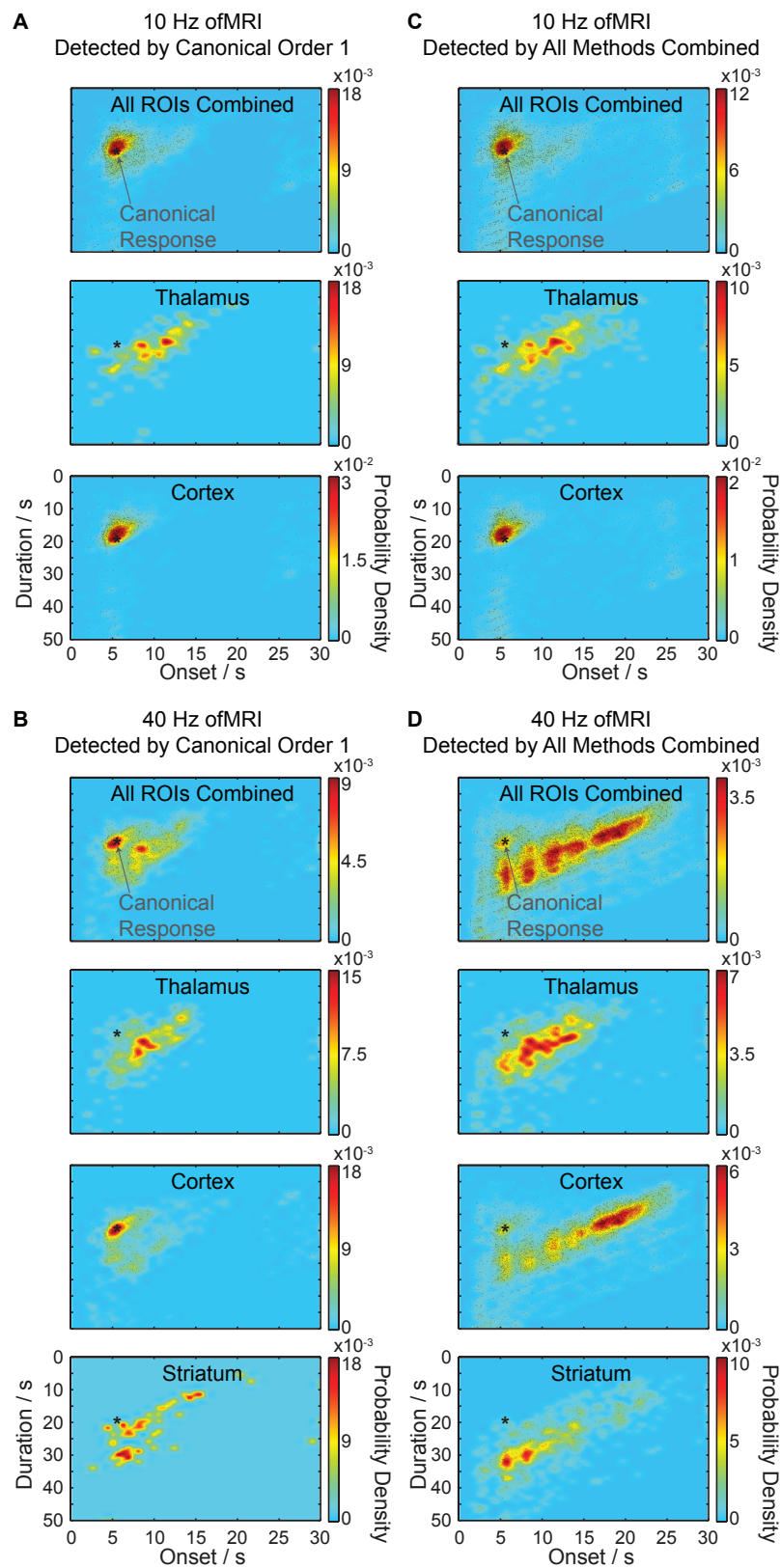
Figure 3.6

Figure 3.6: ***Observed BOLD responses exhibit distinct temporal characteristics in different brain regions in the experimental ofMRI datasets.*** *With the 10 Hz stimulation ofMRI data, there are few differences between the observed responses detected by the 1st order canonical basis set (panel A) and those detected by all methods combined (panel C). In both cases, the cortex exhibits onset and duration values that closely resemble the canonical response, while those in the thalamus show deviations from the canonical response. With the 40 Hz stimulation ofMRI data, there are clear differences between the observed responses detected by the 1st order canonical basis set and those detected by all methods combined. The differences are especially prominent in the cortex. There, the observed responses detected by the 1st order canonical basis set are similar to the canonical response (panel B), while those detected by all methods combined mostly show delayed onset and extended duration from the canonical response (panel D). (A-D) Plots show the onset and duration measured from the observed BOLD responses. The onset and duration values from detected voxels that fell within each region of interest are shown. The regions of interest are shown in Figure 3.4B. The superset of voxels detected by GLM with the 1st order canonical basis set in each subject were used in panel A and B. The superset of voxels detected by all methods combined were used in panel C and D. Each grey dot refers to a detected voxel from a subject (N = 10 subjects). At 10 Hz stimulation, striatal responses are not detected, therefore we did not include the plots showing the onset and duration in the striatum in panel A and C. The overlaid probability density color map was calculated with a histogram of 50 bins along each axis. Non-smoothed ofMRI data are used in each panel.*

different threshold settings are used (Figure 3.7); (ii) raw data is spatially smoothed to increase the signal-to-noise ratio (Figure 3.8); and (iii) fixed-effects analysis at the group level is used (Figure 3.9). By invoking random-effects analysis at the group level, the brain regions detected at the subject level are similarly detected, although with a smaller volume (Figure 3.10). Notably, with random-effects analysis, increasing the model order within each method leads to a larger detection volume with the 10 Hz and 40 Hz stimulation ofMRI datasets. This is because methods with larger numbers of regressors take more contrast images per subject into the second level analysis [ABC08], resulting in a greater number of total degrees of freedom and very sensitive statistical tests. Specifically, in the case of n subjects and k regressors in the model, the total degrees of freedom are $n \times k - 1$ at the second level analysis. This is different from the single-subject and fixed-effects analyses, where the total degrees of freedom are fixed at $m - 1$ for fMRI data with m time frames. As a result, with random-effects analysis, the differences in the detection results across methods are largely governed by the differences in the total degrees of freedom, rather than each method's capabilities to handle heterogeneous BOLD responses.
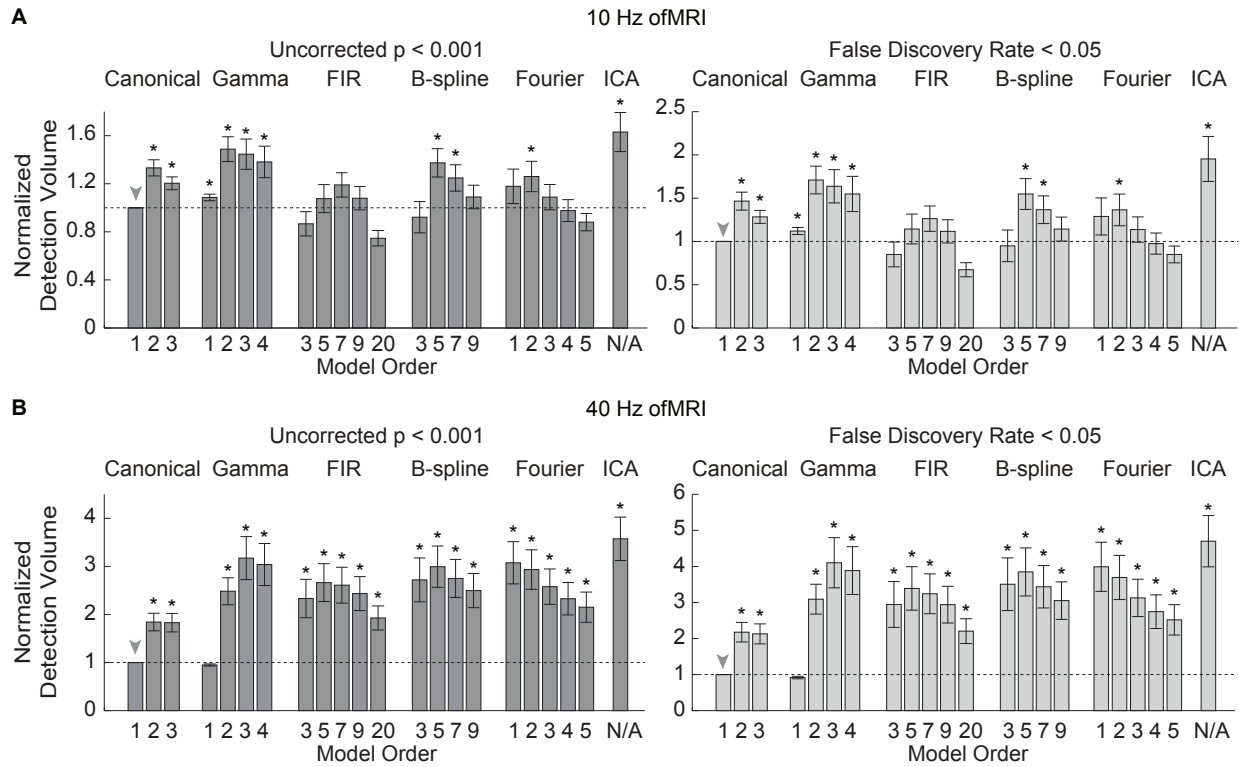
Figure 3.7: ***Detection results with the experimental ofMRI datasets show similar trends within and across methods when different threshold settings are used.*** *To check whether the detection results with the experimental ofMRI data are affected by the choice of threshold settings, we applied two additional threshold settings during statistical analysis. In both cases, similar trends are observed in the detection performance across different model orders within each method and across different methods. (A, B) Bar graphs show normalized detection volume across different threshold settings with the 10 Hz (A) and 40 Hz (B) stimulation ofMRI data. Non-smoothed ofMRI data are used in each panel. The detection volume was first normalized to the active volume detected by GLM with the 1*[st] *order canonical basis set (gray arrowhead and dashed horizontal line) for each subject, and then averaged across different subjects. Error bars represent SEM across different subjects. Asterisk indicates p < 0.05 compared with GLM with the 1*[st] *order canonical basis set using one-sided Wilcoxon signed-rank test (N = 10 subjects).*
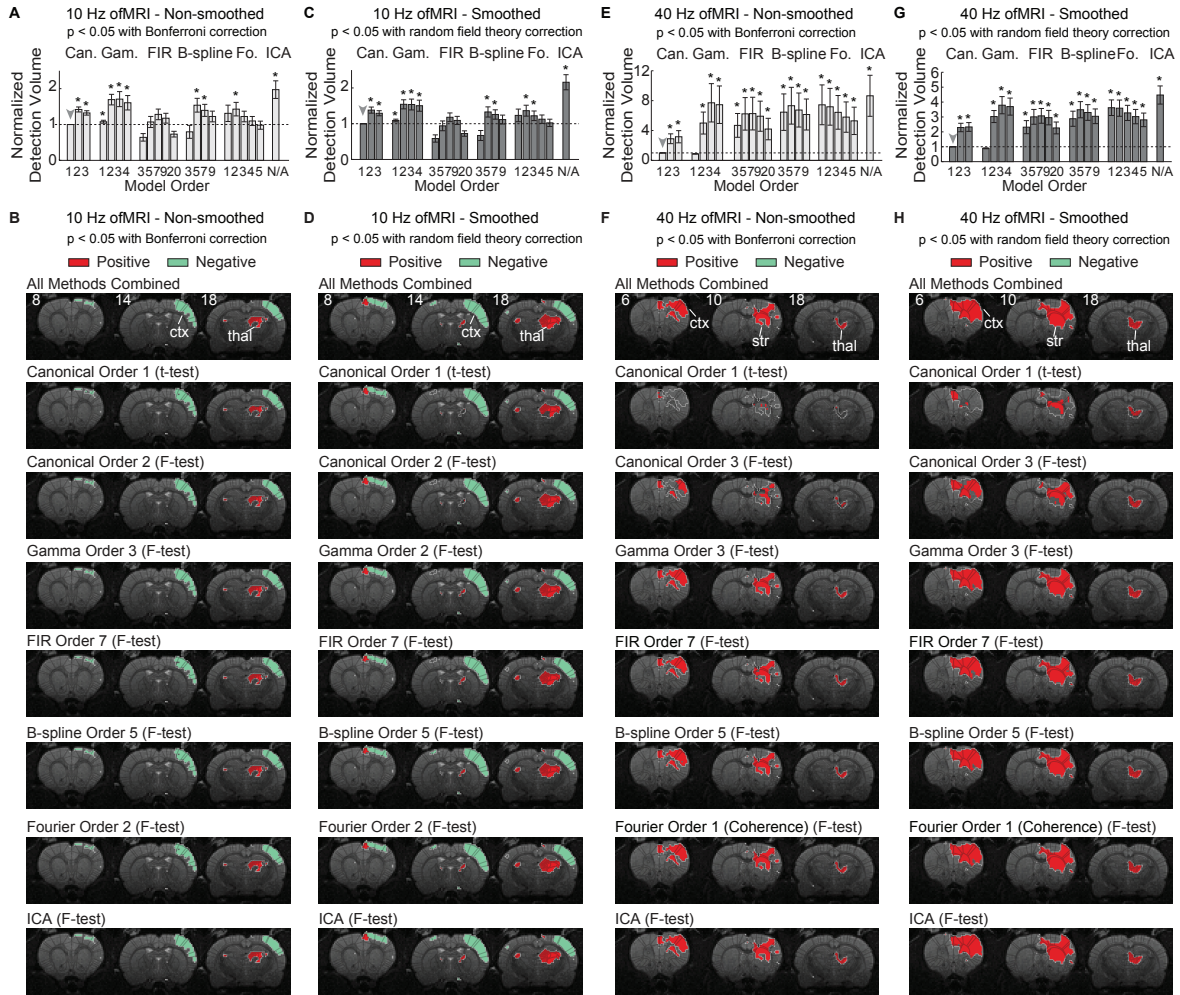
Figure 3.8: ***Detection results for the non-smoothed ofMRI data with Bonferroni correction show similar trends within and across methods as those for the spatially-smoothed ofMRI data with random field theory correction.*** *(A, B, E, F) Detection capability assessment using the non-smoothed experimental ofMRI data with a threshold of p < 0.05 with Bonferroni correction. These panels are identical to panel A, B, E, and F of Figure 3.5. (C, D, G, H) Detection capability assessment using the spatially-smoothed experimental ofMRI data with a threshold of p < 0.05 with random field theory correction. (A, C, E, G) Bar graphs show the active volume detected by each method. The detection volume was first normalized to the active volume detected by GLM with the 1st order canonical basis set (gray arrowhead and dashed horizontal line) for each subject, and then averaged across different subjects. Error bars represent SEM across different subjects. Asterisk indicates p < 0.05 compared with GLM with the 1st order canonical basis set using one-sided Wilcoxon signed-rank test (N = 10 subjects). (B, D, F, H) Activation maps from a representative subject are shown. For simplicity, we show results from conventionally used GLM with the 1st order canonical basis set, as well as from the model order within each method that yields the largest detection volume in panel A, C, E, and G. The gray border represents the superset of voxels that are detected by all tested methods combined. Colored voxels are detected by the method denoted in the figure legend.*

A 10 Hz ofMRI - Fixed Effects
p < 0.05 with random field theory correction

B 40 Hz ofMRI - Fixed Effects
p < 0.05 with random field theory correction

C 10 Hz ofMRI - Fixed Effects
p < 0.05 with random field theory correction

All Methods Combined   Positive Negative

Canonical Order 1 (t-test)

Canonical Order 2 (F-test)

Gamma Order 2 (F-test)

FIR Order 7 (F-test)

B-spline Order 5 (F-test)

Fourier Order 2 (F-test)

ICA (F-test)

D 40 Hz ofMRI - Fixed Effects
p < 0.05 with random field theory correction

All Methods Combined   Positive Negative

Canonical Order 1 (t-test)

Canonical Order 3 (F-test)

Gamma Order 4 (F-test)

FIR Order 7 (F-test)

B-spline Order 5 (F-test)

Fourier Order 1 (Co.) (F-test)

ICA (F-test)

Figure 3.9

76

Figure 3.9: ***Detection results of the fixed-effects analysis at the group level show similar trends within and across methods as the single-subject analysis for the experimental ofMRI data.*** *(A, B) Bar graphs show the active volume detected by each method using the fixed-effects analysis at the group level (N = 10 subjects). The detection volume was normalized to the active volume detected by GLM with the 1st order canonical basis set (gray arrowhead and dashed horizontal line). The threshold was set to $p < 0.05$ with random field theory correction to control the family-wise error rate in each panel. The model order that yields the largest detection volume within each method is denoted by black arrowheads. (C, D) Activation maps of the fixed-effects analysis are shown. For simplicity, we show results from conventionally used GLM with the 1st order canonical basis set, as well as from the model order within each method that yields the largest detection volume in panel A and B. The gray border represents the superset of voxels that are detected by all tested methods.Colored voxels are detected by the method denoted in the figure legend. The polarity of the detected responses was calculated using the BOLD responses averaged across each subject. The evoked response is considered positive if the average percent signal change over entire stimulation cycle is above zero, otherwise is considered negative. T2-weighted anatomical images are used as underlays. Abbreviations are as follows: Can. (canonical), Gam. (gamma), Fo. (Fourier), co (coherence analysis), ctx (cortex), str (striatum), and thal (thalamus).*

A 10 Hz ofMRI - Random Effects
p < 0.05 with random field theory correction

B 40 Hz ofMRI - Random Effects
p < 0.05 with random field theory correction

C 10 Hz ofMRI - Random Effects
p < 0.05 with random field theory correction

D 40 Hz ofMRI - Random Effects
p < 0.05 with random field theory correction

Figure 3.10

Figure 3.10: **_Differences in the random-effects results within and across methods are largely governed by the differences in the total degrees of freedom at the second level analysis._** *(A, B) Bar graphs show the active volume detected by each method using the random-effects analysis at the group level (N = 10 subjects). The detection volume was normalized to the active volume detected by GLM with the 1st order canonical basis set (gray arrowhead and dashed horizontal line). The threshold was set to $p < 0.05$ with random field theory correction to control the family-wise error rate in each panel. The model order that yields the largest detection volume within each method is denoted by black arrowheads. (C, D) Activation maps of the random-effects analysis are shown. For simplicity, we show results from conventionally used GLM with the 1st order canonical basis set, as well as from the model order within each method that yields the largest detection volume in panel A and B. The gray border represents the superset of voxels that are detected by all tested methods.Colored voxels are detected by the method denoted in the figure legend. The polarity of the detected responses was calculated using the BOLD responses averaged across each subject. The evoked response is considered positive if the average percent signal change over entire stimulation cycle is above zero, otherwise is considered negative. T2-weighted anatomical images are used as underlays. Abbreviations are as follows: Can. (canonical), Gam. (gamma), Fo. (Fourier), ctx (cortex), str (striatum), and thal (thalamus).*

We then examine each method's detection performance with the control ofMRI data. In the group of control subjects, saline was injected into the brain instead of ChR2-expressing virus. Therefore, we do not expect any optogenetically-evoked neuronal activity, and assume all detected responses with the control dataset to be false positive. In other words, methods with smaller detection volumes are preferred. As shown in Figure 3.11A and B, most of the methods detect similar volumes as the 1st order canonical basis set. However, ICA detects a considerably larger volume of 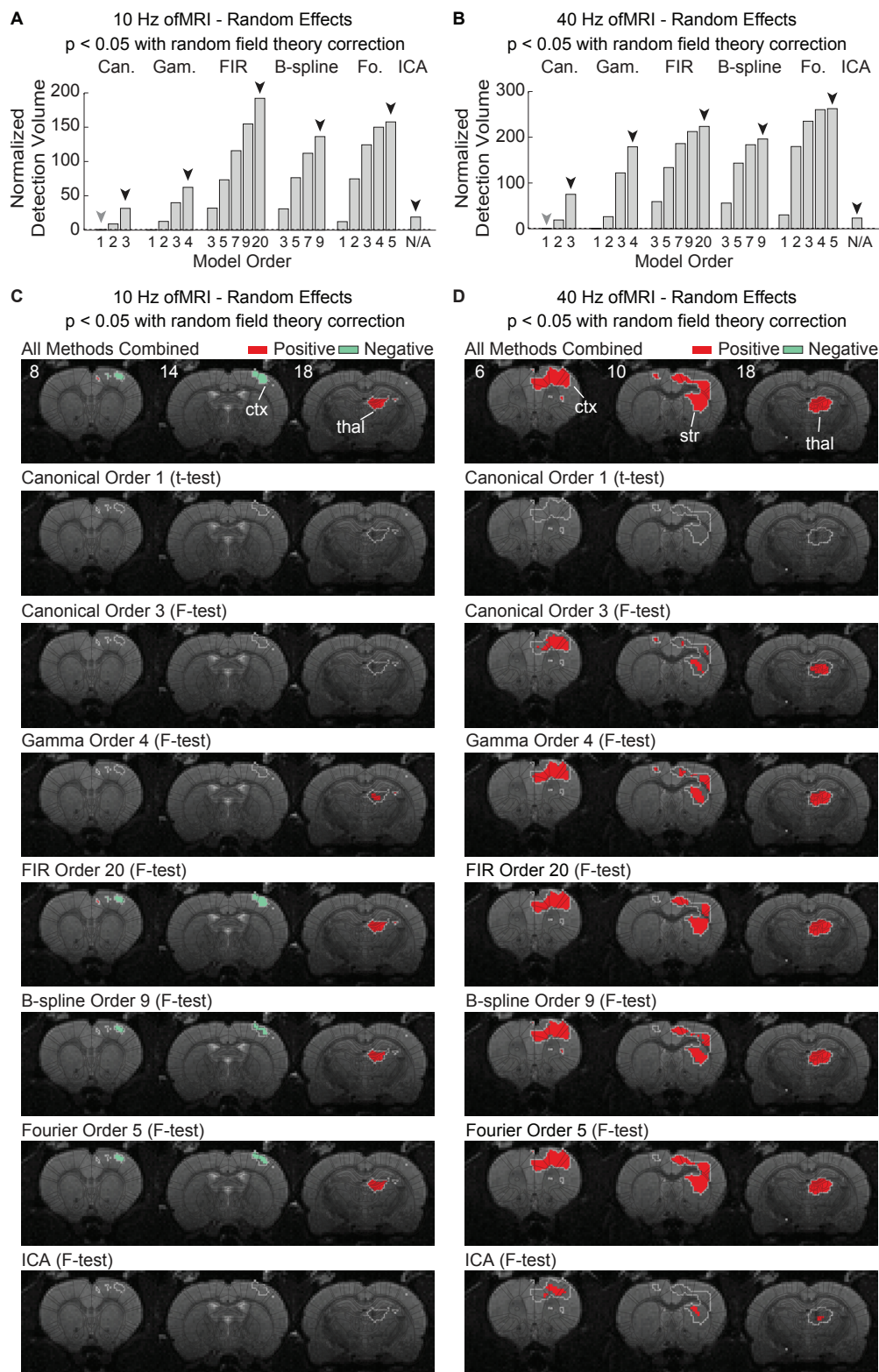spurious activations than any other methods. Similar results are obtained when different threshold settings are used (Figure 3.12A-F), and when the control data is spatially smoothed to increase the signal-to-noise ratio (Figure 3.12G, H).

To summarize the above-described detection results with experimental and control ofMRI datasets at varying thresholds, we generate modified ROC curves and calculate AUC values for each method (Figure 3.11C-F). ROC curves with large areas under the curve and hence high AUC values are preferred as they indicate the method's ability in yielding a large detection volume with the experimental ofMRI data while maintaining a small amount of spurious detections with the control ofMRI data across different threshold settings. With both 10 Hz and 40 Hz stimulation ofMRI datasets, most of the methods yield significantly higher AUC values compared to the 1st order canonical basis set (Figure 3.11C, D). Compared to the detection volume results with the experimental ofMRI data, we observe similar trends within and across methods except with ICA. ICA detects the largest volume with the experimental ofMRI data, but yields one of the lowest AUC values. This is consistent with previous results that ICA detects a larger volume of false positive activations than any other methods with the control ofMRI data. Similar detection results are obtained when using an ofMRI dataset with a different block-design paradigm (Figure 3.13E and F). With the ofMRI data, we show that the 2nd and 3rd order canonical basis sets, the 2nd to 4th order gamma basis sets, the 5th to 20th order FIR basis sets, the 5th to 9th order B-spline basis sets, and the 2nd to 5th order Fourier basis sets yield high AUC values and good detection capabilities (Figure 3.11C-F, Table 3.1).
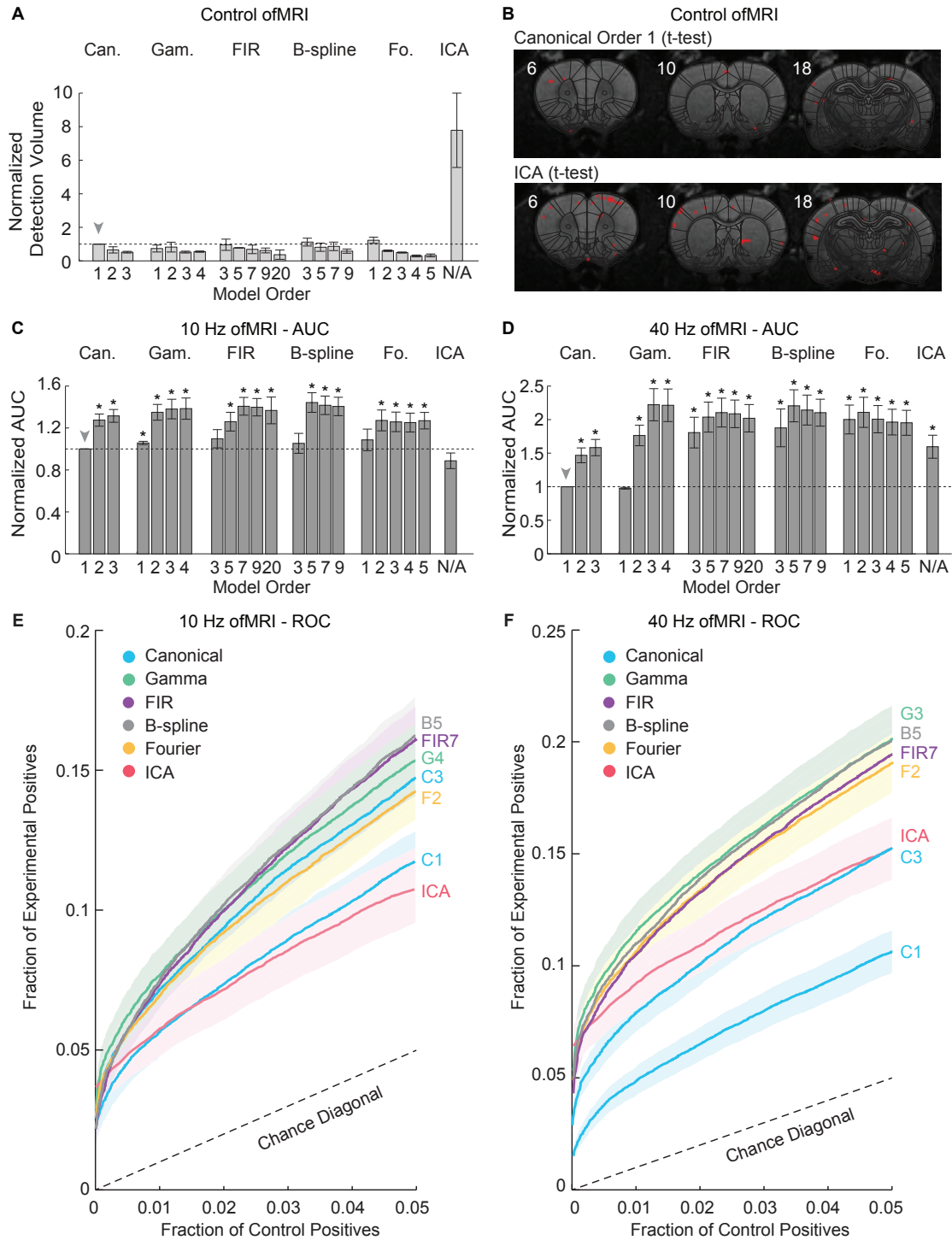
Figure 3.11: ***GLM with the 2nd and 3rd order canonical basis sets, the 2nd to 4th order gamma basis sets, the 5th to 20th order FIR basis sets, the 5th to 9th order B-spline basis sets, and the 2nd to 5th order Fourier basis sets show good detection performance with the ofMRI datasets.***

Figure 3.11: *(A) Bar graph shows the normalized detection volume with the control ofMRI data. The detection volume was first normalized to the active volume detected by GLM with the 1st order canonical basis set for each subject (gray arrowhead and dashed horizontal line), and then averaged across different subjects. Error bars represent SEM across different subjects (N = 2 subjects). Non-smoothed ofMRI data are used in each panel. The threshold was set to uncorrected p < 0.001 in panel A and B to better show the spurious activations detected by each method. Please see Figure 3.12 and its figure caption for results with other threshold settings. (B) Activation maps from a representative subject are shown. T2-weighted anatomical images are used as underlays. In this subject, one signal component was extracted for ICA and t-test was used during statistical analysis. (C, D) Bar graphs represent normalized AUC values for each method. AUC values were first normalized to the AUC value yielded by GLM with the 1st order canonical basis set (gray arrowhead and dashed horizontal line) for each subject, and then averaged across different subjects. Error bars represent SEM across different experimental subjects. Asterisk indicates p < 0.05 compared with GLM with the 1st order canonical basis set using one-sided Wilcoxon signed-rank test (N = 10 subjects). (E, F) Modified ROC curves are shown. For simplicity, we show results from conventionally used GLM with the 1st order canonical basis set, as well as from the model order within each method that yields the largest AUC values in panel C and D. Shaded areas represent SEM across different experimental subjects (N = 10 subjects). C1 to C3, G1 to G4, FIR3 to FIR20, B3 to B9, and F1 to F5 refer to different model orders in the canonical, gamma, FIR, B-spline, and Fourier basis sets. Abbreviations are as follows: Can. (canonical), Gam. (gamma), and Fo. (Fourier).*
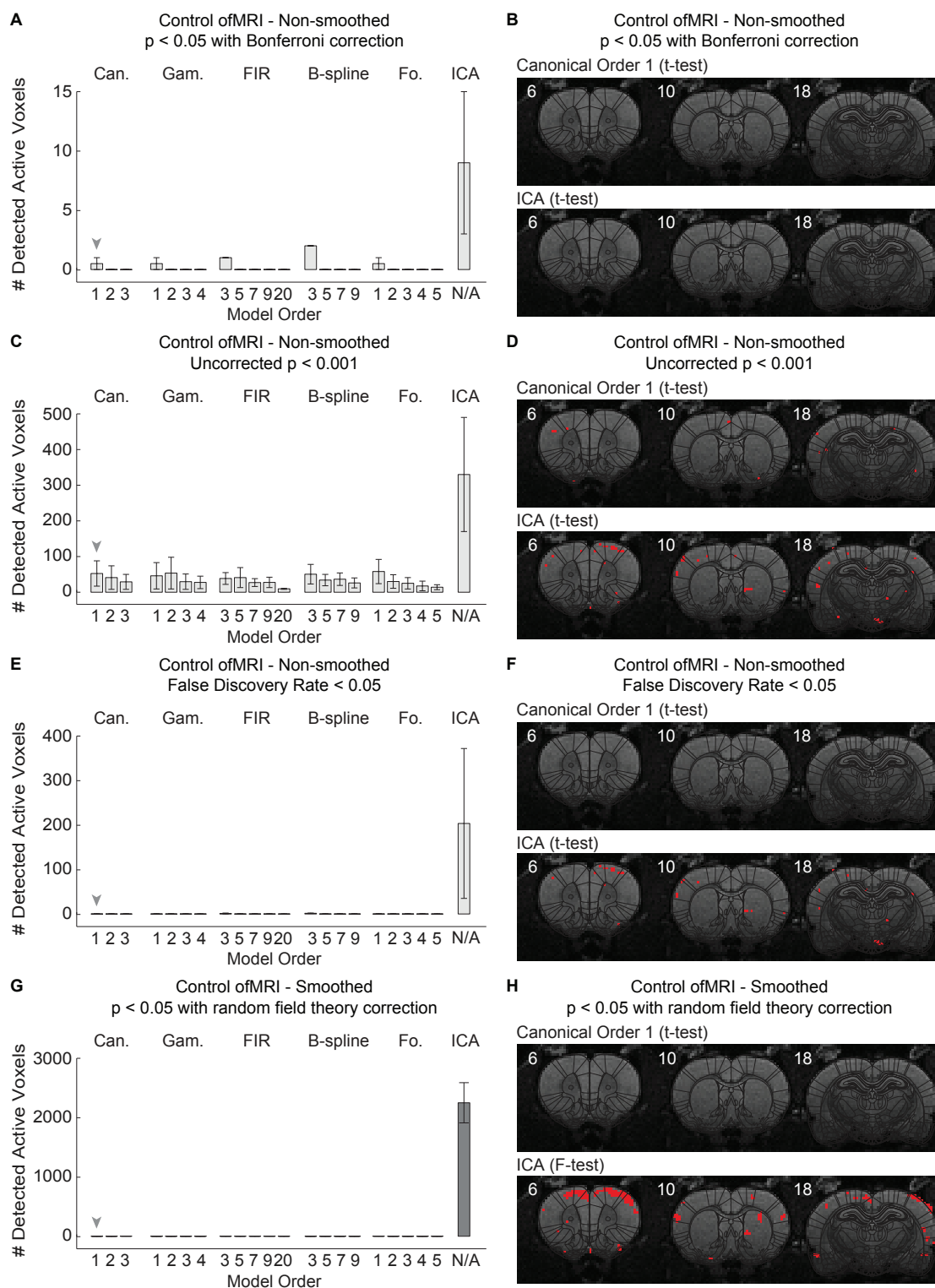
Figure 3.12: *ICA detects a larger volume of spurious activations than any other methods with the control ofMRI data.*

Figure 3.12: *(A-F) ICA detects a larger volume of spurious activations than any other methods with the non-smoothed control ofMRI data across different threshold settings. (A, C, E) Bar graphs showing the number of detected active voxels with the control ofMRI data. Error bars represent SEM across different subjects (N = 2 subjects). As the 1st order canonical basis set (gray arrowhead) does not detect any active voxels in some cases (e.g., panel E and G), we did not normalize the detection volume of each method relative to the 1st order canonical basis set. Instead, we show the number of detected active voxels for each method. For the same reason, we did not show the dashed horizontal line that represents the results using the 1st order canonical basis set as in other figures. Additionally, as in some cases, most of the methods do not detect any active voxels (e.g., panel E and G), we did not denote the model order that yields the smallest detection volume within each method by black arrowheads. Note that, the results shown in panel C are based on the same data, regressors, and threshold settings as Figure 3.11A. The difference between them is that, before averaging across different subjects, the detection volume was normalized within each subject in Figure 3.11A, but not here. It is worth noting that, in panel A and B, when the threshold was set to $p < 0.05$ with Bonferroni correction, very few active voxels are detected by each method with the control ofMRI data. There, ICA detects the largest volume of spurious activations among different methods, but with ~ 10 detected voxels on average. With less stringent threshold settings, ICA detects more evident spurious activations than other methods. These results are consistent with the AUC results shown in Figure 3.11C-F, which summarize the detection volume of each method with the experimental and control ofMRI data across different thresholds. (B, D, F) Activation maps from a representative subject are shown. T2-weighted anatomical images are used as underlays. In this subject, one signal component was extracted from the non-smoothed data and t-test was used during statistical analysis for ICA. Note that, panel D is identical to Figure 3.11B. (G, H) ICA detects a larger volume of spurious activations than any other methods with the spatially-smoothed control ofMRI data. The control ofMRI data were spatially smoothed with a 0.5 mm FWHM Gaussian kernel. Thresholds were set to $p < 0.05$ with random field theory correction in both panels. (G) Bar graph showing the number of detected active voxels with the control ofMRI data. (H) Activation maps from a representative subject are shown. T2-weighted anatomical images are used as underlays. A separate ICA component extraction was conducted for each subject as spatial smoothing was involved in the data preprocessing step. Here, four signal components were extracted and used as a set of regressors. F-test was used during statistical analysis for ICA.*

A ofMRI with Alternative Stimulation Block Design
Experimental Paradigm
— 10 s

B All Methods Combined
■ Positive ■ Negative
6 10 18

C Detected BOLD Responses
All Methods Combined
% Signal Change
10 s

D Observed Data
All Methods Combined
Duration / s
Onset / s
Canonical Response
x10⁻³

E ofMRI with Alternative Stimulation Block Design
Detection Volume
Can. Gam. FIR B-spline Fo. ICA
Normalized Detection Volume
123 1234 357920 3579 12345 N/A
Model Order

F AUC
Can. Gam. FIR B-spline Fo. ICA
Normalized AUC
123 1234 357920 3579 12345 N/A
Model Order

G RMSE
Can. Gam. FIR B-spline Fo. ICA
Average RMSE / PSC
123 1234 357920 3579 12345 N/A
Model Order

Figure 3.13: ***Detection and characterization results show similar trends within and across methods for the ofMRI datasets with a different block-design paradigm.*** *(A) Illustration of the experimental paradigm. Blue boxcars represent the 10 s period of optical stimulation. (B) Activation maps detected by all methods combined are shown. One subject with 100 Hz optical stimulation in the central thalamus is included. The superset of voxels detected by all tested methods were used in panel B, C, D, and G. Thresholds were set to $p < 0.05$ with Bonferroni correction in panel B, C, D, E, and G. Non-smoothed ofMRI data are used in each panel. (C) Plots showing observed hemodynamic responses averaged across all detected voxels. Error bars represent SEM across different stimulation cycles. (D) Plots showing the onset and duration measured from the observed data. Each grey dot refers to a detected voxel. (E) Bar graphs showing normalized detection volume. The detection volume was normalized to the active volume detected by GLM with the 1ˢᵗ order canonical basis set (gray arrowhead and dashed horizontal line). The model order that yields the largest detection volume within each method is denoted by black arrowheads. (F) Bar graphs showing normalized AUC value. AUC value was normalized relative to GLM with the 1ˢᵗ order canonical basis set (gray arrowhead). The model order that yields the largest AUC within each method is denoted by black arrowheads. (G) Bar graphs showing RMSE. The model order that yields the smallest RMSE within each method is denoted by black arrowheads.*

3.3.3 Characterization capability assessment with ofMRI datasets

GLM with the 4th order gamma basis set, the 20th order FIR basis set, the 7th to 9th order B-spline basis sets, and the 3rd to 5th order Fourier basis sets show good characterization performance with the ofMRI datasets

First, we examine the characterization errors of each method. With the 10 Hz and 40 Hz stimulation ofMRI datasets, the 4th order gamma basis set, the 20th order FIR basis set, the 7th to 9th order B-spline basis sets, and the 3rd to 5th order Fourier basis sets consistently yield significantly lower onset errors, duration errors, and RMSE compared to the 1st order canonical basis set (Figure 3.14A-C), suggesting good characterization performance. As shown in Figure 3.14C, increasing the model order within each method leads to a decrease in the RMSE. This is because with the ofMRI data, RMSE is calculated relative to the observed time courses, and any increase in the model order within each method naturally leads to a better fit to the observed data. Similar characterization results are obtained when analyzing an ofMRI dataset with a different block-design paradigm (Figure 3.13G).

Next, we take a closer look at the onset and duration estimated by different methods at each detected voxel. As shown in Figure 3.14D, the onset and duration estimated by the 4th order gamma basis set, the 9th order B-spline basis set, and the 5th order Fourier basis set show similar patterns as those measured from the observed data, while the values estimated by the canonical basis set show a clear deviation, suggesting biased estimations. Since each regressor in the 20th order FIR basis set has a bin width of the image acquisition interval (3 seconds), their onset and duration estimates are therefore fixed at integer multiples of 3 seconds and do not show a continuous pattern in Figure 3.14D. As shown in Figure 3.2, ICA extracts two signal components in most of the subjects. With these subjects, ICA yields a fixed duration value for each estimated onset value (Figure 3.14D), and cannot characterize the differences among BOLD responses that share the same onset but different duration. This is the same with other methods that have two regressors, such as the 2nd order canonical basis set, the 2nd order gamma basis set, and the 1st order Fourier basis set (coherence analysis) (data not shown).

Figure 3.14: *GLM with the 4th order gamma basis set, the 20th order FIR basis set, the 7th to 9th order B-spline basis sets, and the 3rd to 5th order Fourier basis sets show good characterization performance with the ofMRI datasets. The results in each panel were calculated using the superset of voxels detected by all methods combined, rather than the voxels detected by each method. This way each method's characterization capabilities can be assessed without the influence of their detection performance. Non-smoothed ofMRI data were used and the threshold is set to $p < 0.05$ with Bonferroni correction in each panel. (A-C) Bar graphs show the average onset error (A), duration error (B), and RMSE (C). In panel A, the onset errors of some methods are beyond the upper limit of the plot. Therefore, these values are not shown to better illustrate the onset errors of the rest methods. The methods with extreme onset errors include the 3rd and 5th order FIR basis sets and the 1st order Fourier basis set with the 10 Hz stimulation ofMRI data, and the 3rd order FIR basis set with the 40 Hz stimulation ofMRI data. The onset and duration error was calculated relative to the onset and duration measured from the observed time course and is in the unit of seconds. RMSE was calculated relative to the observed data and is in the unit of percent signal change (PSC). The mean errors in panel A to C were calculated by first averaging the errors across different detected voxels within each subject, and then averaging across different subjects.*

Figure 3.14: *Error bars represent SEM across different subjects. Asterisk indicates p < 0.05 compared with GLM with the 1st order canonical basis set using one-sided Wilcoxon signed-rank test (N = 10 subjects). The results using GLM with the 1st order canonical basis set is denoted with a gray arrowhead and a dashed horizontal line. (D) Plots show the onset and duration measured from the observed data (top panel) and estimated by each method (bottom panels). For simplicity, we show results from conventionally used GLM with the 1st order canonical basis set, as well as from the model order within each method that yields the lowest errors in panel A to C. Each grey dot refers to a detected voxel from a subject (N = 10 subjects). The probability density color map is overlaid. Note that, the plots for the 1st order canonical basis set are identical to those in Figure 3.4K and L.*

3.3.4 Detection capability assessment with simulated datasets

GLM with the 2nd to 4th order gamma basis sets, the 5th to 9th order FIR basis sets, the 5th to 9th order B-spline basis sets, the 1st to 5th order Fourier basis sets, and ICA show good detection performance with the simulated datasets

To further validate the above results obtained with ofMRI data, we conducted the assessment using simulated data with varying onset and duration. Three probability distributions of onset and duration are used in the calculation of summarized results. The 10 Hz and 40 Hz stimulation ofMRI data distributions are based on the bivariate probability distributions of onset and duration estimated from the experimental ofMRI data. The uniform distribution is equivalent to averaging across the analysis results from the simulated datasets with different signal shapes.

The detection results of simulated data are summarized in Figure 3.15. First, we examine the TPR metric (Figure 3.15A, B). Unlike other methods, the 1st to 3rd order canonical basis sets and the 1st and 2nd order gamma basis sets can only detect small onset and duration deviations from the canonical response. Across different distributions of onset and duration, the 3rd and 4th order gamma basis sets, the 5th to 9th order FIR basis sets, the 5th to 9th order B-spline basis sets, the 1st to 5th order Fourier basis sets, and ICA similarly yield high TPR (Figure 3.15B).

Next, we examined the FPR metric. As shown in Figure 3.15C and D, in each method, false positives are not detected in the majority of the simulation. ICA detects a larger volume of spurious activations than any other methods with the control ofMRI data (Figure 3.14A, B), but yields similar FPR as other methods with the simulated data across different threshold settings
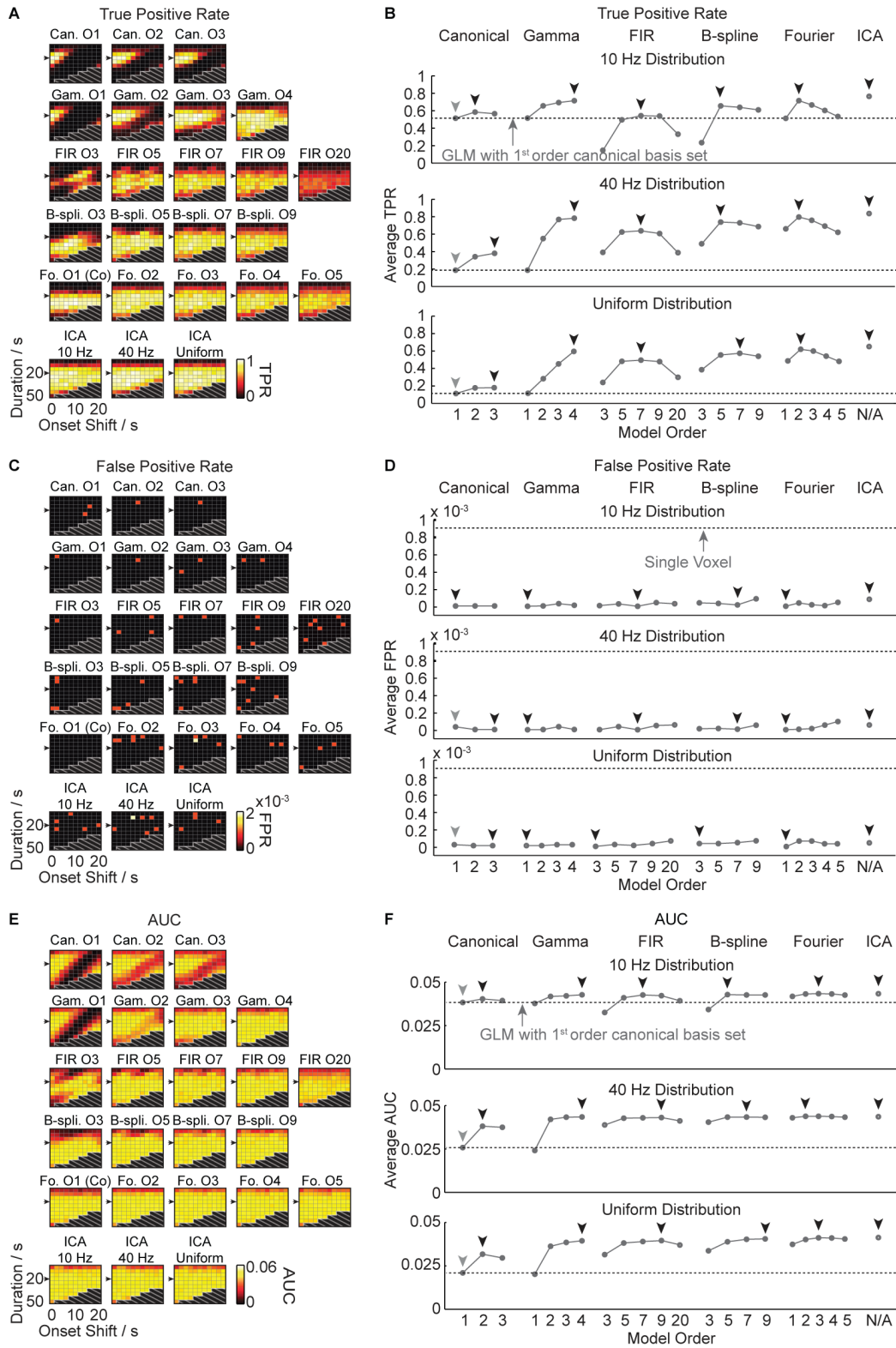
Figure 3.15
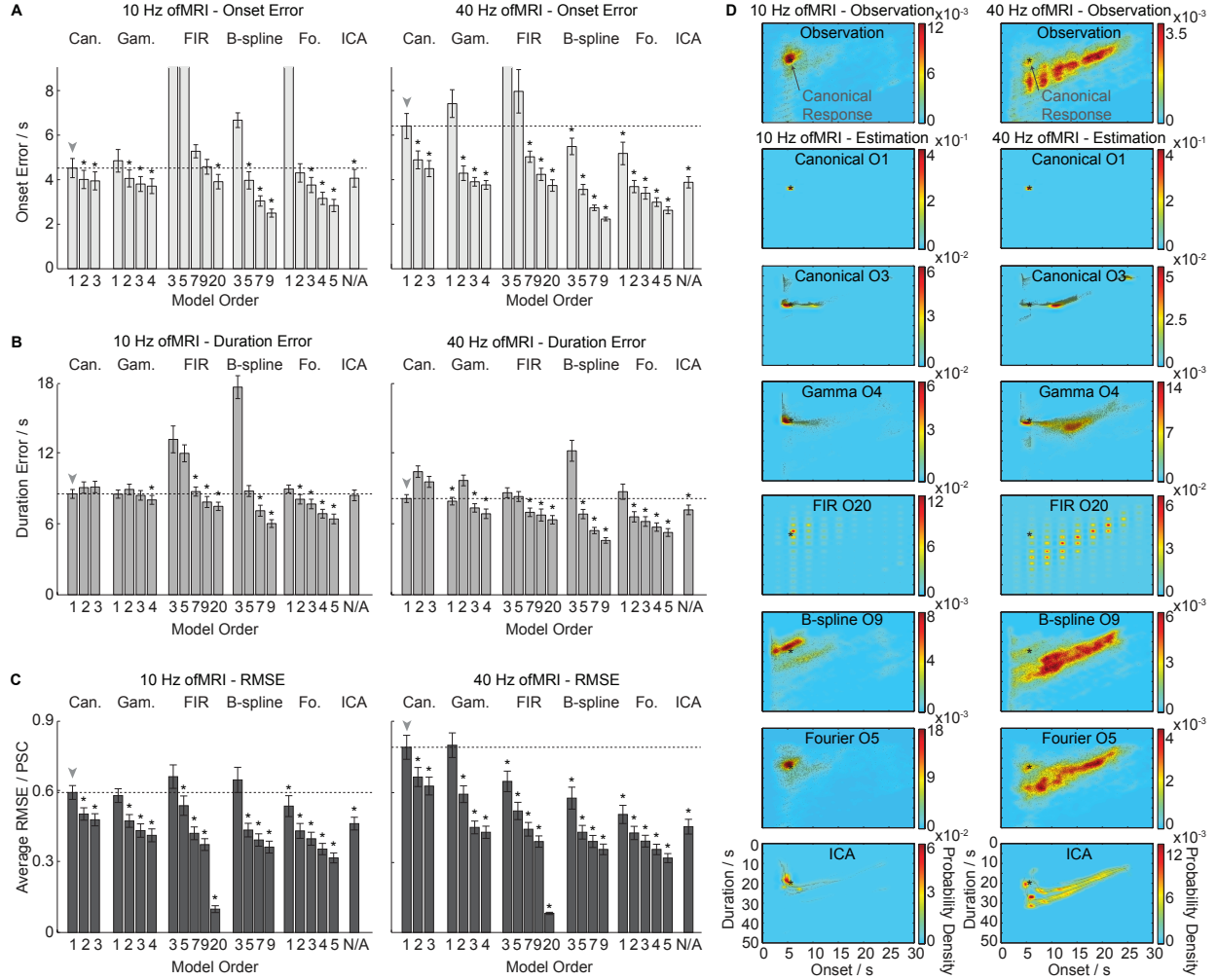
Figure 3.15: ***GLM with the 2nd to 4th order gamma basis sets, the 5th to 9th order FIR basis sets, the 5th to 9th order B-spline basis sets, the 1st to 5th order Fourier basis sets, and ICA show good detection performance with the simulated datasets.*** *(A, C, E) Colormaps show true positive rate (A), false positive rate (C), and AUC (E) for each method. Threshold was set to p < 0.05 with Bonferroni correction in panel A-D. CNR is 1.5 in each panel. Results from the simulated shape that matches the canonical response is denoted by black arrowheads. (B, D, F) Plots show average true positive rate (B), false positive rate (D), and AUC (F). The results using GLM with the 1st order canonical basis set is denoted with a gray arrowhead and a dashed horizontal line. The model order that yields the highest true positive rate, the lowest false positive rate, and the highest AUC within each method is denoted by black arrowheads. B-spli. stands for B-spline.*

(Figure 3.15C, D, Figure 3.16A).

To summarize the TPR and FPR metrics at varying thresholds, we generate ROC curves and calculate AUC values for each method. Across different distributions of onset and duration, the 2nd to 4th order gamma basis sets, the 5th to 20th order FIR basis sets, the 5th to 9th order B-spline basis sets, the 1st to 5th order Fourier basis sets, and ICA similarly yield the highest AUC (Figure 3.15E, F). Detection results with similar trends within and across methods are obtained when different threshold settings are applied (Figure 3.16) and under different CNR levels (Figure 3.17), with the exception that at lower CNR levels, the 20th order FIR basis set underperforms relative to other methods (Figure 3.17C, Table 3.1).
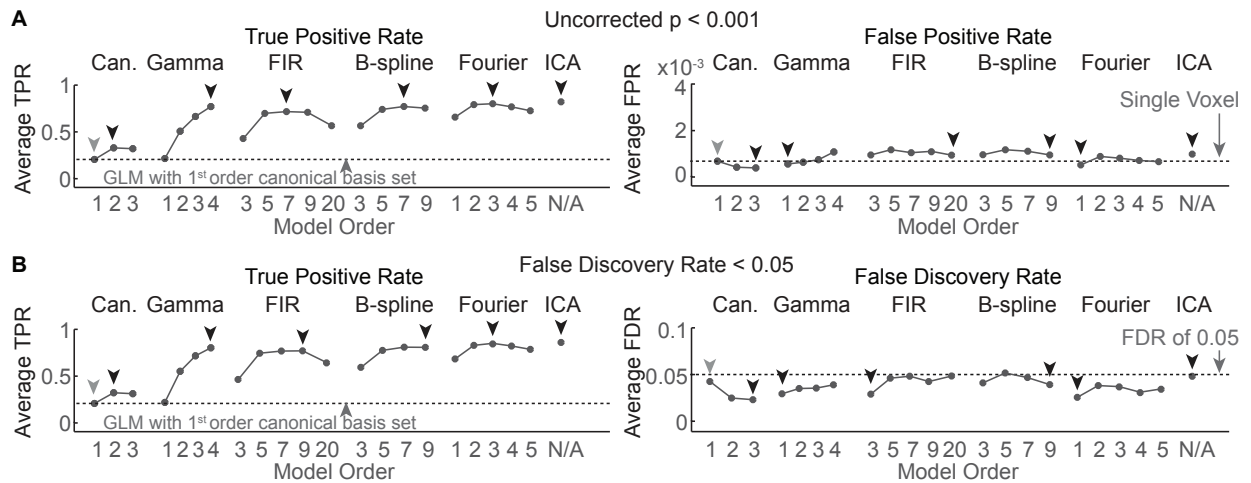
Figure 3.16: ***Consistent detection results are observed across different threshold settings with simulated data.****(A) Plots showing the average true and false positive rate at the threshold of uncorrected p < 0.001. CNR of the simulation is 1.5 and uniform distribution across onset and duration is used in each panel. (B) Plots showing the average true positive rate and false discovery rate (FDR) at the threshold of FDR < 0.05. Since FDR-based thresholds do not control over the false positive rate, here we plot the FDR value instead of the false positive rate results. GLM with the 1st order canonical basis set is denoted by a gray arrowhead. The model order that yields the highest TPR, the lowest FPR, and the lowest FDR within each method is denoted by black arrowheads.*
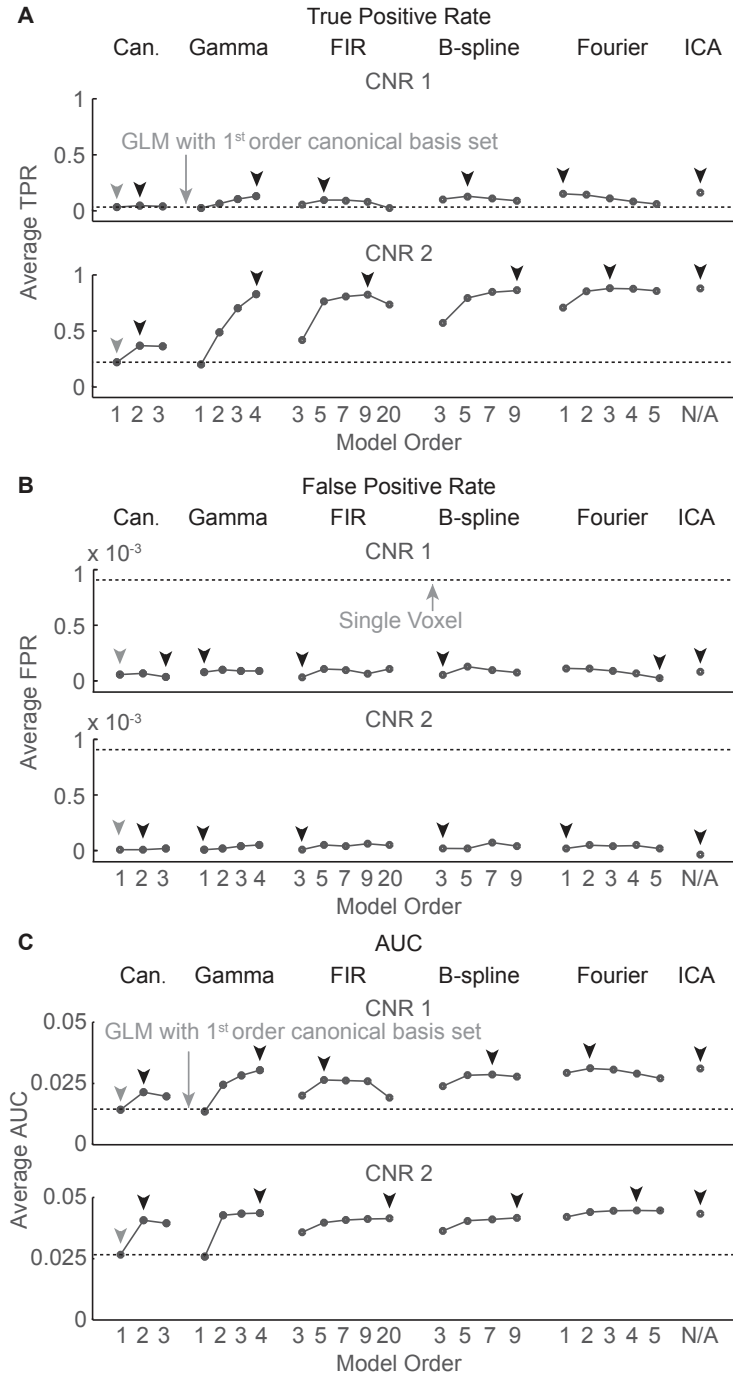
Figure 3.17: **Consistent detection results are observed across different CNR levels with simulated data.**(A-C) Plot showing the average true positive rate (A), false positive rate (B), and AUC (C) across different CNR levels. Threshold is set to $p < 0.05$ with Bonferroni correction in panel A and B. Uniform distribution across onset and duration is used. GLM with the 1st order canonical basis set is denoted by a gray arrowhead. The model order that yields the highest TPR, the lowest FPR, and the highest AUC within each method is denoted by black arrowheads.

3.3.5 Characterization capability assessment with simulated datasets

GLM with the 3rd and 4th order gamma basis sets, the 5th to 9th order FIR basis sets, the 5th to 9th order B-spline basis sets, the 2nd to 5th order Fourier basis sets, and ICA show good characterization performance with the simulated datasets

The characterization results of the simulated data are shown in Figure 3.18. First, we examine the estimation errors of onset and duration (Figure 3.18A-D). For the canonical basis set, adding the 2nd and 3rd order decreases the onset errors, but at the cost of the duration errors. Across different distributions of onset and duration, the 3rd and 4th order gamma basis sets, the 5th to 9th order FIR basis sets, the 5th to 9th order B-spline basis sets, the 2nd to 5th order Fourier basis sets, and ICA similarly yield low onset and duration errors. Note that, four signal components are extracted using ICA with each distribution of onset and duration (Figure 3.19A).

Finally, RMSE is used to assess each method's capability to predict the observed BOLD responses. As shown in Figure 3.18E and F, the 1st to 3rd order canonical basis sets and the 1st and 2nd order gamma basis sets yield small RMSE near the canonical response, but large RMSE when onset and duration deviate substantially. Across different distributions of onset and duration, the 3rd and 4th order gamma basis sets, the 5th to 9th order FIR basis sets, the 5th to 9th order B-spline basis sets, the 1st to 5th order Fourier basis sets, and ICA similarly yield low RMSE. Characterization results with similar trends within and across methods are obtained when analyzing the simulated datasets with different CNR levels (Figure 3.20), with the exception that at higher CNR levels, the 1st order Fourier basis set (coherence analysis) underperforms relative to other methods, especially with the 10 Hz stimulation ofMRI data distribution (Table 3.1).

93
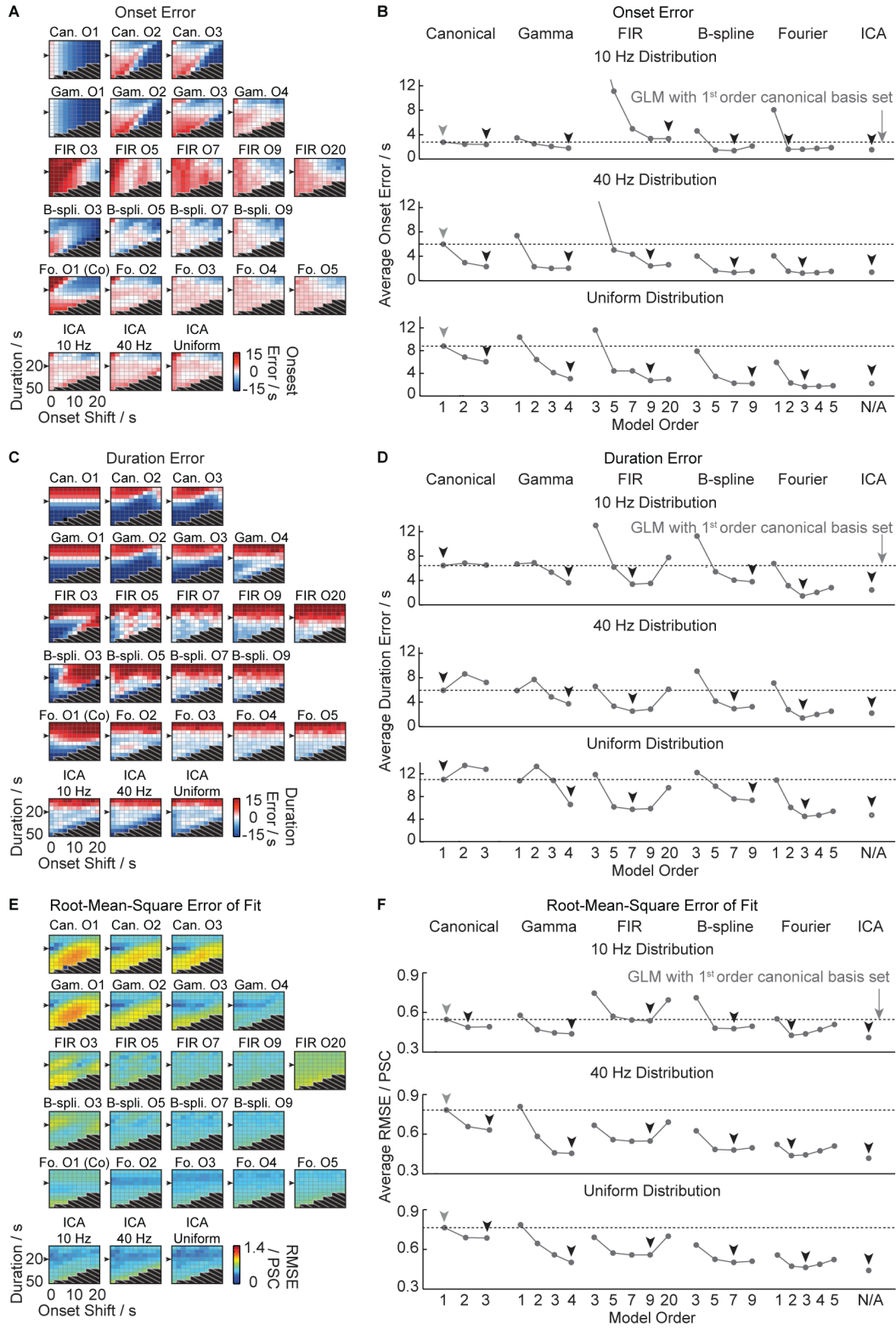
Figure 3.18

Figure 3.18: **GLM with the 3rd and 4th order gamma basis sets, the 5th to 9th order FIR basis sets, the 5th to 9th order B-spline basis sets, the 2nd to 5th order Fourier basis sets, and ICA show good characterization performance with the simulated datasets.** *Similar to Figure 3.14, the results in each panel were calculated using the ground truth positive voxels rather than the voxels detected by each method, so that each method's characterization capability can be assessed without the influence of their detection performance. (A, C, E) Colormaps show onset errors (A), duration errors (C), and RMSE of fit (E) for each method. Color bar represents onset and duration errors in the unit of seconds, and RMSE in the unit of percent signal change (PSC). CNR is 1.5 in each panel. (B, D, F) Plots show average onset errors (B), duration errors (D), and RMSE (F). The results using GLM with the 1st order canonical basis set is denoted with a gray arrowhead and a dashed horizontal line. The model order that yields the smallest errors within each method is denoted by black arrowheads. Note that, in panel B, the onset errors of the 3rd order FIR basis set with the 10 Hz and 40 Hz stimulation ofMRI data distributions are beyond the upper limit of the plot and therefore are not shown to better illustrate the onset errors of the rest methods.*

A Signal Component Time Course

10 Hz Distribution

40 Hz Distribution

Uniform Distribution

Overlay

– 20 s

B Signal Component Time Course

CNR 1

CNR 1.5

– 20 s

CNR 2

Overlay

C Signal Component Time Course

20

85

Overlay

– 20 s

Figure 3.19

Figure 3.19: ***Different signal components are extracted across simulated datasets with different onset and duration distributions and across different CNR levels.*** *In each panel, the signal components that yield the highest correlation coefficient are aligned vertically and overlaid together in the bottom row. (A) Distinct signal components are obtained when analyzing simulated datasets with different distributions of onset and duration. CNR is set to 1.5 and the number of independent components was set to 20. (B) With different CNR levels of 1, 1.5, and 2, we see additional signal components being uncovered with higher CNR levels. Simulated datasets with uniform distribution across onset and duration is used and the number of independent components was set to 20. (C) Negligible differences are observed when different numbers of total independent components were used for ICA analysis. CNR of the simulation is 1.5 and uniform distribution across onset and duration is used. Results from ICA analysis with 20 and 85 total independent components are shown. The number 20 refers to the default setting for the ICA software used in the present study, while the number 85 represents the number of distinct signal shapes in the simulated datasets.*
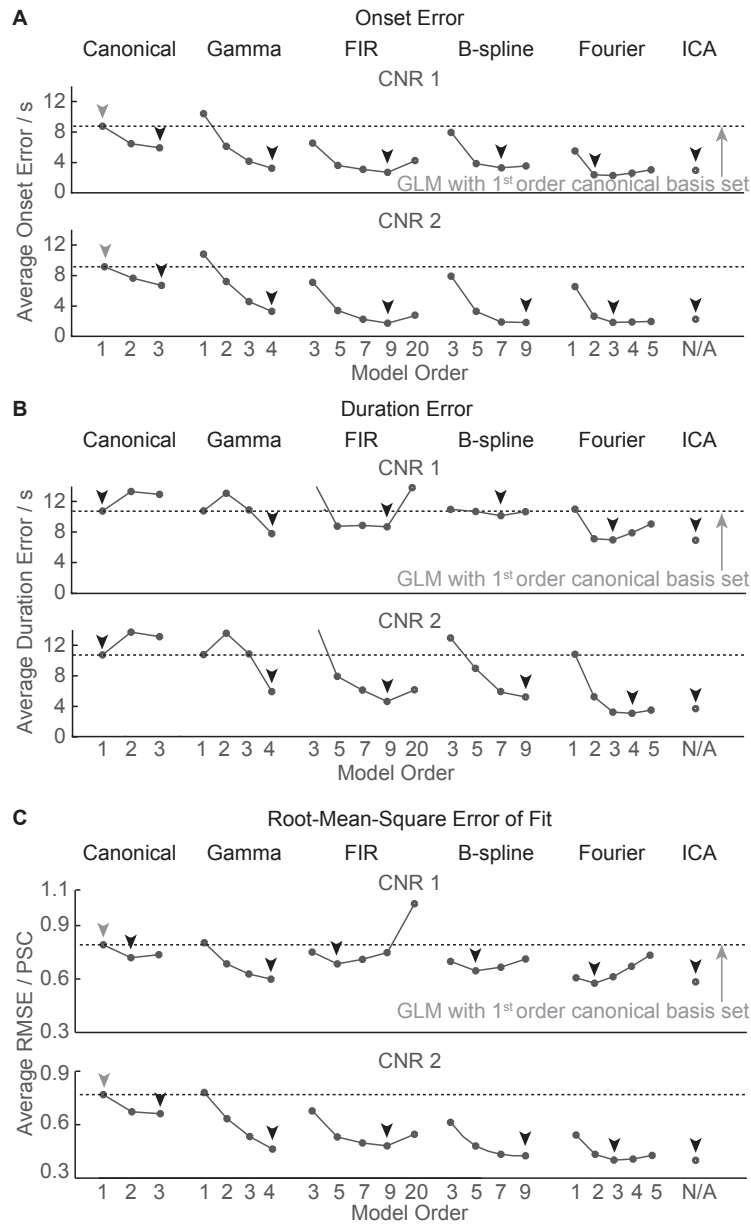
Figure 3.20: **Consistent characterization results are observed across different CNR levels with simulated data.** *(A-C) Plot showing the average onset error (A), duration error (B), and RMSE (C) at CNR of 1 and 2. Results are obtained from the uniform distribution across onset and duration. The ground truth positive voxels are included in each panel. GLM with the 1st order canonical basis set is denoted by a gray arrowhead. The model order that yields the smallest errors within each method is denoted by black arrowheads. Note that, in panel B, the duration errors of the 3rd order FIR basis set are beyond the upper limit of the plot and therefore are not shown to better illustrate the duration errors of the rest methods.*

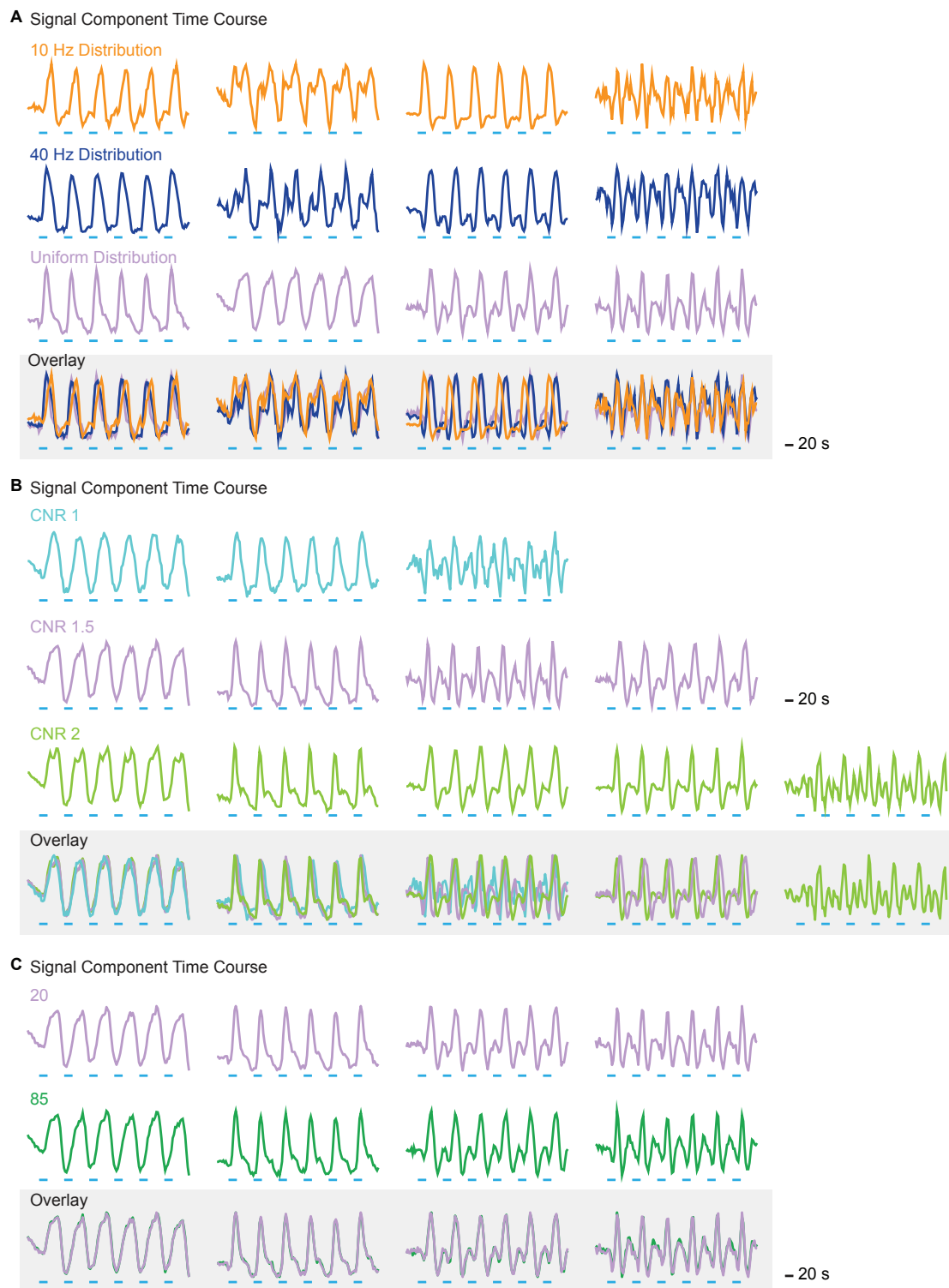### 3.3.6 Summary of detection and characterization assessment

GLM with the 3rd and 4th order gamma basis sets, the 7th to 9th order FIR basis sets, the 5th to 9th order B-spline basis sets, and the 2nd to 5th order Fourier basis sets show good balance between detection and characterization

We summarize each method's detection and characterization performance with the ofMRI and simulated datasets. Each method's AUC and RMSE values are averaged across the 10 Hz and 40 Hz stimulation ofMRI datasets for the real data, and across different CNR levels and distributions of onset and duration for the simulated data (Table 3.1). As shown in Figure 3.21, most of the methods show superior detection and characterization capabilities compared to conventionally used 1st order canonical basis set. To identify the methods that perform well with both the ofMRI and simulated datasets, we standardized the mean AUC and RMSE of each method shown in Figure 3.21A and B, and compared the standardized values across the ofMRI and simulated datasets. As shown in Figure 3.21C, most of the methods exhibit similar detection and characterization performances between the ofMRI and simulated datasets, except for the 20th order FIR basis set and ICA. The 20th order FIR basis set yields low RMSE relative to the observed data with the ofMRI datasets, but exhibits high RMSE relative to the ground truth with the simulated datasets. This is possibly because the 20th order FIR basis set overfits the observed data. ICA yields a high AUC value with the simulated datasets but shows a low AUC value with the ofMRI datasets, as it detects a larger volume of false positive activations than other methods with the control ofMRI data. In summary, with both ofMRI and simulated datasets, we show that the 3rd and 4th order gamma basis sets, the 7th to 9th order FIR basis sets, the 5th to 9th order B-spline basis sets, and the 2nd to 5th order Fourier basis sets exhibit superior detection and characterization performance over other methods.

Figure 3.21: **GLM with the 3rd and 4th order gamma basis sets, the 7th to 9th order FIR basis sets, the 5th to 9th order B-spline basis sets, and the 2nd to 5th order Fourier basis sets show good balance between detection and characterization.** *(A, B) Plot show the mean AUC and RMSE of each method. Non-smoothed ofMRI data were used when calculating AUC and RMSE. The dashed line represents the results using GLM with the 1st order canonical basis set. C1 to C3, G1 to G4, FIR3 to FIR20, B3 to B9, and F1 to F5 refer to different model orders in the canonical, gamma, FIR, B-spline, and Fourier basis sets. Co stands for coherence analysis. (C) Plots show the standardized mean AUC and RMSE of each method. The bottom panel shows an overlay across different methods. For each method, the standardized AUC and RMSE from the ofMRI datasets (solid circle) is connected to the standardized AUC and RMSE from the simulated datasets (open circle) using a colored dashed line. The standardized AUC and RMSE are calculated using the mean AUC and RMSE of each method shown in panel A and B. See Section 3.2.2 for details regarding the calculation of standardized AUC and RMSE.*

Table 3.1

Metrics		AUC (x10e-3)			RMSE (x10e-1)			AUC (x10e-2)										RMSE (x10e-1)									
Datasets		ofMRI			ofMRI			Simulation										Simulation									
CNR		N/A			N/A			1			1.5			2			N/A	1			1.5			2			N/A
Condition		10 Hz	40 Hz	Mean	10 Hz	40 Hz	Mean	10 Hz	40 Hz	Uniform	10 Hz	40 Hz	Uniform	10 Hz	40 Hz	Uniform	Mean	10 Hz	40 Hz	Uniform	10 Hz	40 Hz	Uniform	10 Hz	40 Hz	Uniform	Mean
Canonical	C1	3.84	3.43	3.64	5.91	7.94	6.93	3.22	1.96	1.43	3.83	2.58	2.14	3.92	2.86	2.52	2.78	5.75	7.97	7.92	5.46	7.82	7.64	5.37	7.75	7.69	7.04
Canonical	C2	4.77	4.83	4.80	5.01	6.67	5.84	3.33	2.89	2.14	4.03	3.81	3.21	4.09	4.09	3.85	3.58	5.46	6.85	7.19	4.88	6.56	6.89	4.66	6.36	6.72	6.18
Canonical	C3	4.89	5.21	5.05	4.76	6.28	5.52	3.17	2.80	1.97	3.94	3.75	3.00	4.02	4.04	3.73	3.46	5.81	6.86	7.36	4.91	6.31	6.86	4.61	6.03	6.62	6.15
Gamma	G1	4.07	3.38	3.73	5.78	8.03	6.91	3.09	1.77	1.36	3.77	2.41	2.06	3.85	2.72	2.46	2.67	6.06	8.24	8.04	5.78	8.07	7.86	5.70	8.02	7.81	7.29
Gamma	G2	5.03	5.74	5.39	4.71	5.93	5.32	3.44	3.29	2.45	4.18	4.20	3.67	4.13	4.20	4.02	3.82	5.32	6.25	6.85	4.69	5.82	6.45	4.49	5.68	6.33	5.77
Gamma	G3	5.12	7.15	6.14	4.31	4.50	4.41	3.47	3.70	2.83	4.21	4.33	3.89	4.15	4.20	4.09	3.96	5.33	5.37	6.28	4.45	4.58	5.59	4.10	4.25	5.33	5.03
Gamma	G4	5.16	7.11	6.13	4.10	4.30	4.20	3.48	3.63	3.04	4.27	4.34	3.98	4.23	4.22	4.11	4.01	5.47	5.58	5.99	4.37	4.54	5.02	3.90	4.08	4.63	4.84
FIR	FIR3	4.01	5.67	4.84	6.58	6.48	6.53	1.87	2.70	2.01	3.25	3.89	3.15	3.75	4.06	3.58	3.14	7.98	7.27	7.51	7.45	6.66	6.94	7.31	6.49	6.77	7.15
FIR	FIR5	4.70	6.50	5.60	5.36	5.21	5.28	2.91	3.21	2.64	4.10	4.27	3.81	4.17	4.18	3.97	3.70	6.89	6.71	6.85	5.70	5.58	5.74	5.26	5.13	5.31	5.91
FIR	FIR7	5.25	6.76	6.00	4.19	4.43	4.31	3.02	3.15	2.62	4.26	4.29	3.90	4.18	4.20	4.08	3.74	6.98	6.98	7.10	5.42	5.46	5.60	4.75	4.81	4.97	5.78
FIR	FIR9	5.20	6.75	5.98	3.71	3.90	3.81	2.93	3.04	2.59	4.22	4.31	3.95	4.23	4.22	4.12	3.73	7.31	7.41	7.48	5.36	5.48	5.60	4.51	4.67	4.81	5.85
FIR	FIR20	4.96	6.57	5.77	0.99	0.82	0.91	2.14	2.22	1.92	3.93	4.12	3.70	4.20	4.20	4.10	3.39	10.17	10.13	10.22	6.93	6.90	7.00	5.33	5.38	5.46	7.50
B-spline	S3	3.87	5.99	4.93	6.45	5.76	6.10	2.10	3.00	2.39	3.42	4.05	3.37	3.82	4.12	3.63	3.32	7.68	6.89	6.99	7.10	6.24	6.35	6.93	6.02	6.13	6.70
B-spline	S5	5.39	7.03	6.21	4.33	4.30	4.31	3.24	3.49	2.84	4.28	4.33	3.89	4.21	4.22	4.04	3.84	6.12	6.11	6.46	4.80	4.84	5.26	4.29	4.32	4.80	5.22
B-spline	S7	5.31	6.86	6.09	3.91	3.90	3.90	3.23	3.39	2.86	4.26	4.34	4.03	4.14	4.18	4.11	3.84	6.47	6.47	6.66	4.77	4.79	5.03	4.02	4.06	4.34	5.18
B-spline	S9	5.27	6.81	6.04	3.61	3.56	3.58	3.18	3.26	2.78	4.26	4.32	4.05	4.24	4.24	4.16	3.83	6.98	6.99	7.12	4.95	4.96	5.12	4.02	4.07	4.25	5.39
Fourier	F1 (Co)	3.99	6.42	5.21	5.34	5.06	5.20	3.28	3.59	2.93	4.18	4.30	3.78	4.19	4.20	3.96	3.91	6.03	5.73	6.06	5.50	5.22	5.57	5.34	5.04	5.42	5.55
Fourier	F2	4.75	6.75	5.75	4.29	4.27	4.28	3.50	3.65	3.12	4.32	4.38	4.06	4.20	4.21	4.14	4.04	5.44	5.45	5.77	4.26	4.37	4.73	3.82	3.93	4.33	4.68
Fourier	F3	4.75	6.49	5.62	3.96	3.92	3.94	3.42	3.57	3.06	4.34	4.38	4.16	4.20	4.22	4.18	4.04	5.94	5.95	6.12	4.38	4.43	4.64	3.71	3.78	4.01	4.77
Fourier	F4	4.71	6.36	5.53	3.52	3.56	3.54	3.22	3.37	2.90	4.32	4.37	4.15	4.22	4.22	4.19	3.98	6.58	6.59	6.71	4.70	4.73	4.88	3.85	3.91	4.07	5.11
Fourier	F5	4.70	6.45	5.58	3.15	3.19	3.17	2.99	3.14	2.71	4.25	4.33	4.09	4.20	4.20	4.20	3.88	7.24	7.22	7.34	5.09	5.10	5.23	4.08	4.14	4.28	5.52
ICA	N/A	3.46	5.19	4.33	4.60	4.54	4.57	3.48	3.62	3.10	4.33	4.36	4.13	4.23	4.21	4.18	4.04	5.45	5.49	6.45	4.09	4.17	4.75	3.78	3.67	4.55	4.71

Worst — Performance of Each Metric — Best

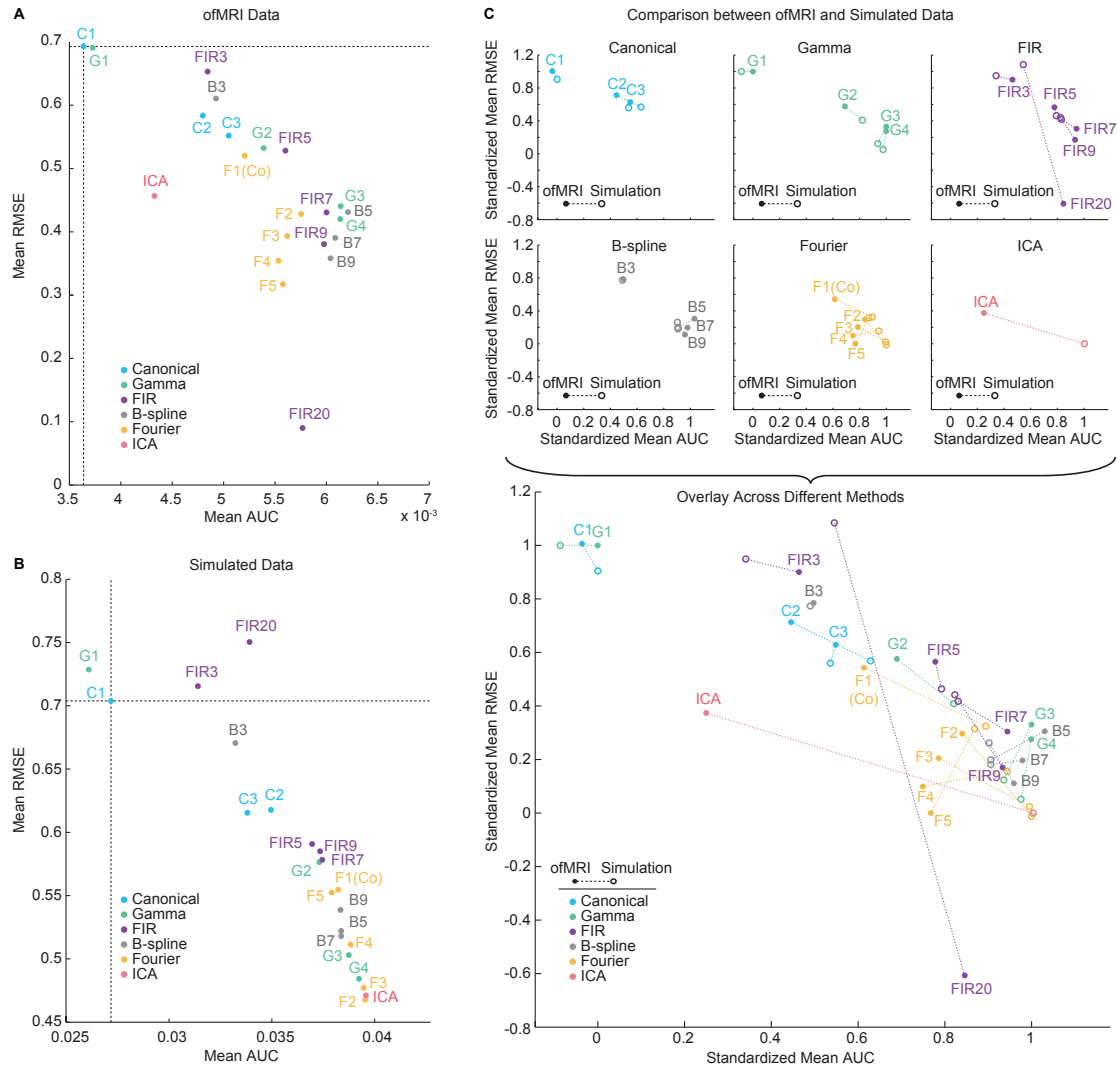Table 3.1: ***GLM with the 3rd and 4th order gamma basis sets, the 7th to 9th order FIR basis sets, the 5th to 9th order B-spline basis sets, and the 2nd to 5th order Fourier basis sets show superior detection and characterization performance over other methods.*** *Color bar represents the relative performance of different methods with each performance metric. Non-smoothed ofMRI data were used when calculating AUC and RMSE. To eliminate the influence of extreme values, the color scale was set based on the value of the second best performing method (red) and the second worst performing method (green) in each column. The best performing method exhibits the highest AUC and the smallest RMSE, and the worst performing method exhibits the lowest AUC and the largest RMSE. C1 to C3, G1 to G4, FIR3 to FIR20, B3 to B9, and F1 to F5 refer to different model orders in the canonical, gamma, FIR, B-spline, and Fourier basis sets. Co stands for coherence analysis.*

3.4 Discussion

The large number of existing analysis approaches necessitates a comprehensive assessment to ease the selection of methods in scenarios with heterogeneous BOLD responses, yet none have been performed thoroughly with a block-design paradigm. In the present work, we address this issue by systematically evaluating a series of standard analysis methods using rodent ofMRI data in Chapter 2 and simulations with a block-design paradigm. We find that, conventionally used GLM with a canonical basis set leads to considerable detection and characterization errors in the presence of heterogeneous BOLD responses. GLM with the 3rd and 4th order gamma basis sets, the 7th to 9th order FIR basis sets, the 5th to 9th order B-spline basis sets, and the 2nd to 5th order Fourier basis sets are the optimal methods as they offer good balance between detection and characterization. GLM with the 1st order Fourier basis set (coherence analysis) used in our earlier studies shows good detection capability. ICA shows good detection and characterization performance with the simulated data, but detects a large volume of spurious activations with the control ofMRI data.

Our study aims to evaluate the performance of various methods and strives to provide recommendations for method selection primarily in the analysis of animal fMRI data. In small animal fMRI studies, variations in the temporal dynamics of the hemodynamic responses can be more severe than those in human studies. This is likely due to the use of anesthesia to minimize motion and restraint stress [SSR15, SSS14, WMM10], the use of disease models [NHR04, WRJ08], and the use of direct brain stimulation [AKS09, BLL15, DCC15, FZL16, LWB16, LDG10, LLW15, WFL15] in small animal studies. Under these conditions, evoked BOLD responses can differ considerably from the canonical response. For example, in urethane-anesthetized mice, a 20 s electrical stimulation in the hind paw causes the fMRI responses in the thalamus to be delayed by approximately 11 s compared to the canonical response [SSS14]. In another study with isoflurane-anesthetized rats, optogenetic stimulation of the hippocampus for 20 s evokes BOLD responses that last for over 50 s [WFL15]. In such cases, employing the analysis approaches recommended in the present study may be beneficial to accurately detect and characterize these heterogeneous responses.

Notably, in animal ofMRI studies, analysis methods that can accurately detect and characterize evoked BOLD responses are particularly useful in the identification of stimulation-related artifacts. During ofMRI experiments, stray light and local tissue heating associated with the optical stimulation can introduce undesirable artifacts to the data [CWS13, SWA16], hence it is important to identify contaminated data during the analysis process. Specifically, artifacts caused by stray light are typically detected in vision-related brain regions [SWA16], whereas optogenetically-evoked responses are usually absent there when the stimulation target is outside of the visual pathway [BLL15, DKK11, DCC15, LWB16, LDG10, LLW15, TYK15, WFL15]. As a result, accurate detection of BOLD responses in vision-related regions is essential to identify data contaminated with these artifacts. Conversely, at the stimulation site, artifacts caused by local tissue heating usually exhibit both positive and negative fMRI signal changes [CWS13], whereas optogenetically-evoked responses usually show only one type of polarity [DCC15, LLL10, LLW15, TYK15, WFL15]. As a result, accurate characterization of BOLD responses at the stimulation site is critical to identify data contaminated with heating artifacts. In both cases, employing the methods that show good detection and characterization performance in the present study may be advantageous in the analysis process.

Beyond providing guidelines for animal studies, our results may also be useful for analyzing block-design fMRI data in human studies, especially those with highly variable responses. For example, in ischemic patients, a 24 s hand-grasping task causes the BOLD responses in the primary motor cortex to be delayed by up to 24 s compared to those in the cerebellum [AKS12]. In patients with major arterial stenosis, a 10 s handball squeeze task causes the BOLD responses in the primary motor cortex to be delayed by approximately 3 s compared to those in healthy individuals [RWA06]. Occasionally, heterogeneous BOLD responses can also be observed in healthy human subjects. For example, a 9 s painful mechanical stimuli causes the BOLD responses in the somatosensory cortex to persist for approximately 18 s [PLO09]. After averaging a large number of trials for each subject, a 20 s visual stimulation plus attention control task leads to highly variable BOLD responses throughout the brain [GSH12]. In such cases, adopting the methods recommended in the present work may also be useful to reduce errors in the detection and characterization tasks.

Notably, our results, which are based on rodent ofMRI data and simulated data guided by experimental data, are in good agreement with published data on human block-design studies. For example, GLM with the 1st order canonical basis set detected a smaller volume of hemodynamic responses compared to ICA in patients with fibromyalgia when painful stimuli were applied [PLO09]. In a like manner, during psychomotor tasks in healthy subjects, GLM with the 1st order canonical basis set did not uncover BOLD responses in the frontal regions that were detected by ICA [MMB98]. Consistently with our results, when the elicited BOLD responses were less heterogeneous during a simple visual paradigm in healthy subjects, GLM with the 1st order canonical basis set and ICA delivered comparable detection results [CAP01a].

Nonetheless, it should be noted that there exist several differences in regards to the characterization performed here compared to the commonly conducted ones in event-related studies. First, instead of characterizing impulse response functions, we focused on characterizing responses evoked by blocks of stimulation, which we refer to as block responses, although the impulse response function characterizations are more widely investigated [LLA09, SWT14]. While block-design studies are not optimal for modeling impulse response functions [MBG12], characterizing block responses can often offer great insights. For example, delayed occipital block responses during face encoding task may serve as an early marker for Alzheimer's disease in human [RGS05]. In rodent ofMRI studies, prolonged block responses could be indicative of seizure-like afterdischarge activities in the hippocampus [WFL15]. These variations in the block responses could originate from various sources including the timing of neuronal activity, the impulse response function, and nonlinearities. Nonetheless, accurate detection and characterization of these block response variations provide an important first step towards in-depth investigations of the underlying mechanism. Second, we did not impose constraints on the basis sets, although it is recommended when modeling impulse response functions in order to avoid physiologically ambiguous or implausible shapes [CSP04, STR10, WBS04]. This is because a larger degree of variations may be observed in block responses compared to impulse response functions. For example, impulse response functions are usually considered to be physiological meaningful if they only have one peak [CSP04], or exhibit a sensible range of time-to-peak values [HPR02]. However, because of the transient neuronal activities at block transitions (the beginning and end

of each task-block), physiological meaningful bimodal block responses have been observed in humans [MCD12]. Block responses from the ofMRI datasets used here also exhibit a wide range of onset shifts relative to the canonical response. Therefore, we did not impose constraints on the basis sets.

The present work demonstrates advantages of flexible models in achieving better detection and characterization performances, but the analysis results should be interpreted with caution. First, using flexible models may lead to the detection of physiologically implausible responses. To reduce such undesirable errors, it may be helpful to examine the temporal dynamics of detected BOLD responses in each region of interest. Special attention may be paid to unexpected activation and prior knowledge of anatomical and functional connectivity could be used to assess whether detected responses are physiologically plausible. Electrophysiological experiments, such as *in vivo* extracellular recordings, may also help to confirm the neural origin of detected responses. Second, the regression coefficients estimated with flexible models may lack interpretability, in contrast to conventionally used 1st order canonical basis set where the regression coefficient typically reflects the amplitude of the BOLD responses. For example, in the case of the Fourier basis set, it is difficult to interpret the regression coefficients of higher harmonics, as they only represent the refinement of model fitting, and are not interpretable features of the BOLD responses, such as amplitude, onset, and duration.

In this study, systematic evaluations of various statistical methods are presented, but a few caveats exist. First, the simulated data was generated by adding Gaussian noise to the ground truth signal, which did not account for any other type of physiological noise that may be present in the real data (e.g., colored noise). Adding physiological noise may affect the TPR, FPR, and AUC results [WR12]. Second, the simulated datasets did not include other types of BOLD responses, such as nonstationary or biphasic responses [FSB05, FSM05, GSH12, HM02, Ulu08]. Third, we evaluated a variety of analysis methods on their simultaneous detection and characterization capabilities, but it may be possible to achieve higher accuracies using advanced statistical methods, such as two-gamma-variate fitting [YHW16] and exponential fitting [BSD15]. Future comparisons including advanced methods may be useful. Fourth, it is worth noting that, there

106
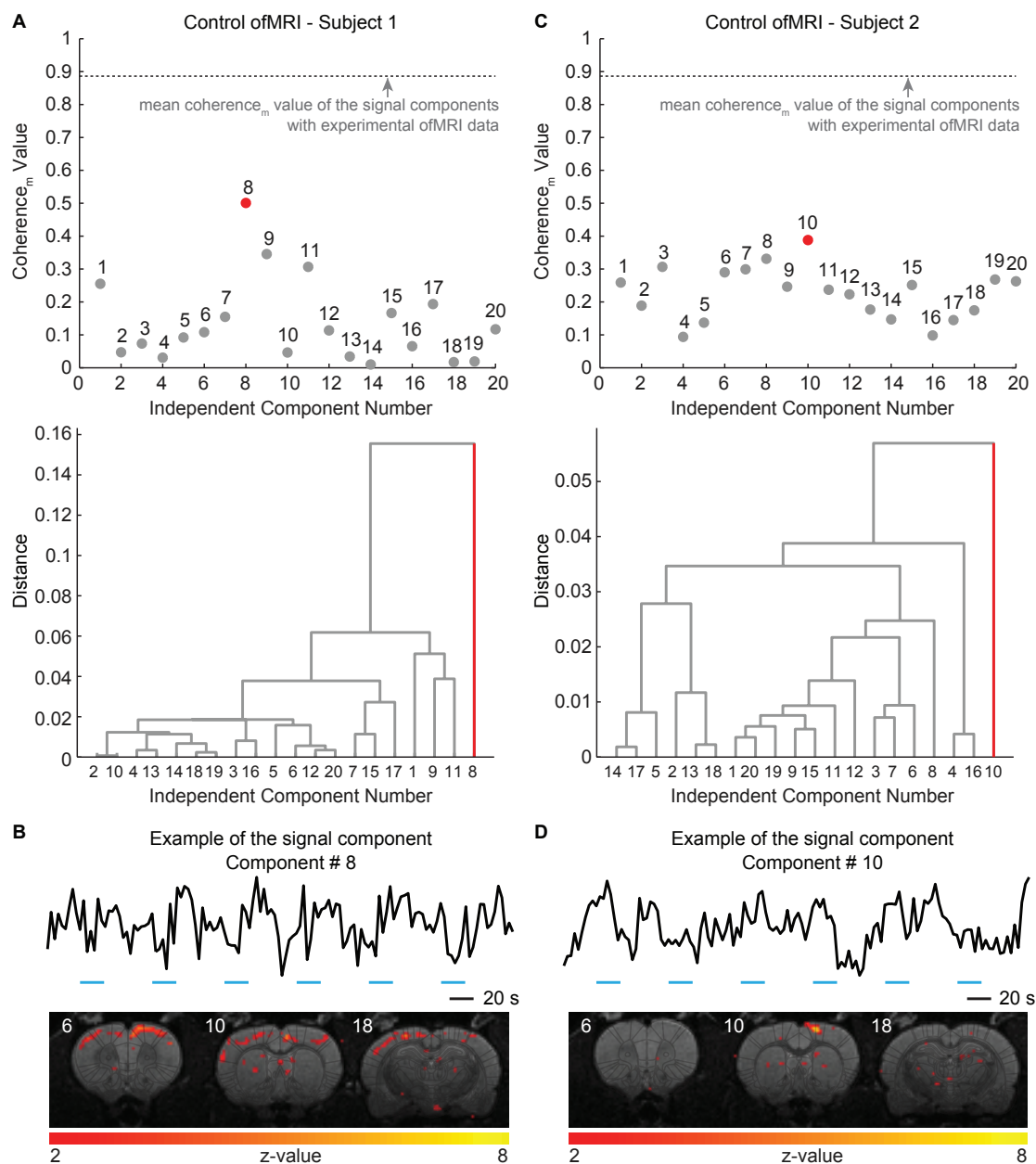
Figure 3.22: **The signal components in the control group exhibit much smaller coherence$_m$ values than the signal components in the experimental group.** *(A, C) Scatter plots show coherence$_m$ value (top panel) and dendrogram (bottom panel) of each extracted independent component from subjects in the control group (N = 2 subjects). The number of independent components in each subject was set to 20. The dashed horizontal line represents the mean coherence$_m$ value of the signal components across different experimental subjects and stimulation frequencies. (B, D) The time courses and the spatial maps associated with the signal components in the control group are shown. Threshold was set at |Z| > 2 for the spatial map. Horizontal blue bars represent the 20 s period of optical stimulation.*

exist many metrics to compare methods besides those employed in the present work. Among the commonly used ones are the Akaike Information Criterion [Aka98], the Bayesian Information Criterion [Sch78], and the Bayesian model selection [Was00]. In this work, we focused on two specific applications of fMRI analysis – detection and characterization of the BOLD responses – utilizing application-specific performance metrics, such as AUC for detection and RMSE of fit for characterization. Fifth, the method employed to select signal components assumes the existence of signals of interest in the datasets. However, if used on data without signals of interest, such as the control ofMRI data, this method would yield a group of 'signal' components that are predominantly noise (Figure 3.22). Employing such 'signal' components during data analysis may lead to undesirable consequences, such as the detection of spurious activations. With the purpose of comparing the performance against other methods, we employed these 'signal' components from the control ofMRI data. However, when using ICA for data analysis, time series and spatial maps of the selected signal components should be inspected prior to further analysis to avoid erroneous detections. Finally, the present study mainly focused on periodic block designs, and may not directly apply to non-periodic block-design studies. For example, our signal component selection method assumes that the signal of interest is periodic with respect to time. Therefore, this method is not suitable to extract signal components from data with a non-periodic paradigm. Additionally, the sinusoidal functions in the Fourier basis set was used to model BOLD responses over the entire scan session. In this case, their fundamental frequency was set to the frequency of repeated stimulation cycles, which would only apply to studies with periodic designs. Nonetheless, the Fourier basis set may be used for non-periodic block-design studies if it is used to model the impulse response function instead. In this case, the sinusoidal functions may need to be convolved with the stimulation paradigm before being used as regressors. For example, the Fourier basis set was used to model impulse responses in epilepsy patients and successfully detected activations that may be indicative of propagated epileptiform activity [LLC08]. Therefore, further evaluations may be necessary to understand each method's detection and characterization capabilities in non-periodic block-design studies.

CHAPTER 4

Conclusions

Since its debut in 2010, ofMRI has been increasingly employed in various research areas, such as the investigation of BOLD mechanisms [KDK11, KKD13, CWS13, LZT14, IVP15], and mapping the functional network of cortico-thalamic pathways [LDG10], primary somatosensory cortex [DKK11], medial prefrontal cortex [LWA15, FZL16], and hippocampus [WSG11, AST12, WFL15, DCC15, LHW15, TYK15]. This thesis describes a study that employs ofMRI to investigate and visualize the whole-brain network controlled by central thalamus, and discusses the appropriate approaches in the analysis of ofMRI datasets with heterogeneous BOLD responses.

In Chapter 2, the role of central thalamus in forebrain arousal is investigated at different stimulation paradigms using ofMRI. High frequency stimulation, such as 40 Hz and 100 Hz, leads to behavior arousal and wide-spread activations in cortical and subcortical brain regions. Conversely, low frequency stimulation, such as 10 Hz, results in behavior arrest and cortical inhibition. The role of zona incerta in the mediation of cortical excitation/inhibition balance is also uncovered.

In Chapter 3, a comprehensive evaluation of six standard analysis methods is conducted to understand the proper choice of methods against heterogeneous BOLD responses in ofMRI studies. The results show that, GLM with the 3rd and 4th order gamma basis sets, the 7th to 9th order FIR basis sets, the 5th to 9th order B-spline basis sets, and the 2nd to 5th order Fourier basis sets are optimal for good balance between detection and characterization, while the 1st order Fourier basis set (coherence analysis) used in our earlier studies show good detection capability. ICA has mostly good detection and characterization capabilities, but detects a large volume of spurious activation with the control fMRI data.

As a newly developed technique, ofMRI has a lot of potentials that await future researchers to explore. Every element in the ofMRI experiments, such as the choice of light-sensitive proteins, stimulation paradigm, and experimental design, can be customized to best test the scientific hypothesis of interest. This thesis provides an example of such studies and offers practical recommendations for analyzing ofMRI datasets with heterogeneous hemodynamic responses.

References

[ABC08]   John Ashburner, Gareth Barnes, C Chen, Jean Daunizeau, Guillaume Flandin, Karl Friston, D Gitelman, S Kiebel, J Kilner, V Litvak, et al. "Face Group fMRI Data." *SPM8 Manual*, pp. 261–280, 2008.

[AC91]   A Agmon and BW Connors. "Thalamocortical responses of mouse somatosensory (barrel) cortexin vitro." *Neuroscience*, **41**(2):365–379, 1991.

[Aka98]   Hirotogu Akaike. "Information theory and an extension of the maximum likelihood principle." In *Selected Papers of Hirotugu Akaike*, pp. 199–213. Springer, 1998.

[AKS09]   Frank Angenstein, Elena Kammerer, and Henning Scheich. "The BOLD response in the rat hippocampus depends rather on local processing of signals than on the input or output activity. A combined functional MRI and electrophysiological study." *The Journal of Neuroscience*, **29**(8):2428–2439, 2009.

[AKS12]   Shiori Amemiya, Akira Kunimatsu, Nobuhito Saito, and Kuni Ohtomo. "Impaired hemodynamic response in the ischemic brain assessed with BOLD fMRI." *Neuroimage*, **61**(3):579–590, 2012.

[ALC15]   Oluwaseun Akeju, Marco L Loggia, Ciprian Catana, Kara J Pavone, Rafael Vazquez, James Rhee, Violeta Contreras Ramirez, Daniel B Chonde, David Izquierdo-Garcia, Grae Arabasz, et al. "Disruption of thalamic functional connectivity is a neural correlate of dexmedetomidine-induced unconsciousness." *eLife*, **3**:e04499, 2015.

[APD07]   Elena A Allen, Brian N Pasley, Thang Duong, and Ralph D Freeman. "Transcranial magnetic stimulation elicits coupled neural and hemodynamic consequences." *Science*, **317**(5846):1918–1921, 2007.

[AST12]   Yoshifumi Abe, Masaki Sekino, Yasushi Terazono, Hiroyuki Ohsaki, Yugo Fukazawa, Seiichiro Sakai, Hiromu Yawo, and Tatsuhiro Hisatsune. "Opto-fMRI analysis for exploring the neuronal connectivity of the hippocampal formation in rats." *Neuroscience research*, **74**(3):248–255, 2012.

[AWZ07]   Alexander M Aravanis, Li-Ping Wang, Feng Zhang, Leslie A Meltzer, Murtaza Z Mogri, M Bret Schneider, and Karl Deisseroth. "An optical neural interface: in vivo control of rodent motor cortex with integrated fiberoptic and optogenetic technology." *Journal of neural engineering*, **4**(3):S143, 2007.

[AZD98]   GK Aguirre, E Zarahn, and M D'esposito. "The variability of human, BOLD hemodynamic responses." *Neuroimage*, **8**(4):360–369, 1998.

[BBS96]   W Backfrieder, R Baumgartner, M Samal, E Moser, and H Bergmann. "Quantification of intensity variations in functional MR images using rotated principal components." *Physics in Medicine and Biology*, **41**(8):1425, 1996.

[BBW96] Edward Bullmore, Michael Brammer, Steve CR Williams, Sophia Rabe-Hesketh, Nicolas Janot, Anthony David, John Mellers, Robert Howard, and Pak Sham. "Statistical methods of estimation and inference for functional MR image analysis." *Magnetic Resonance in Medicine*, **35**(2):261–277, 1996.

[BFA02] P Bartho, TF Freund, and L Acsady. "Selective GABAergic innervation of thalamic nuclei from zona incerta." *European Journal of Neuroscience*, **16**(6):999–1014, 2002.

[BG90] Henk W Berendse and Henk J Groenewegen. "Organization of the thalamostriatal projections in the rat, with special emphasis on the ventral striatum." *Journal of Comparative Neurology*, **299**(2):187–228, 1990.

[BGK09] Christian Bamann, Ronnie Gueta, Sonja Kleinlogel, Georg Nagel, and Ernst Bamberg. "Structural guidance of the photocycle of channelrhodopsin-2 by an interhelical hydrogen bond." *Biochemistry*, **49**(2):267–278, 2009.

[BH95] Yoav Benjamini and Yosef Hochberg. "Controlling the false discovery rate: a practical and powerful approach to multiple testing." *Journal of the Royal Statistical Society. Series B (Methodological)*, pp. 289–300, 1995.

[BIG92] DL Benson, PJ Isackson, CM Gall, and EG Jones. "Contrasting patterns in the localization of glutamic acid decarboxylase and Ca 2+/calmodulin protein kinase gene expression in the rat centrat nervous system." *Neuroscience*, **46**(4):825–849, 1992.

[BJW93] Peter A Bandettini, Andrzej Jesmanowicz, Eric C Wong, James S Hyde, et al. "Processing strategies for time-course data sets in functional MRI of the human brain." *Magnetic resonance in medicine*, **30**(2):161–173, 1993.

[BLL15] Blake Byers, Hyun Joo Lee, Jia Liu, Andrew J Weitz, Peter Lin, Pengbo Zhang, Aleksandr Shcheglovitov, Ricardo Dolmetsch, Renee Reijo Pera, and Jin Hyung Lee. "Direct in vivo assessment of human stem cell graft–host neural circuits." *NeuroImage*, **114**:328–337, 2015.

[BLR14] Andre Berndt, Soo Yeun Lee, Charu Ramakrishnan, and Karl Deisseroth. "Structure-guided transformation of channelrhodopsin into a light-activated chloride channel." *Science*, **344**(6182):420–424, 2014.

[BMG96] Claudio Bassetti, Johannes Marhis, Matthias Gugger, Karl O Lovblad, and Christian W Hess. "Hypersomnia following paramedian thalamic stroke: a report of 12 patients." *Annals of neurology*, **39**(4):471–480, 1996.

[BS95] Anthony J Bell and Terrence J Sejnowski. "An information-maximization approach to blind separation and blind deconvolution." *Neural computation*, **7**(6):1129–1159, 1995.

[BS04]   Christian F Beckmann and Stephen M Smith. "Probabilistic independent compo-
            nent analysis for functional magnetic resonance imaging." *Medical Imaging, IEEE
            Transactions on*, **23**(2):137–152, 2004.

[BSD15]   Simone C Bosshard, Florian Stuker, Constantin von Deuster, Aileen Schroeter, and
            Markus Rudin. "BOLD fMRI of C-fiber mediated nociceptive processing in mouse
            brain in response to thermal stimulation of the forepaws." *PloS one*, **10**(5):e0126513,
            2015.

[BSM11]   André Berndt, Philipp Schoenenberger, Joanna Mattis, Kay M Tye, Karl Deisseroth,
            Peter Hegemann, and Thomas G Oertner. "High-efficiency channelrhodopsins for
            fast neuronal stimulation at low light levels." *Proceedings of the National Academy
            of Sciences*, **108**(18):7595–7600, 2011.

[BSS00]   R Baumgartner, R Somorjai, R Summers, W Richter, L Ryner, and M Jarmasz. "Re-
            sampling as a cluster validation technique in fMRI." *Journal of Magnetic Resonance
            Imaging*, **11**(2):228–231, 2000.

[BYG09]   André Berndt, Ofer Yizhar, Lisa A Gunaydin, Peter Hegemann, and Karl Deisseroth.
            "Bi-stable neural state switches." *Nature neuroscience*, **12**(2):229–234, 2009.

[BZB05]   Edward S Boyden, Feng Zhang, Ernst Bamberg, Georg Nagel, and Karl Deisseroth.
            "Millisecond-timescale, genetically targeted optical control of neural activity." *Na-
            ture neuroscience*, **8**(9):1263–1268, 2005.

[CAP01a]   VD Calhoun, T Adali, GD Pearlson, and JJ Pekar. "A method for making group in-
            ferences from functional MRI data using independent component analysis." *Human
            brain mapping*, **14**(3):140–151, 2001.

[CAP01b]   VD Calhoun, T Adali, GD Pearlson, and JJ Pekar. "Spatial and temporal indepen-
            dent component analysis of functional MRI data containing a pair of task-related
            waveforms." *Human brain mapping*, **13**(1):43–53, 2001.

[CAS12]   Scott J Cruikshank, Omar J Ahmed, Tanya R Stevens, Saundra L Patrick, Amalia N
            Gonzalez, Margot Elmaleh, and Barry W Connors. "Thalamic control of layer 1
            circuits in prefrontal cortex." *The Journal of Neuroscience*, **32**(49):17813–17823,
            2012.

[CC96a]   Manuel A Castro-Alamancos and Barry W Connors. "Cellular mechanisms of the
            augmenting response: short-term plasticity in a thalamocortical pathway." *The Jour-
            nal of neuroscience*, **16**(23):7742–7756, 1996.

[CC96b]   Manuel A Castro-Alamancos and Barry W Connors. "Short-term plasticity of
            a thalamocortical pathway dynamically modulated by behavioral state." *Science*,
            272(5259):274–277, 1996.

[CC96c]   Manuel A Castro-Alamancos and Barry W Connors. "Spatiotemporal properties of
            short-term plasticity sensorimotor thalamocortical pathways of the rat." *The Journal
            of neuroscience*, **16**(8):2767–2779, 1996.

[CC97]   MANUEL A CASTRO-ALAMANCOS and BARRY W CONNORS. "Thalamocortical synapses." *Progress in neurobiology*, **51**(6):581–606, 1997.

[CCL99]   Kai-Hsiang Chuang, Ming-Jang Chiu, Chung-Chih Lin, and Jyh-Horng Chen. "Model-free functional MRI analysis using Kohonen clustering neural network and fuzzy C-means." *Medical Imaging, IEEE Transactions on*, **18**(12):1117–1128, 1999.

[CDS97]   Diego Contreras, Alain Destexhe, Terrence J Sejnowski, and Mircea Steriade. "Spatiotemporal patterns of spindle oscillations in cortex and thalamus." *The Journal of neuroscience*, **17**(3):1179–1196, 1997.

[CLB81]   P Castaigne, F Lhermitte, A Buge, R Escourolle, JJ Hauw, and O Lyon-Caen. "Paramedian thalamic and midbrain infarcts: clinical and neuropathological study." *Annals of neurology*, **10**(2):127–148, 1981.

[CLC07]   Scott J Cruikshank, Timothy J Lewis, and Barry W Connors. "Synaptic basis for intense thalamocortical activation of feedforward inhibitory cells in neocortex." *Nature neuroscience*, **10**(4):462–468, 2007.

[Cox96]   Robert W Cox. "AFNI: software for analysis and visualization of functional magnetic resonance neuroimages." *Computers and Biomedical research*, **29**(3):162–173, 1996.

[CSP04]   VD Calhoun, MC Stevens, GD Pearlson, and KA Kiehl. "fMRI analysis with the general linear model: removal of latency-induced amplitude bias by incorporation of hemodynamic derivative terms." *Neuroimage*, **22**(1):252–257, 2004.

[CWS13]   Isabel N Christie, Jack A Wells, Paul Southern, Nephtali Marina, Sergey Kasparov, Alexander V Gourine, and Mark F Lythgoe. "fMRI response to blue light delivery in the naive brain: implications for combined optogenetic fMRI studies." *Neuroimage*, **66**:634–641, 2013.

[DBP96]   M Deschenes, J Bourassa, and A Parent. "Striatal and cortical projections of single neurons from the central lateral thalamic nucleus in the rat." *Neuroscience*, **72**(3):679–687, 1996.

[DCC15]   Ben A Duffy, ManKin Choy, Miguel R Chuapoco, Michael Madsen, and Jin Hyung Lee. "MRI compatible optrodes for simultaneous LFP and optogenetic fMRI investigation of seizure-like afterdischarges." *NeuroImage*, **123**:173–184, 2015.

[DDA97]   Mark D'Esposito, John A Detre, Geoffrey K Aguirre, Matthew Stallcup, David C Alsop, Lynette J Tippet, and Martha J Farah. "A functional MRI study of mental image generation." *Neuropsychologia*, **35**(5):725–730, 1997.

[DKK11]   Mitul Desai, Itamar Kahn, Ulf Knoblich, Jacob Bernstein, Hisham Atallah, Aimei Yang, Nancy Kopell, Randy L Buckner, Ann M Graybiel, Christopher I Moore, et al. "Mapping brain networks in awake mice using combined optical neural control and fMRI." *Journal of neurophysiology*, **105**(3):1393–1405, 2011.

[DL14]   David Degras and Martin A Lindquist. "A hierarchical model for simultaneous detection and estimation in multi-subject fMRI studies." *NeuroImage*, **98**:61–72, 2014.

[DM43]   EW Dempsey and RS Morison. "The electrical activity of a thalamocortical relay system." *American Journal of Physiology–Legacy Content*, **138**(2):283–296, 1943.

[DTN07]   Anna Devor, Peifang Tian, Nozomi Nishimura, Ivan C Teng, Elizabeth MC Hillman, SN Narayanan, Istvan Ulbert, David A Boas, David Kleinfeld, and Anders M Dale. "Suppressed neuronal activity and concurrent arteriolar vasoconstriction may explain negative blood oxygenation level-dependent signal." *The Journal of Neuroscience*, **27**(16):4452–4459, 2007.

[EAJ12]   Anders Eklund, Mats Andersson, Camilla Josephson, Magnus Johannesson, and Hans Knutsson. "Does parametric fMRI analysis with SPM yield valid results? – An empirical study of 1484 rest datasets." *NeuroImage*, **61**(3):565–578, 2012.

[EFS02]   Fabrizio Esposito, Elia Formisano, Erich Seifritz, Rainer Goebel, Renato Morrone, Gioacchino Tedeschi, and Francesco Di Salle. "Spatial independent component analysis of functional MRI time-series: To what extent do results depend on the algorithm used?" *Human brain mapping*, **16**(3):146–157, 2002.

[EGW97]   Stephen A Engel, Gary H Glover, and Brian A Wandell. "Retinotopic organization in human visual cortex and the spatial precision of functional MRI." *Cerebral cortex*, **7**(2):181–192, 1997.

[EHK13]   TJ Ellender, J Harwood, P Kosillo, M Capogna, and JP Bolam. "Heterogeneous properties of central lateral and parafascicular thalamic synapses in the striatum." *The Journal of physiology*, **591**(1):257–272, 2013.

[Eks10]   Arne Ekstrom. "How and when the fMRI BOLD signal relates to underlying neural activity: the danger in dissociation." *Brain research reviews*, **62**(2):233–244, 2010.

[ENK16]   Anders Eklund, Thomas E Nichols, and Hans Knutsson. "Cluster failure: Why fMRI inferences for spatial extent have inflated false-positive rates." *Proceedings of the National Academy of Sciences*, p. 201602413, 2016.

[ERB11]   Erik Barry Erhardt, Srinivas Rachakonda, Edward J Bedrick, Elena A Allen, Tülay Adali, and Vince D Calhoun. "Comparison of multi-subject ICA methods for analysis of fMRI data." *Human brain mapping*, **32**(12):2075–2095, 2011.

[ESH05]   Fabrizio Esposito, Tommaso Scarabino, Aapo Hyvarinen, Johan Himberg, Elia Formisano, Silvia Comani, Gioacchino Tedeschi, Rainer Goebel, Erich Seifritz, and Francesco Di Salle. "Independent component analysis of fMRI group studies by self-organizing clustering." *Neuroimage*, **25**(1):193–205, 2005.

[FBB14]   Esteban A Fridman, Bradley J Beattie, Allegra Broft, Steven Laureys, and Nicholas D Schiff. "Regional cerebral metabolic patterns demonstrate the role of anterior forebrain mesocircuit dysfunction in the severely injured brain." *Proceedings of the National Academy of Sciences*, **111**(17):6473–6478, 2014.

[FFJ98]   Karl J Friston, P Fletcher, Oliver Josephs, A Holmes, MD Rugg, and Robert Turner. "Event-related fMRI: characterizing differential responses." *Neuroimage*, **7**(1):30–40, 1998.

[FHW94]   Karl J Friston, Andrew P Holmes, Keith J Worsley, J-P Poline, Chris D Frith, and Richard SJ Frackowiak. "Statistical parametric maps in functional imaging: a general linear approach." *Human brain mapping*, **2**(4):189–210, 1994.

[FL13]   Zhongnan Fang and Jin Hyung Lee. "High-throughput optogenetic functional magnetic resonance imaging with parallel computations." *Journal of neuroscience methods*, **218**(2):184–195, 2013.

[FSB05]   Michael D Fox, Abraham Z Snyder, Deanna M Barch, Debra A Gusnard, and Marcus E Raichle. "Transient BOLD responses at block transitions." *Neuroimage*, **28**(4):956–966, 2005.

[FSM05]   Michael D Fox, Abraham Z Snyder, Mark P McAvoy, Deanna M Barch, and Marcus E Raichle. "The BOLD onset transient: identification of novel functional differences in schizophrenia." *Neuroimage*, **25**(3):771–782, 2005.

[Fur58]   Joaquin M Furster. "Effects of stimulation of brain stem on tachistoscopic perception." *Science*, **127**:150, 1958.

[FZL16]   Emily A Ferenczi, Kelly A Zalocusky, Conor Liston, Logan Grosenick, Melissa R Warden, Debha Amatya, Kiefer Katovich, Hershel Mehta, Brian Patenaude, Charu Ramakrishnan, et al. "Prefrontal cortical regulation of brainwide circuit dynamics and reward-related behavior." *Science*, **351**(6268):aac9698, 2016.

[GB94]   Henk J Groenewegen and Henk W Berendse. "The specificity of the 'nonspecific' midline and intralaminar thalamic nuclei." *Trends in neurosciences*, **17**(2):52–57, 1994.

[GDP15]   Kristóf Giber, Marco A Diana, Viktor M Plattner, Guillaume P Dugué, Hajnalka Bokor, Charly V Rousseau, Zsófia Maglóczky, László Havas, Balázs Hangya, Hendrik Wildner, et al. "A subcortical inhibitory signal for behavioral arrest in the thalamus." *Nature neuroscience*, **18**(4):562–568, 2015.

[Gen00]   Christopher R Genovese. "A Bayesian time-course model for functional magnetic resonance imaging data." *Journal of the American Statistical Association*, **95**(451):691–703, 2000.

[GHM05]   Sten Grillner, Jeanette Hellgren, Ariane Menard, Kazuya Saitoh, and Martin A Wikström. "Mechanisms for selection of basic motor programs–roles for the striatum and pallidum." *Trends in neurosciences*, **28**(7):364–370, 2005.

[GHR09]   Zengcai V Guo, Anne C Hart, and Sharad Ramanathan. "Optical interrogation of neural circuits in Caenorhabditis elegans." *Nature methods*, **6**(12):891–896, 2009.

[GK09]   Valeria Gazzola and Christian Keysers. "The observation and execution of actions share motor and somatosensory voxels in all tested subjects: single-subject analyses of unsmoothed fMRI data." *Cerebral Cortex*, **19**(6):1239–1255, 2009.

[GL95]   Gary H Glover and Adrian T Lee. "Motion artifacts in fMRI: comparison of 2DFT with PR and spiral scan methods." *Magnetic Resonance in Medicine*, **33**(5):624–635, 1995.

[GLA00]   Anne-Lise Giraud, Christian Lorenzi, John Ashburner, Jocelyne Wable, Ingrid Johnsrude, Richard Frackowiak, and Andreas Kleinschmidt. "Representation of the temporal envelope of sounds in the human brain." *Journal of Neurophysiology*, **84**(3):1588–1598, 2000.

[GLN02]   Christopher R Genovese, Nicole A Lazar, and Thomas Nichols. "Thresholding of statistical maps in functional neuroimaging using the false discovery rate." *Neuroimage*, **15**(4):870–878, 2002.

[GMS15]   Abhijeet Gummadavelli, Joshua E Motelow, Nicholas Smith, Qiong Zhan, Nicholas D Schiff, and Hal Blumenfeld. "Thalamic stimulation to improve level of consciousness after seizures: Evaluation of electrophysiology and behavior." *Epilepsia*, **56**(1):114–124, 2015.

[GS83]   Alan Guberman and Donald Stuss. "The syndrome of bilateral paramedian thalamic infarction." *Neurology*, **33**(5):540–540, 1983.

[GSH12]   Javier Gonzalez-Castillo, Ziad S Saad, Daniel A Handwerker, Souheil J Inati, Noah Brenowitz, and Peter A Bandettini. "Whole-brain, time-locked activation with simple tasks revealed using massive averaging and model-free analysis." *Proceedings of the National Academy of Sciences*, **109**(14):5487–5492, 2012.

[GTZ07]   Viviana Gradinaru, Kimberly R Thompson, Feng Zhang, Murtaza Mogri, Kenneth Kay, M Bret Schneider, and Karl Deisseroth. "Targeting and readout strategies for fast optical neural control in vitro and in vivo." *The Journal of neuroscience*, **27**(52):14231–14238, 2007.

[GYB10]   Lisa A Gunaydin, Ofer Yizhar, André Berndt, Vikaas S Sohal, Karl Deisseroth, and Peter Hegemann. "Ultrafast optogenetic control." *Nature neuroscience*, **13**(3):387–392, 2010.

[GZR10]   Viviana Gradinaru, Feng Zhang, Charu Ramakrishnan, Joanna Mattis, Rohit Prakash, Ilka Diester, Inbal Goshen, Kimberly R Thompson, and Karl Deisseroth. "Molecular and cellular approaches for diversifying and extending optogenetics." *Cell*, **141**(1):154–165, 2010.

[HC10]   Akio Hirata and Manuel A Castro-Alamancos. "Neocortex network activation and deactivation states controlled by the thalamus." *Journal of neurophysiology*, **103**(3):1147–1157, 2010.

[HFP03]   Michael D Hunter, Tom FD Farrow, Nikos G Papadakis, Iain D Wilkinson, Peter WR Woodruff, and Sean A Spence. "Approaching an ecologically valid functional anatomy of spontaneous "willed" action." *Neuroimage*, **20**(2):1264–1269, 2003.

[HGD12]   Daniel A Handwerker, Javier Gonzalez-Castillo, Mark D'Esposito, and Peter A Bandettini. "The continuing challenge of understanding and modeling hemodynamic variation in fMRI." *Neuroimage*, **62**(2):1017–1023, 2012.

[HGM92]   Stephan Heckers, Changiz Geula, and Marek-Marsel Mesulam. "Cholinergic innervation of the human thalamus: dual origin and differential nuclear distribution." *Journal of Comparative Neurology*, **325**(1):68–82, 1992.

[HGP08]   Joanna K Huttunen, Olli Gröhn, and Markku Penttonen. "Coupling between simultaneously recorded BOLD response and neuronal activity in the rat somatosensory cortex." *Neuroimage*, **39**(2):775–785, 2008.

[HJ49]   John Hunter and Herbert H Jasper. "Effects of thalamic stimulation in unanaesthetised animals: The arrest reaction and petit Mal-like seizures, activation patterns and generalized convulsions." *Electroencephalography and clinical neurophysiology*, **1**(1):305–324, 1949.

[HLK14]   Barbara J Hunnicutt, Brian R Long, Deniz Kusefoglu, Katrina J Gertz, Haining Zhong, and Tianyi Mao. "A comprehensive thalamocortical projection map at the mesoscopic level." *Nature neuroscience*, **17**(9):1276–1285, 2014.

[HM02]   Michael P Harms and Jennifer R Melcher. "Sound repetition rate in the human auditory pathway: representations in the waveshape and amplitude of fMRI activation." *Journal of Neurophysiology*, **88**(3):1433–1450, 2002.

[HM03]   Michael P Harms and Jennifer R Melcher. "Detection and quantification of a wide range of fMRI temporal responses using a physiologically-motivated basis set." *Human brain mapping*, **20**(3):168–183, 2003.

[HOD04]   Daniel A Handwerker, John M Ollinger, and Mark D'Esposito. "Variation of BOLD hemodynamic responses across subjects and brain regions and their effects on statistical analyses." *Neuroimage*, **21**(4):1639–1651, 2004.

[HPR02]   RNA Henson, Cathy J Price, MD Rugg, Robert Turner, and Karl J Friston. "Detecting latency differences in event-related BOLD responses: application to words versus nonwords and initial versus repeated face presentations." *Neuroimage*, **15**(1):83–97, 2002.

[HSO03]   RICHARD L Horner, R Stephenson, and CP O'Donnell. "Instrumentation and methods for chronic studies of sleep and breathing in rodents." In *Sleep Related Breathing Disorders: Experimental Models and Therapeutic Potential*, volume 171, pp. 19–55. Marcel Dekker, Inc, 2003.

[HV07]   Walter B Hoover and Robert P Vertes. "Anatomical analysis of afferent projections to the medial prefrontal cortex in the rat." *Brain Structure and Function*, **212**(2):149–179, 2007.

[HYL05]   Dewen Hu, Lirong Yan, Yadong Liu, Zongtan Zhou, Karl J Friston, Changlian Tan, and Daxing Wu. "Unified SPM–ICA for fMRI analysis." *Neuroimage*, **25**(3):746–755, 2005.

[IVP15]   Bistra Iordanova, Alberto L Vazquez, Alexander J Poplawsky, Mitsuhiro Fukuda, and Seong-Gi Kim. "Neural and hemodynamic responses to optogenetic and sensory stimulation in the rat somatosensory cortex." *Journal of Cerebral Blood Flow & Metabolism*, **35**(6):922–932, 2015.

[Jas49]   Herbert Jasper. "Diffuse projection systems: the integrative action of the thalamic reticular system." *Electroencephalography and clinical neurophysiology*, **1**(1):405–420, 1949.

[JL74]   EG t Jones and Randi Y Leavitt. "Retrograde axonal transport and the demonstration of non-specific projections to the cerebral cortex and striatum from thalamic intralaminar nuclei in the rat, cat and monkey." *Journal of Comparative Neurology*, **154**(4):349–377, 1974.

[JMN91]   John Jackson, Craig H Meyer, Dwight G Nishimura, Albert Macovski, et al. "Selection of a convolution function for Fourier inversion using gridding [computerised tomography application]." *Medical Imaging, IEEE Transactions on*, **10**(3):473–478, 1991.

[Joh67]   Stephen C Johnson. "Hierarchical clustering schemes." *Psychometrika*, **32**(3):241–254, 1967.

[Jon01]   Edward G Jones. "The thalamic matrix and thalamocortical synchrony." *Trends in neurosciences*, **24**(10):595–601, 2001.

[KAS03]   Dong-hyun Kim, Elfar Adalsteinsson, and Daniel M Spielman. "Simple analytic variable density spiral design." *Magnetic resonance in medicine*, **50**(1):214–219, 2003.

[KDK11]   Itamar Kahn, Mitul Desai, Ulf Knoblich, Jacob Bernstein, Michael Henninger, Ann M Graybiel, Edward S Boyden, Randy L Buckner, and Christopher I Moore. "Characterization of the functional MRI response temporal linearity via optical control of neocortical pyramidal neurons." *The Journal of Neuroscience*, **31**(42):15086–15091, 2011.

[KKD13]   I Kahn, U Knoblich, M Desai, J Bernstein, AM Graybiel, ES Boyden, RL Buckner, and CI Moore. "Optogenetic drive of neocortical pyramidal neurons generates fMRI signals that are correlated with spiking activity." *Brain research*, **1511**:33–45, 2013.

[KLG96]   Shigeo Kinomura, Jonas Larsson, Balazs Gulyas, and Per E Roland. "Activation by attention of the human reticular formation and thalamic intralaminar nuclei." *Science*, **271**(5248):512–515, 1996.

[KM99]   Christian Kolmac and J Mitrofanis. "Distribution of various neurochemicals within the zona incerta: an immunocytochemical and histochemical study." *Anatomy and embryology*, **199**(3):265–280, 1999.

[KMJ13]   Tae-il Kim, Jordan G McCall, Yei Hwan Jung, Xian Huang, Edward R Siuda, Yuhang Li, Jizhou Song, Young Min Song, Hsuan An Pao, Rak-Hwan Kim, et al. "Injectable, cellular-scale optoelectronics with applications for wireless optogenetics." *Science*, **340**(6129):211–216, 2013.

[LAM10]   Nikos K Logothetis, Mark Augath, Yusuke Murayama, Alexander Rauch, Fahad Sultan, Jozien Goense, Axel Oeltermann, and Hellmut Merkle. "The effects of electrical microstimulation on cortical signal propagation." *Nature neuroscience*, **13**(10):1283–1291, 2010.

[LDB16]   Jia Liu, Ben A Duffy, David Bernal-Casas, Zhongnan Fang, and Jin Hyung Lee. "Comparison of fMRI analysis methods for heterogeneous BOLD responses in block design studies." *Neuroimage*, **Under Review**, 2016.

[LDG10]   Jin Hyung Lee, Remy Durand, Viviana Gradinaru, Feng Zhang, Inbal Goshen, Dae-Shik Kim, Lief E Fenno, Charu Ramakrishnan, and Karl Deisseroth. "Global and local fMRI signals driven by neurons defined optogenetically by type and wiring." *Nature*, **465**(7299):788–792, 2010.

[LHW15]   Philipp Lebhardt, Christian Clemm von Hohenberg, Wolfgang Weber-Fahr, Wolfgang Kelsch, and Alexander Sartorius. "Optogenetic fMRI in the mouse hippocampus: hemodynamic response to brief glutamatergic stimuli." *Journal of Cerebral Blood Flow & Metabolism*, p. 0271678X15606455, 2015.

[LLA09]   Martin A Lindquist, Ji Meng Loh, Lauren Y Atlas, and Tor D Wager. "Modeling the hemodynamic response function in fMRI: efficiency, bias and mis-modeling." *Neuroimage*, **45**(1):S187–S198, 2009.

[LLC08]   Louis Lemieux, Helmut Laufs, David Carmichael, Joseph Suresh Paul, Matthew C Walker, and John S Duncan. "Noncanonical spike-related BOLD responses in focal epilepsy." *Human brain mapping*, **29**(3):329–345, 2008.

[LLL10]   Hyun Ju Lee, Jong Kil Lee, Hyun Lee, Ji-woong Shin, Janet E Carter, Toshiro Sakamoto, Hee Kyung Jin, and Jae-sung Bae. "The therapeutic potential of human umbilical cord blood-derived mesenchymal stem cells in Alzheimer's disease." *Neuroscience letters*, **481**(1):30–35, 2010.

[LLW15]   Jia Liu, Hyun Joo Lee, Andrew J Weitz, Zhongnan Fang, Peter Lin, ManKin Choy, Robert Fisher, Vadim Pinskiy, Alexander Tolpygo, Partha Mitra, et al. "Frequency-selective control of cortical and subcortical networks by central thalamus." *eLife*, **4**:e09215, 2015.

[LNS90]   Chia-Sheng Lin, MA Nicolelis, Jay S Schneider, and John K Chapin. "A major direct GABAergic pathway from zona incerta to neocortex." *Science*, **248**(4962):1553–1556, 1990.

[LRC98]   Rodolfo Llinas, Urs Ribary, D Contreras, and Christine Pedroarena. "The neuronal basis for consciousness." *Philosophical Transactions of the Royal Society B: Biological Sciences*, **353**(1377):1841–1849, 1998.

[LS06]   Gilles van Luijtelaar and Evgenia Sitnikova. "Global and focal aspects of absence epilepsy: the contribution of genetic models." *Neuroscience & Biobehavioral Reviews*, **30**(7):983–1003, 2006.

[LUD05]   Philippe Lavallée, Nadia Urbain, Caroline Dufresne, Hajnalka Bokor, László Acsády, and Martin Deschênes. "Feedforward inhibitory control of sensory information in higher-order thalamic nuclei." *The Journal of neuroscience*, **25**(33):7489–7498, 2005.

[LWA15]   Zhifeng Liang, Glenn DR Watson, Kevin D Alloway, Gangchea Lee, Thomas Neuberger, and Nanyin Zhang. "Mapping the functional network of medial prefrontal cortex by combining optogenetics and fMRI in awake rats." *NeuroImage*, **117**:114–123, 2015.

[LWB16]   Hyun Joo Lee, Andrew J Weitz, David Bernal-Casas, Ben A Duffy, ManKin Choy, Alexxai V Kravitz, Anatol C Kreitzer, and Jin Hyung Lee. "Activation of Direct and Indirect Pathway Medium Spiny Neurons Drives Distinct Brain-wide Responses." *Neuron*, **91**(2):412–424, 2016.

[LWP02]   CH Liao, KJ Worsley, J-B Poline, JAD Aston, GH Duncan, and AC Evans. "Estimating the delay of the fMRI response." *NeuroImage*, **16**(3):593–606, 2002.

[LZT14]   Nan Li, Peter van Zijl, Nitish Thakor, and Galit Pelled. "Study of the spatial correlation between neuronal activity and BOLD fMRI responses evoked by sensory and channelrhodopsin-2 stimulation in the rat somatosensory cortex." *Journal of Molecular Neuroscience*, **53**(4):553–561, 2014.

[MBE14]   Joanna Mattis, Julia Brill, Suzanne Evans, Talia N Lerner, Thomas J Davidson, Minsuk Hyun, Charu Ramakrishnan, Karl Deisseroth, and John R Huguenard. "Frequency-dependent, cell type-divergent signaling in the hippocamposeptal projection." *The Journal of Neuroscience*, **34**(35):11769–11780, 2014.

[MBG12]   Bärbel Maus, Gerard JP van Breukelen, Rainer Goebel, and Martijn PF Berger. "Optimal design for nonlinear estimation of the hemodynamic response function." *Human brain mapping*, **33**(6):1253–1267, 2012.

[MBP98]   Robert G Mair, Joshua A Burk, and M Christine Porter. "Lesions of the frontal cortex, hippocampus, and intralaminar thalamic nuclei have distinct effects on remembering in rats." *Behavioral neuroscience*, **112**(4):772, 1998.

[MCD12] Michael Marxen, Ryan J Cassidy, Tara L Dawson, Bernhard Ross, and Simon J Graham. "Transient and sustained components of the sensorimotor BOLD response in fMRI." *Magnetic resonance imaging*, **30**(6):837–847, 2012.

[MD41] RS Morison and EW Dempsey. "A study of thalamo-cortical relations." *American Journal of Physiology–Legacy Content*, **135**(2):281–292, 1941.

[MG02] Cameron C McIntyre and Warren M Grill. "Extracellular stimulation of central neurons: influence of stimulus waveform and frequency on neuronal output." *Journal of Neurophysiology*, **88**(4):1592–1604, 2002.

[MH08] Robert G Mair and Jacqueline R Hembrook. "Memory enhancement with event-related stimulation of the rostral intralaminar thalamic nuclei." *The Journal of Neuroscience*, **28**(52):14293–14300, 2008.

[MHB06] Paul M Matthews, Garry D Honey, and Edward T Bullmore. "Applications of fMRI in translational medicine and clinical practice." *Nature Reviews Neuroscience*, **7**(9):732–744, 2006.

[MIV08] Salima Makni, Jérôme Idier, Thomas Vincent, Bertrand Thirion, Ghislaine Dehaene-Lambertz, and Philippe Ciuciu. "A fully Bayesian approach to the parcel-based detection-estimation of brain activity in fMRI." *Neuroimage*, **41**(3):941–969, 2008.

[MJM98] Martin J McKeown, Tzyy-Ping Jung, Scott Makeig, Greg Brown, Sandra S Kindermann, Te-Won Lee, and Terrence J Sejnowski. "Spatially independent activity patterns in functional MRI data during the Stroop color-naming task." *Proceedings of the National Academy of Sciences*, **95**(3):803–810, 1998.

[MM49] Giuseppe Moruzzi and Horace W Magoun. "Brain stem reticular formation and activation of the EEG." *Electroencephalography and clinical neurophysiology*, **1**(1):455–473, 1949.

[MMB98] Martin J McKeown, Scott Makeig, Greg G Brown, Tzyy-Ping Jung, Sandra S Kindermann, Anthony J Bell, and Terrence J Sejnowski. "Analysis of fMRI data by blind separation into independent spatial components." *Human Brain Mapping*, **6**:160–188, 1998.

[MMS06] William L Maxwell, Mary Anne MacKinnon, Douglas H Smith, Tracy K McIntosh, and David I Graham. "Thalamic nuclei after human blunt head injury." *Journal of Neuropathology & Experimental Neurology*, **65**(5):478–488, 2006.

[MOH11] Robert G Mair, Kristen D Onos, and Jacqueline R Hembrook. "Cognitive activation by central thalamic stimulation: the yerkes-dodson law revisited." *Dose-response*, **9**(3):dose–response, 2011.

[MRM03] Chad H Moritz, Baxter P Rogers, and M Elizabeth Meyerand. "Power spectrum ranked independent component analysis of a periodic fMRI complex motor paradigm." *Human brain mapping*, **18**(2):111–122, 2003.

[MSS14]   Anna S Mitchell, S Murray Sherman, Marc A Sommer, Robert G Mair, Robert P Vertes, and Yogita Chudasama. "Advances in understanding mechanisms of thalamic relays in cognition and behavior." *The Journal of Neuroscience*, **34**(46):15340–15346, 2014.

[MV65]   Allan F Mirsky and JM Van Buren. "On the nature of the "absence" in centrencephalic epilepsy: a study of some behavioral, electroencephalographic and autonomic factors." *Electroencephalography and clinical neurophysiology*, **18**(4):334–348, 1965.

[MWL04]   Anke Meyer-Baese, Axel Wismueller, and Oliver Lange. "Comparison of two exploratory data analysis methods for fMRI: unsupervised clustering versus independent component analysis." *Information Technology in Biomedicine, IEEE Transactions on*, **8**(3):387–398, 2004.

[NB05]   Lori A Newman and Joshua A Burk. "Effects of excitotoxic thalamic intralaminar nuclei lesions on attention and working memory." *Behavioural brain research*, **162**(2):264–271, 2005.

[NBL05]   Georg Nagel, Martin Brauner, Jana F Liewald, Nona Adeishvili, Ernst Bamberg, and Alexander Gottschalk. "Light activation of channelrhodopsin-2 in excitable cells of Caenorhabditis elegans triggers rapid behavioral responses." *Current Biology*, **15**(24):2279–2284, 2005.

[NC03]   Rajesh R Nandy and Dietmar Cordes. "Novel ROC-type method for testing the efficiency of multivariate statistical methods in fMRI." *Magnetic Resonance in Medicine*, **49**(6):1152–1162, 2003.

[NCL92]   Miguel AL Nicolelis, John K Chapin, and Rick CS Lin. "Somatotopic maps within the zona incerta relay parallel GABAergic somatosensory pathways to the neocortex, superior colliculus, and brainstem." *Brain research*, **577**(1):134–141, 1992.

[NCL95]   MAL Nicolelis, JK Chapin, and RCS Lin. "Development of direct GABAergic projections from the zona incerta to the somatosensory cortex of the rat." *Neuroscience*, **65**(2):609–631, 1995.

[NHR04]   Hrachya Nersesyan, Fahmeed Hyder, Douglas L Rothman, and Hal Blumenfeld. "Dynamic fMRI and EEG recordings during spike-wave seizures and generalized tonic-clonic seizures in WAG/Rij rats." *Journal of Cerebral Blood Flow & Metabolism*, **24**(6):589–599, 2004.

[NHT09]   Shing-Chung Ngan, Xiaoping Hu, Li-Hai Tan, and Pek-Lan Khong. "Improvement of spectral density-based activation detection of event-related fMRI data." *Magnetic resonance imaging*, **27**(7):879–894, 2009.

[OLK90]   Seiji Ogawa, Tso-Ming Lee, Alan R Kay, and David W Tank. "Brain magnetic resonance imaging with contrast dependent on blood oxygenation." *Proceedings of the National Academy of Sciences*, **87**(24):9868–9872, 1990.

[PIF07]   Brian N Pasley, Ben A Inglis, and Ralph D Freeman. "Analysis of oxygen metabolism implies a neural origin for the negative BOLD response in human visual cortex." *Neuroimage*, **36**(2):269–276, 2007.

[PJA01]   James T Porter, Cary K Johnson, and Ariel Agmon. "Diverse types of interneurons generate thalamus-evoked feedforward inhibition in the mouse barrel cortex." *The Journal of Neuroscience*, **21**(8):2699–2710, 2001.

[PJS16]   Joana Pinto, João Jorge, Inês Sousa, Pedro Vilela, and Patrícia Figueiredo. "Fourier modeling of the BOLD response to a breath-hold task: Optimization and reproducibility." *NeuroImage*, **135**:223–231, 2016.

[PLO09]   Jesus Pujol, Marina López-Solà, Héctor Ortiz, Joan Carles Vilanova, Ben J Harrison, Murat Yücel, Carles Soriano-Mas, Narcís Cardoner, and Joan Deus. "Mapping brain response to pain in fibromyalgia patients using temporal analysis of FMRI." *PLoS One*, **4**(4):e5224, 2009.

[Plu91]   Fred Plum. "Coma and related global disturbances of the human conscious state." In *Normal and Altered States of Function*, pp. 359–425. Springer, 1991.

[PTJ13]   Vadim Pinskiy, Alexander S Tolpygo, Jamie Jones, Kevin Weber, Neil Franciotti, and Partha P Mitra. "A low-cost technique to cryo-protect and freeze rodent brains, precisely aligned to stereotaxic coordinates for whole-brain cryosectioning." *Journal of neuroscience methods*, **218**(2):206–213, 2013.

[PW06]   G. Paxinos and C. Watson. *The Rat Brain in Stereotaxic Coordinates: Hard Cover Edition*. Elsevier Science, 2006.

[RGM15]   Mark A Rossi, Vinson Go, Tracy Murphy, Quanhai Fu, James Morizio, and Henry H Yin. "A wirelessly controlled implantable LED system for deep brain optogenetic stimulation." *Frontiers in integrative neuroscience*, **9**, 2015.

[RGS05]   Serge ARB Rombouts, Rutger Goekoop, Cornelis J Stam, Frederik Barkhof, and Philip Scheltens. "Delayed rather than decreased BOLD response as a marker for early Alzheimer's disease." *Neuroimage*, **26**(4):1078–1085, 2005.

[RWA06]   Anne C Roc, Jiongjiong Wang, Beau M Ances, David S Liebeskind, Scott E Kasner, and John A Detre. "Altered hemodynamics and regional cerebral blood flow in patients with hemodynamically significant stenoses." *Stroke*, **37**(2):382–387, 2006.

[SAO06]   Amir Shmuel, Mark Augath, Axel Oeltermann, and Nikos K Logothetis. "Negative functional MRI response correlates with decreases in neuronal activity in monkey visual area V1." *Nature neuroscience*, **9**(4):569–577, 2006.

[SBB94]   JJ Sychra, PA Bandettini, N Bhattacharya, and Q Lin. "Synthetic images by subspace transforms I. Principal components images and related filters." *Medical Physics*, **21**(2):193–201, 1994.

[SCG99] Pawel Skudlarski, R Todd Constable, and John C Gore. "ROC analysis of statistical methods used in functional MRI: individual subjects." *Neuroimage*, **9**(3):311–329, 1999.

[Sch78] Gideon Schwarz et al. "Estimating the dimension of a model." *The annals of statistics*, **6**(2):461–464, 1978.

[Sch08] Nicholas D Schiff. "Central thalamic contributions to arousal regulation and neurological disorders of consciousness." *Annals of the New York Academy of Sciences*, **1129**(1):105–118, 2008.

[Sch10] Nicholas D Schiff. "Recovery of consciousness after brain injury: a mesocircuit hypothesis." *Trends in neurosciences*, **33**(1):1–9, 2010.

[Sch12] Nicholas D Schiff. "Moving toward a generalizable application of central thalamic deep brain stimulation for support of forebrain arousal regulation in the severely injured brain." *Annals of the New York Academy of Sciences*, **1265**(1):56–68, 2012.

[SEH02] Erich Seifritz, Fabrizio Esposito, Franciszek Hennel, Henrietta Mustovic, John G Neuhoff, Deniz Bilecen, Gioacchino Tedeschi, Klaus Scheffler, and Francesco Di Salle. "Spatiotemporal pattern of neural processing in the human auditory cortex." *Science*, **297**(5587):1706–1708, 2002.

[SG82] Mircea Steriade and Loyd L Glenn. "Neocortical and caudate projections of intralaminar thalamic neurons and their synaptic excitation from midbrain reticular core." *Journal of Neurophysiology*, **48**:352–371, 1982.

[SG96] S Murray Sherman and RW Guillery. "Functional organization of thalamocortical relays." *Journal of Neurophysiology*, **76**(3):1367–1395, 1996.

[SGK07] Nicholas D Schiff, JT Giacino, K Kalmar, JD Victor, K Baker, M Gerber, B Fritz, B Eisenberg, J O'connor, EJ Kobylarz, et al. "Behavioural improvements with thalamic stimulation after severe traumatic brain injury." *Nature*, **448**(7153):600–603, 2007.

[SJW04] Stephen M Smith, Mark Jenkinson, Mark W Woolrich, Christian F Beckmann, Timothy EJ Behrens, Heidi Johansen-Berg, Peter R Bannister, Marilena De Luca, Ivana Drobnjak, David E Flitney, et al. "Advances in functional and structural MR image analysis and implementation as FSL." *Neuroimage*, **23**:S208–S219, 2004.

[SKM08] Ulrich Schridde, Manjula Khubchandani, Joshua E Motelow, Basavaraju G Sanganahalli, Fahmeed Hyder, and Hal Blumenfeld. "Negative BOLD with large increases in neuronal activity." *Cerebral cortex*, **18**(8):1814–1827, 2008.

[SLC13] Fu-Zen Shaw, Yi-Fang Liao, Ruei-Feng Chen, Yu-Hsing Huang, and Rick CS Lin. "The zona incerta modulates spontaneous spike-wave discharges in the rat." *Journal of neurophysiology*, **109**(10):2505–2516, 2013.

[SM07]   Gilad Silberberg and Henry Markram. "Disynaptic inhibition between neocortical pyramidal cells mediated by Martinotti cells." *Neuron*, **53**(5):735–746, 2007.

[Smi08]   Yoland Smith. "The thalamus." In *Neuroscience in Medicine*, pp. 419–442. Springer, 2008.

[SMS93]   Mircea Steriade, David A McCormick, and Terrence J Sejnowski. "Thalamocortical oscillations in the sleeping and aroused brain." *Science*, **262**(5134):679–685, 1993.

[SNR85]   SJ Shammah-Lagnado, N Negrao, and JA Ricardo. "Afferent connections of the zona incerta: a horseradish peroxidase study in the rat." *Neuroscience*, **15**(1):109–134, 1985.

[SP01]   Thomas Seidenbecher and Hans-Christian Pape. "Contribution of intralaminar thalamic nuclei to spike-and-wave-discharges during spontaneous seizures in a genetic rat model of absence epilepsy." *European Journal of Neuroscience*, **13**(8):1537–1546, 2001.

[SRP04]   Yoland Smith, Dinesh V Raju, Jean-Francois Pare, and Mamadou Sidibe. "The thalamostriatal system: a highly specific network of the basal ganglia circuitry." *Trends in neurosciences*, **27**(9):520–527, 2004.

[SSH09]   Anne C Smith, Sudhin A Shah, Andrew E Hudson, Keith P Purpura, Jonathan D Victor, Emery N Brown, and Nicholas D Schiff. "A Bayesian statistical analysis of behavioral facilitation associated with deep brain stimulation." *Journal of neuroscience methods*, **183**(2):267–276, 2009.

[SSH13]   Nicholas D Schiff, Sudhin A Shah, Andrew E Hudson, Tanya Nauvel, Steven F Kalik, and Keith P Purpura. "Gating of attentional effort through the central thalamus." *Journal of neurophysiology*, **109**(4):1152–1163, 2013.

[SSR15]   Felix Schlegel, Aileen Schroeter, and Markus Rudin. "The hemodynamic response to somatosensory stimulation in mice depends on the anesthetic used: Implications on analysis of mouse fMRI data." *NeuroImage*, **116**:40–49, 2015.

[SSS06]   Prasad Shirvalkar, Malika Seth, Nicholas D Schiff, and Daniel G Herrera. "Cognitive enhancement with central thalamic electrical stimulation." *Proceedings of the National Academy of Sciences*, **103**(45):17007–17012, 2006.

[SSS14]   Aileen Schroeter, Felix Schlegel, Aline Seuwen, Joanes Grandjean, and Markus Rudin. "Specificity of stimulus-evoked fMRI responses in the mouse: the influence of systemic physiological changes associated with innocuous stimulation under four different anesthetics." *Neuroimage*, **94**:372–384, 2014.

[ST07]   Roberto C Sotero and Nelson J Trujillo-Barreto. "Modelling the role of excitatory and inhibitory neuronal activity in the generation of the BOLD signal." *Neuroimage*, **35**(1):149–165, 2007.

[STR10]   Jason Steffener, Matthias Tabert, Aaron Reuben, and Yaakov Stern. "Investigating hemodynamic response variability at the group level using basis functions." *Neuroimage*, **49**(3):2113–2122, 2010.

[SWA16]   Florian Schmid, Lydia Wachsmuth, Franziska Albers, Miriam Schwalm, Albrecht Stroh, and Cornelius Faber. "True and apparent optogenetic BOLD fMRI signals." *Magnetic resonance in medicine*, **In Press**, 2016.

[SWT14]   Zuyao Y Shan, Margaret J Wright, Paul M Thompson, Katie L McMahon, Gabriella GAM Blokland, Greig I de Zubicaray, Nicholas G Martin, Anna AE Vinkhuyzen, and David C Reutens. "Modeling of the hemodynamic responses in block design fMRI studies." *Journal of Cerebral Blood Flow & Metabolism*, **34**(2):316–324, 2014.

[TBM06]   Jason C Trageser, Kathryn A Burke, Radi Masri, Ying Li, Larisa Sellers, and Asaf Keller. "State-dependent gating of sensory inputs by zona incerta." *Journal of neurophysiology*, **96**(3):1456–1463, 2006.

[TK04]   Jason C Trageser and Asaf Keller. "Reducing the uncertainty: gating of peripheral inputs by zona incerta." *The Journal of neuroscience*, **24**(40):8911–8915, 2004.

[TWM82]   Keith R Thulborn, John C Waterton, Paul M Matthews, and George K Radda. "Oxygenation dependence of the transverse relaxation time of water protons in whole blood at high field." *Biochimica et Biophysica Acta (BBA)-General Subjects*, **714**(2):265–270, 1982.

[TYK15]   Norio Takata, Keitaro Yoshida, Yuji Komaki, Ming Xu, Yuki Sakai, Keigo Hikishima, Masaru Mimura, Hideyuki Okano, and Kenji F Tanaka. "Optogenetic Activation of CA1 Pyramidal Neurons at the Dorsal and Ventral Hippocampus Evokes Distinct Brain-Wide Responses Revealed by Mouse fMRI." *PloS one*, **10**(3):e0121417, 2015.

[Ulu08]   Kâmil Uludağ. "Transient and sustained BOLD responses to sustained visual stimulation." *Magnetic resonance imaging*, **26**(7):863–869, 2008.

[UUB15]   Kâmil Uludağ, Kâmil Uğurbil, and Lawrence Berliner. *fMRI: From Nuclear Spins to Brain Functions*, volume 30. Springer, 2015.

[VHF08]   Brent A Vogt, Patrick R Hof, David P Friedman, Robert W Sikes, and Leslie J Vogt. "Norepinephrinergic afferents and cytology of the macaque monkey midline, mediodorsal, and intralaminar thalamic nuclei." *Brain Structure and Function*, **212**(6):465–479, 2008.

[VVV97]   Marcos Velasco, Francisco Velasco, Ana Luisa Velasco, Francisco Brito, Friacro Jiménez, Irma Marquez, and Beatriz Rojas. "Electrocortical and behavioral responses produced by acute electrical stimulation of the human centromedian thalamic nucleus." *Electroencephalography and clinical neurophysiology*, **102**(6):461–471, 1997.

[VWJ99]   YD Van Der Werf, JGE Weerts, J Jolles, MP Witter, J Lindeboom, and Ph Schel-
           tens. "Neuropsychological correlates of a right unilateral lacunar thalamic infarc-
           tion." *Journal of Neurology, Neurosurgery & Psychiatry*, **66**(1):36–42, 1999.

[War02]   B Douglas Ward. "Deconvolution analysis of fMRI time series data." *Milwaukee,
           WI: Biophysics Research Institute, Medical College of Wisconsin*, pp. 25–26, 2002.

[Was00]   Larry Wasserman. "Bayesian model selection and model averaging." *Journal of
           mathematical psychology*, **44**(1):92–107, 2000.

[WBS04]   Mark W Woolrich, Timothy EJ Behrens, and Stephen M Smith. "Constrained linear
           basis sets for HRF modelling using Variational Bayes." *NeuroImage*, **21**(4):1748–
           1761, 2004.

[WEM92]   Keith J Worsley, Alan C Evans, S Marrett, P Neelin, et al. "A three-dimensional
           statistical analysis for CBF activation studies in human brain." *Journal of Cerebral
           Blood Flow and Metabolism*, **12**:900–900, 1992.

[WF95]   Keith J Worsley and Karl J Friston. "Analysis of fMRI time-series revisited – again."
           Neuroimage, **2**(3):173–181, 1995.

[WFL15]   Andrew J Weitz, Zhongnan Fang, Hyun Joo Lee, Robert S Fisher, Wesley C Smith,
           ManKin Choy, Jia Liu, Peter Lin, Matthew Rosenberg, and Jin Hyung Lee. "Opto-
           genetic fMRI reveals distinct, frequency-dependent networks recruited by dorsal and
           intermediate hippocampus stimulations." *NeuroImage*, **107**:229–241, 2015.

[WLD02]   Axel Wismüller, Oliver Lange, Dominik R Dersch, Gerda L Leinsinger, Klaus Hahn,
           Benno Pütz, and Dorothee Auer. "Cluster analysis of biomedical image time-series."
           International Journal of Computer Vision, **46**(2):103–128, 2002.

[WMM10]   Kathleen A Williams, Matthew Magnuson, Waqas Majeed, Stephen M LaConte,
           Scott J Peltier, Xiaoping Hu, and Shella D Keilholz. "Comparison of α-chloralose,
           medetomidine and isoflurane anesthesia for functional connectivity mapping in the
           rat." *Magnetic resonance imaging*, **28**(7):995–1003, 2010.

[WR12]   Marijke Welvaert and Yves Rosseel. "How ignoring physiological noise can bias
           the conclusions from fMRI simulation results." *Journal of neuroscience methods*,
           211(1):125–132, 2012.

[WRJ08]   Ralph Weber, Pedro Ramos-Cabrer, Carlos Justicia, Dirk Wiedermann, Cordula
           Strecker, Christiane Sprenger, and Mathias Hoehn. "Early prediction of func-
           tional recovery after experimental stroke: functional magnetic resonance imaging,
           electrophysiology, and behavioral testing in rats." *The Journal of Neuroscience*,
           28(5):1022–1029, 2008.

[WSB01]   Florian Weilke, Sabine Spiegel, Henning Boecker, Helga Gräfin von Einsiedel, Bas-
           tian Conrad, Markus Schwaiger, and Peter Erhard. "Time-resolved fMRI of acti-
           vation patterns in M1 and SMA during complex voluntary movement." *Journal of
           neurophysiology*, **85**(5):1858–1863, 2001.

[WSG11]   W Weber-Fahr, A Sartorius, N Gass, Z Li, and W Kelsch. "Optogenetically induced BOLD of excitatory neurons in the mouse hippocampus at 9.4 T: identification of a hippocampal network." In *Proc. Intl. Soc. Magn. Reson. Med*, volume 19, 2011.

[WWG02]   Ysbrand D Van der Werf, Menno P Witter, and Henk J Groenewegen. "The intralaminar and midline nuclei of the thalamus. Anatomical and functional evidence for participation in processes of arousal and awareness." *Brain Research Reviews*, **39**(2):107–140, 2002.

[YFD11]   Ofer Yizhar, Lief E Fenno, Thomas J Davidson, Murtaza Mogri, and Karl Deisseroth. "Optogenetics in neural systems." *Neuron*, **71**(1):9–34, 2011.

[YFP11]   Ofer Yizhar, Lief E Fenno, Matthias Prigge, Franziska Schneider, Thomas J Davidson, Daniel J O'Shea, Vikaas S Sohal, Inbal Goshen, Joel Finkelstein, Jeanne T Paz, et al. "Neocortical excitation/inhibition balance in information processing and social dysfunction." *Nature*, **477**(7363):171–178, 2011.

[YHW16]   Xin Yu, Yi He, Maosen Wang, Hellmut Merkle, Stephen J Dodd, Afonso C Silva, and Alan P Koretsky. "Sensory and optogenetically driven single-vessel fMRI." *Nature methods*, **13**(4):337–340, 2016.